SEMICONDUCTOR PHOTODETECTORS FOR PHOTON-STARVED APPLICATIONS IN THE SHORT-WAVELENGTH INFRARED SPECTRAL REGION

by

Kateryna Kuzmenko

Submitted for the degree of Doctor of Philosophy

Institute of Photonics and Quantum Sciences

School of Engineering and Physical Sciences

Heriot-Watt University

May 2019

Abstract

The design, fabrication and characterisation of planar geometry Ge-on-Si single-photon avalanche diode (SPAD) detectors is described in this Thesis. These devices utilise a Si avalanche multiplication layer, and an adjacent Ge layer to absorb short-wave infrared incident photons. The innovative planar geometry design ensures the confinement of the high electric field to the centre of the detector away from the exposed sidewalls resulting in significantly reduced dark count rate (DCR).

Planar Ge-on-Si SPADs were fabricated and characterised in terms of single-photon detection efficiency (SPDE), DCR, and timing jitter. These devices exhibited SPDE of almost one order of magnitude greater than previously reported, with the highest SPDE measured being 38%. The dark count rates per unit area were approximately 4 orders of magnitude less than equivalent mesa devices. A record-low noise equivalent power of 4×10^{-17} $WHz^{-1/2}$ was obtained, more than two orders of magnitude lower than the previous best reported value. The lowest timing jitter of 26 μm diameter devices was 150 ps. These devices exhibited lower afterpulsing when compared to a commercial InGaAs/InP SPAD detector, illustrating the potential for high count rate operation. An investigation of an SPDE spectral dependence at different operating temperatures revealed that efficient single-photon detection of 1550 nm wavelength light will require an operating temperature of 245 K.

Laboratory-based light detection and ranging (LIDAR) experiments using the time-of-flight approach were performed using an individual Ge-on-Si SPAD detector. This approach allowed depth and intensity profiles of scanned targets to be reconstructed. Based on these results, a parametric LIDAR model was used to estimate LIDAR performance at long distances. For example, eye-safe sub-mW average laser power levels would be sufficient for imaging at kilometre distances. It was demonstrated that by employing appropriate image processing algorithms the total acquisition time can be reduced down to a few seconds for a 10000 pixels image at kilometre range, illustrating the potential for rapid three-dimensional imaging for automotive applications.

Acknowledgements

I would like to thank everyone who has contributed one way or another towards this achievement. Without the help, support and belief of the people in my life, I would not have been able to complete the work presented here. Working towards this Thesis has truly been a remarkable experience.

My foremost thanks go to Prof. Gerald S. Buller for his guidance, support, patience, ideas, and motivation, which powered and inspired me throughout the years of my PhD. Most of all I am grateful that he offered me the opportunity, which has led to a whole new world of knowledge, experience and wonderful professional people, all of whom I am honoured to call my colleagues and friends.

It is hard to express in words my gratitude for Dr. Peter Vines. It has been my honour and pleasure to work alongside with him. I am forever grateful for his invaluable input to my work through his inspirational ideas, his willingness to receive and answer questions, his patience and endless support, for all the kind words of encouragement and for all the skills that I have learned from him. He has set the professional standard that I hope to reach one day.

I would also like to thank all the former and current members of the Single-Photon Group here at Heriot-Watt University. Especially, I would like to thank Dr. Aongus McCarthy for his invaluable input, for all the help with the optics in the lab and all the ideas and discussions we have had over the years. In addition, I would like to thank Dr. Robert J. Collins, Dr. Abderrahim Halimi and Dr. Aurora Maccarone for their help and input towards the imaging experiment presented here. I would like to thank Dr. Ross J. Donaldson, Dr. Ximing Ren, Dr. Agata Pawlikowska, Dr. Giuseppe Intermite, Pete Connolly, Ugo Zanforlin, Zoë Greener, David W. Canning, Parthena Mavridou and, most of all, Rachael Tobin for their help and support, useful discussions, and much-needed laughs in the difficult moments.

I would like to express my gratitude to School of Engineering and Physical Sciences at Heriot-Watt University for funding my work. Thanks to all of the staff of the University that I had the pleasure to work with, and especially to Neil Ross for his help in the clean room.

Our collaboration with the group of Prof. Douglas Paul from University of Glasgow has been vital for this project. I would like to thank all the people that have been involved in the fabrication of the samples described in this Thesis, namely: Dr. Derek C.S. Dumas, Dr. Jaroslaw Kirdoda, Dr. Muhammad Mirza, Dr. Ross W. Millar and Dr. Lourdes Ferre Llin. Of course, special thanks go to Prof. Douglas Paul for his guidance and input towards the development of the fabrication processes.

I would like to thank all my friends for their love and support along this challenging but wonderful journey. I am fortunate enough that the list of people that have been there for me is too long to mention all the names.

My biggest thanks go to my family. Although I have seen my family in Ukraine very few times during my PhD, I could always feel their love, support and encouragement despite the distance. I am forever grateful to my partner and my friend Dr. Jack Wildman and his family. All the patience, support and love of all the wonderful people in my life has helped me reach my goals and inspires me towards those for the future.

Contents

List of Tables

List of Figures

Acronyms and Abbreviations

2D – Two-Dimensional

3D – Three-Dimensional

AC – Alternating Current

ADMM – Alternating Direction Method of Multipliers

ALD – Atomic Layer Deposition

APD – Avalanche Photodiode

As - Arsenic

ARC – Anti-Reflective Coating

B - Boron

BF_2 – Boron Difluoride

BS – Beam Splitter

CFD – Constant Fraction Discriminator

CH_4 –Methane

CMOS – Complimentary Metal-Oxide-Semiconductor

CO_2 – Carbon Dioxide

CVD – Chemical Vapour Deposition

DC – Direct Current

DCD – Dark Current Density

DCR – Dark Count Rate

EHP – Electron-Hole Pair

FGR – Floating Guard Ring

FWHM – Full Width at Half Maximum

GaAs – Gallium Arsenide

Ge – Germanium

GeO_2 – Germanium dioxide

Ge-on-Si – Germanium on Silicon

GR – Guard Ring

GRC – Generation-Recombination Centre

HCl – Hydrochloric acid

HF – Hydrofluoric acid

H_2O – Dihydrogen monoxide

H_2O_2 – Hydrogen peroxide

H_2SO_4 – Sulfuric acid

HSQ – Hydrogen silsesquioxane

InGaAs – Indium Gallium Arsenide

InP – Indium Phosphide

InGaAs/InP – Indium Gallium Arsenide/ Indium Phosphide

InGaAs/InP-on-Si – Indium Gallium Arsenide/Indium Phosphide on Silicon

LIDAR – Light Detection and Ranging

LP-CVD – Low Pressure - Chemical Vapour Deposition

MBE – Molecular Beam Epitaxy

MD – Misfit Dislocation

MoSi - Molybdenum Silicide

MR – Multiplication Region

NbN – Niobium Nitride

NbTiN – Niobium Titanium Nitride

NEP – Noise Equivalent Power

NIR – Near Infrared

SACM – Separate Absorption Charge Multiplication

SAGCM – Separate Absorption Grading Charge Multiplication

SBR – Signal-to-Background Ratio

SEG – Selective Epitaxial Growth

SEM – Scanning Electron Microscopy

SF_6/C_4F_8 – Sulfur Hexafluoride / Octafluorocyclobutane

SNSPD – Superconducting Nanowire Single-Photon Detector

SNR – Signal-to-Noise Ratio

SOI – Silicon on Insulator

SPAD – Single-Photon Avalanche Diode

SPDE – Single-Photon Detection Efficiency

Si - Silicon

SiGe – Silicon-Germanium

Si_3N_4 – Silicon Nitride

SiO_2 – Silicon Dioxide

Si/SiGe – Silicon/Silicon-Germanium

SWIR – Short-Wavelength Infrared

TAC – Time-to-Amplitude Converter

TCSPC – Time-Correlated Single-Photon Counting

TD – Threading Dislocation

TDD – Threading Dislocation Density

TEM – Transmission Electron Microscopy

Ti/TiN – Titanium/Titanium Nitride

ToF – Time of Flight

USB – Universal Serial Bus

RC – Reflective Collimator

RCA – Radio Corporation of America

RDI-TV – Restoration Depth and Intensity using Total Variation

RHEED – Reflection High-Energy Electron Diffraction

RP-CVD – Reduced Pressure – Chemical Vapour Deposition

RTA – Rapid Thermal Annealing

UHV-CVD – Ultra-High Vacuum – Chemical Vapour Deposition

WSi - Tungsten silicide

Zn – Zinc

List of Publications

Peer Reviewed Journals, Conferences and a Patent

D.J. Paul, D. Dumas, J. Kirdoda, R.W. Millar, M.M. Mirza, G.S. Buller, P. Vines and K. Kuzmenko "Single photon avalanche detector, method of use therefore and method for its manufacture" GB Patent application no. 1814688.6 (10th September 2018)

J. Kirdoda, D.C. Dumas, P. Vines, K. Kuzmenko, R.W. Millar, G.S. Buller, D.J. Paul, "Ge-on-Si single-photon avalanche detectors for lidar applications" SPIE Security and Defence, September 2018

D.C. Dumas, J. Kirdoda, R.W. Millar, P. Vines, K. Kuzmenko, G.S. Buller, and D.J. Paul, "High-Efficiency Ge-on-Si SPADs for Short-Wave Infrared". SPIE Photonics West, San Francisco, CA, USA, Feb 2019, p. 1091424.

P. Vines, K. Kuzmenko, J. Kirdoda, D.C. Dumas, M.M. Mirza, R.W. Millar, D.J. Paul, and G.S. Buller "High performance planar germanium-on-silicon single-photon avalanche diode detectors". Nature Communications. 2019 Mar 6;10(1):1086.

K. Kuzmenko, P. Vines, Z. Greener, J. Kirdoda, D.C. Dumas, M.M. Mirza, R.W. Millar, D.J. Paul, and G.S. Buller, "Planar geometry Ge-on-Si SPAD detectors for the short-wave infrared", SPIE Defence and Commercial Sensing Conference, April 2019

J. Kirdoda, L. Ferre Llin, K. Kuzmenko, P. Vines, Z. Greener, D.C. Dumas, R.W. Millar, M.M. Mirza, G.S. Buller, and D.J. Paul, "High Efficiency Planar Ge-on-Si Single-Photon Avalanche Diode Detectors". CLEO: QELS_Fundamental Science, May 2019. ISBN 9781943580576

K. Kuzmenko, P. Vines, A. Halimi, J. Kirdoda, D.C. Dumas, M.M. Mirza, R.W. Millar, D.J. Paul, and G.S. Buller, "Three-dimensional imaging using a planar Ge-on-Si SPAD detector", Optics Express (in preparation)

Chapter 1. Introduction

A range of photon counting applications require single-photon detection in the short-wavelength infrared (SWIR) spectral region. There are several advantages in operating in the SWIR region when compared to the visible or near infrared (NIR) wavelength regions. For example, in light detection and ranging (LIDAR) imaging applications, wavelengths above 1400 nm display better atmospheric transmission due to reduced attenuation caused by water vapour, CO_2, CH_4 and other gases, when compared to the NIR and visible spectral regions [1, 2]. In imaging through atmospheric obscurants, 1550 nm wavelength radiation has demonstrated significantly better performance compared to the visible and NIR regions [3, 4]. In addition, the contribution to background from solar radiation is much greater in the visible and NIR wavelength regions compared to the SWIR [5, 6]. Furthermore, the laser eye-safety threshold is significantly increased when operated in the SWIR spectral region [7], allowing safe use of LIDAR at much higher laser power levels. At wavelengths of 1400 nm to 1700 nm, the average laser power considered to be eye-safe is at least 20 times greater than at wavelengths around 850 nm.

In quantum computing and quantum communications applications, operating at 1310 nm or 1550 nm wavelengths allows for the exploitation of the low-loss optical fibre windows [8]. Another important aspect in linear optical quantum computing is integration of all the optical components on the same chip, avoiding the key issue of insertion losses, and minimising the overall footprint and cost. Since many implementations of linear optical quantum computing components are made on Si-based planar lightwave technology [9, 10], the development of high-efficiency SWIR single-photon detectors that are fully integrated on Si photonics platform is a key future consideration. The aim of this Thesis is to design, fabricate and characterise single-photon detectors for operation in the SWIR spectral region, which can be integrated onto Si and potentially fabricated using complementary metal-oxide-semiconductor (CMOS) compatible processes widely used in the microelectronics industry.

In the following Chapter 2, a detailed discussion of single-photon detection in the SWIR spectral region is presented. First, a brief introduction to the physics and working principles of photodiodes is given, with the main focus being on avalanche photodiodes (APDs) and single-photon avalanche diode (SPAD) detectors. Following this, a detailed

explanation of the time-correlated single-photon counting (TCSPC) technique is presented. This technique is increasingly used in various applications such as three-dimensional depth imaging [11, 12] including long range [13-15] and underwater imaging [16, 17], quantum communications [18-21], and in the characterisation of single-photon detectors [22-25]. A short discussion of the resolution and possible background noise sources of this technique is presented. An overview of existing single-photon detectors that operate in the SWIR region is also presented. For example, InGaAs/InP SPAD detectors are semiconductor-based single-photon detectors that have demonstrated single-photon detection efficiencies (SPDEs) of up to 45% at a detection wavelength of 1550 nm [26], dark count rates (DCRs) that can be as low as 1 count per second [27], and can demonstrate timing jitters as low as 30 ps [26]. Typically, InGaAs/InP SPAD detectors are operated at temperatures in the region of 200 K to 240 K. These detectors are commonly used in LIDAR imaging applications where compact and mobile detectors are required. However, these detectors suffer from the effects of afterpulsing, which limits the maximum count rate possible for these detectors. Another commonly used example is superconducting nanowire single-photon detectors (SNSPDs). These detectors demonstrate high SPDEs of 90% at a detection wavelength of 1550 nm [28-30], DCRs that can be as low as 10 counts per second [28] and timing jitters that can be as low as 18 ps [31]. Although SNSPDs demonstrate excellent performance, these detectors require cryogenic temperatures of below 3 K for operation, which limits their range of applicability. Therefore, an alternative single-photon detection technology that would provide high count rates while remaining compact, preferably operated at temperature compatible with thermoelectric Peltier cooling systems [32, 33] is of high demand.

Chapter 3 discusses the potential of Ge as a candidate material for single-photon detection at wavelengths up to 1.6 μm in the SWIR spectral region. Throughout, the importance of detector integration onto the Si photonics platform along with the other planar lightwave circuitry components have been discussed. One of the advantages of Ge is that it can be grown on Si substrates, which shows the potential for the development of single-photon detectors that are compatible with the CMOS fabrication processes typically used in the microelectronics industry. As will be discussed, it is very challenging to integrate InGaAs/InP detectors onto Si platforms due to the large 8% lattice mismatch between the materials. The lattice mismatch between Ge and Si is 4.2%, which although lower than the value for InGaAs/InP-on-Si, it still introduces a number of challenges in the growth process. A brief overview of growth techniques in terms of their advantages and

limitations is presented along with a short review of InGaAs/InP-on-Si photodetectors reported in the literature. To conclude this discussion, a detailed review of the research and development of Ge-on-Si photodetectors is given. Different design structures, such as separate absorption charge multiplication (SACM) and waveguide integrated structures, are discussed and the successes and challenges of fabricating Ge-on-Si SPAD detectors are described. In addition, the single-photon detection performance of Ge-on-Si SPAD detectors previously reported in the scientific literature is discussed and defines the benchmark for the results presented in this Thesis.

In Chapter 4, new proposed designs for Ge-on-Si SPAD detectors are described. The results of finite-element analysis of the proposed structures using Silvaco Atlas will be presented. This software allowed for the simulation of the electric field profile across the proposed structures under different reverse bias conditions. The results of this analysis were instrumental in the development of a planar geometry design that ensures that a high electric field, which is crucial for the self-sustaining avalanche necessary for Geiger mode operation, is confined along the centre of the device away from the exposed Ge sidewalls. This design served as a basis for all the fabrication generations analysed and described in this Thesis. This is then followed by a discussion of the preliminary results of the optical characterisation of these detectors. These results confirmed that this planar design largely eliminates the contribution of carriers generated along the sidewalls to the overall dark current and, thus, demonstrating the potential for a significant reduction in DCR.

In Chapter 5, the results of single-photon characterisation of the planar Ge-on-Si SPAD detectors is presented. These detectors have been characterised at temperatures between 78 K and 175 K. The SPDEs and DCRs at a range of excess biases up to 7.5% at operating temperatures between 78 K and 125 K measured using 100 µm and 26 µm diameter detectors are presented. In addition, the spectral dependence of SPDE with varying operating temperatures of up to 175 K is presented. From this dependence, an estimation of the required operating temperatures sufficient for successful detection at 1550 nm wavelength is derived. This is followed by a study of afterpulsing in Ge-on-Si SPAD detectors at temperatures of up to 175 K. A comparison of afterpulsing in a commercial InGaAs/InP SPAD detector and a planar Ge-on-Si SPAD detector at identical operating conditions will be provided. In addition, some of the key results of this Thesis, a record low timing jitter and noise equivalent power (NEP) measured using these planar Ge-on-Si SPAD detectors will be presented.

In Chapter 6, a laboratory-based LIDAR three-dimensional imaging experiment is presented. A LIDAR system based on an individual Ge-on-Si SPAD detector is described. Selected targets were illuminated with 1450 nm wavelength, a wavelength selected due to its relatively high laser eye-safety threshold. The time of the flight (ToF) information of back-scattered photons was recorded by a photon counting module. This information was then used for the reconstruction of the depth and intensity profiles of the targets. Both the pixel-wise cross-correlation technique and the Restoration of Depth and Intensity using Total Variation (RDI-TV) [34] algorithms for image reconstruction will be discussed. Three-dimensional images reconstructed using both techniques will be presented, with data acquired with different acquisition times. RDI-TV allows for excellent image reconstruction from partially corrupt data or in a scenario where only partial information of the target is acquired. For example, the results of image reconstruction using RDI-TV are presented for scenarios where only 25% of the target was randomly scanned. Such algorithms allow for the reduction of the total acquisition times required for successful imaging and therefore show the potential for rapid imaging in automotive LIDAR applications. Based on the experimental results described in Chapters 5 and 6 a LIDAR model has been developed to estimate the average laser powers required for imaging at longer distance ranges. From this estimation, it is predicted that eye-safe laser power levels are sufficient for imaging at 1 km ranges for per pixel acquisition times as low as 1 ms. Additionally, an estimation of the average laser powers required for imaging at a distance of 300 metres in various attenuating media is given.

In Chapter 7, a summary of the conclusions drawn throughout the thesis is given along with an overview of potential avenues for future work.

1.1 References:

1. L.S. Rothman, D. Jacquemart, A. Barbe, D.C. Benner, M. Birk, L. Brown, M. Carleer, C. Chackerian Jr, K. Chance, L. Coudert, V. Danai, V.M. Devic, J.M. Flaudh, R.R. Gamachej, A. Goldmank, J.M. Hartmannh, K.W. Jucksl, A.G. Makim, J.Y. Mandini, S.T. Massien, J. Orphalh, A. Perrinh, C.P. Rinslando, M.A.H. Smitho, J. Tennysonp, R.N. Tolchenovp, R.A. Tothe, J. Vander Auweraf, P. Varanasiq, G. Wagner, *The HITRAN 2004 molecular spectroscopic database.* Journal of Quantitative Spectroscopy and Radiative Transfer, 2005. **96**(2): p. 139-204.

2. D. Killinger, *Free space optics for laser communication through the air*. Optics and Photonics News, 2002. **13**(10): p. 36-42.

3. R. Tobin, A. Halimi, A. McCarthy, M. Laurenzis, F. Christnacher, and G.S. Buller, *Three-dimensional single-photon imaging through obscurants.* Optics Express, 2019. **27**(4): p. 4590-4611.

4. F. Nadeem, T. Javornik, E. Leitgeb, V. Kvicera and G. Kandus, *Continental fog attenuation empirical relationship from measured visibility data.* Radioengineering, 2010. **19**(4): p. 596-600.

5. H. Willebrand and B.S. Ghuman, *Free space optics: enabling optical connectivity in today's networks*. 2002: SAMS publishing.

6. R.E. Bird, R.L. Hulstrom and L. Lewis, *Terrestrial solar spectral data sets.* Solar Energy, 1983. **30**(6): p. 563-573.

7. International Electrotechnical Commission, *Safety of laser products-Part 1: Equipment classification and requirements.* IEC 60825-1, 2007.

8. G.S. Buller and R.J. Collins, *Single-photon detectors for infrared wavelengths in the range 1–1.7 μm*, in *Advanced Photon Counting*. 2014, Springer. p. 43-69.

9. J.L. O'brien, *Optical quantum computing.* Science, 2007. **318**(5856): p. 1567-1570.

10. M.G. Thompson, A. Politi, J.C. Matthews and J.L. O'Brien, *Integrated waveguide circuits for optical quantum computing.* IET Circuits, Devices & Systems, 2011. **5**(2): p. 94-102.

11. B. Schwarz, *LIDAR: Mapping the world in 3D.* Nature Photonics, 2010. **4**(7): p. 429.

12. A.M. Wallace, A. McCarthy, C.J. Nichol, X. Ren, S. Morak, D. Martinez-Ramirez, I.H. Woodhouse, and G.S. Buller, *Design and evaluation of multispectral lidar for the recovery of arboreal parameters.* IEEE Transactions on Geoscience and Remote Sensing, 2014. **52**(8): p. 4942-4954.

13. A. McCarthy, X. Ren, A. Della Frera, N.R. Gemmell, N.J. Krichel, C. Scarcella, A. Ruggeri, A. Tosi, and G.S. Buller, *Kilometer-range depth imaging at 1550 nm wavelength using an InGaAs/InP single-photon avalanche diode detector.* Optics Express, 2013. **21**(19): p. 22098-22113.

14. A.M. Pawlikowska, A. Halimi, R.A. Lamb and G.S. Buller, *Single-photon three-dimensional imaging at up to 10 kilometers range.* Optics Express, 2017. **25**(10): p. 11919-11931.

15. Z. Li, E. Wu, C. Pang, B. Du, Y. Tao, H. Peng, H. Zeng, and G. Wu, *Multi-beam single-photon-counting three-dimensional imaging lidar.* Optics Express, 2017. **25**(9): p. 10189-10195.

16. A. Maccarone, A. McCarthy, X. Ren, R.E. Warburton, A.M. Wallace, J. Moffat, Y. Petillot, and G.S. Buller, *Underwater depth imaging using time-correlated single-photon counting.* Optics Express, 2015. **23**(26): p. 33911-33926.

17. A. Halimi, A. Maccarone, A. McCarthy, S. McLaughlin and G.S. Buller, *Object depth profile and reflectivity restoration from sparse single-photon data acquired in underwater environments.* IEEE Transactions on Computational Imaging, 2017. **3**(3): p. 472-484.

18. R.H. Hadfield, *Single-photon detectors for optical quantum information applications.* Nature Photonics, 2009. **3**(12): p. 696.

19. A. Boaron, B. Korzh, R. Houlmann, G. Boso, D. Rusca, S. Gray, M.-J. Li, D. Nolan, A. Martin, and H. Zbinden, *Simple 2.5 GHz time-bin quantum key distribution.* Applied Physics Letters, 2018. **112**(17): p. 171108.

20. P.J. Clarke, R.J. Collins, P.A. Hiskett, M.-J. García-Martínez, N.J. Krichel, A. McCarthy, M.G. Tanner, J.A. O'Connor, C.M. Natarajan, and S. Miki, *Analysis of detector performance in a gigahertz clock rate quantum key distribution system.* New Journal of Physics, 2011. **13**(7): p. 075008.

21. R.J. Collins, R. Amiri, M. Fujiwara, T. Honjo, K. Shimizu, K. Tamaki, M. Takeoka, M. Sasaki, E. Andersson, and G.S. Buller, *Experimental demonstration of quantum digital signatures over 43 dB channel loss using differential phase shift quantum key distribution.* Scientific Reports, 2017. **7**(1): p. 3235.

22. R.E. Warburton, G. Intermite, M. Myronov, P. Allred, D.R. Leadley, K. Gallacher, D.J. Paul, N.J. Pilgrim, L.J.M. Lever, Z. Ikonic, R.W. Kelsall, E. Huante-Ceron, A.P. Knights, and G.S. Buller, *Ge-on-Si Single-Photon Avalanche Diode Detectors: Design, Modeling, Fabrication, and Characterization at Wavelengths 1310 and 1550 nm.* IEEE Transactions on Electron Devices, 2013. **60**(11): p. 3807-3813.

23. S. Pellegrini, R.E. Warburton, L.J. Tan, J.S. Ng, A.B. Krysa, K. Groom, J.P. David, S. Cova, M.J. Robertson, and G.S. Buller, *Design and performance of an InGaAs-InP single-photon avalanche diode detector.* IEEE Journal of Quantum Electronics, 2006. **42**(4): p. 397-403.

24. B. Korzh, T. Lunghi, K. Kuzmenko, G. Boso and H. Zbinden, *Afterpulsing studies of low-noise InGaAs/InP single-photon negative-feedback avalanche diodes.* Journal of Modern Optics, 2015. **62**(14): p. 1151-1157.

25. P. Vines, K. Kuzmenko, J. Kirdoda, D.C. Dumas, M.M. Mirza, R.W. Millar, D.J. Paul, and G.S. Buller, *High performance planar germanium-on-silicon single-photon avalanche diode detectors.* Nature Communications, 2019. **10**(1): p. 1086.

26. M.A. Itzler, R. Ben-Michael, C.-F. Hsu, K. Slomkowski, A. Tosi, S. Cova, F. Zappa, and R. Ispasoiu, *Single photon avalanche diodes (SPADs) for 1.5 μ m photon counting applications.* Journal of Modern Optics, 2007. **54**(2-3): p. 283-304.

27. B. Korzh, N. Walenta, T. Lunghi, N. Gisin and H. Zbinden, *Free-running InGaAs single photon detector with 1 dark count per second at 10% efficiency.* Applied Physics Letters, 2014. **104**(8): p. 081108.

28. W. Zhang, L. You, H. Li, J. Huang, C. Lv, L. Zhang, X. Liu, J. Wu, Z. Wang, and X. Xie, *NbN superconducting nanowire single photon detector with efficiency over 90% at 1550 nm wavelength operational at compact cryocooler temperature.* Science China Physics, Mechanics & Astronomy, 2017. **60**(12): p. 120314.

29. F. Marsili, V.B. Verma, J.A. Stern, S. Harrington, A.E. Lita, T. Gerrits, I. Vayshenker, B. Baek, M.D. Shaw, R.P. Mirin, and S. Nam, *Detecting single infrared photons with 93% system efficiency.* Nature Photonics, 2013. **7**(3): p. 210.

30. I. Esmaeil Zadeh, J.W. Los, R.B. Gourgues, V. Steinmetz, G. Bulgarini, S.M. Dobrovolskiy, V. Zwiller, and S.N. Dorenbos, *Single-photon detectors combining high efficiency, high detection rates, and ultra-high timing resolution.* Apl Photonics, 2017. **2**(11): p. 111301.

31. A. Pearlman, A. Cross, W. Slysz, J. Zhang, A. Verevkin, M. Currie, A. Korneev, P. Kouminov, K. Smirnov, and B. Voronov, *Gigahertz counting rates of NbN single-photon detectors for quantum communications.* IEEE Transactions on Applied Superconductivity, 2005. **15**(2): p. 579-582.

32. H. Goldsmid, *Principles of thermoelectric devices.* British Journal of Applied Physics, 1960. **11**(6): p. 209.

33. B. Wolfram, *Peltier cooling apparatus*. 1963, Google Patents.

34. A. Halimi, Y. Altmann, A. McCarthy, X. Ren, R. Tobin, G.S. Buller, and S. McLaughlin. *Restoration of intensity and depth images constructed using sparse single-photon data*. in *Signal Processing Conference (EUSIPCO), 2016 24th European*. 2016. IEEE.

Chapter 2. Single-photon detection in the short-wavelength infrared region

2.1 Introduction

Many different applications such as fibre-optic communications systems and applications in medicine, astronomy, and industry use photodiodes to convert an optical signal into an electrical one. These applications have unique requirements and limitations. Therefore, a wide variety of different materials and designs have been demonstrated during the past several decades. In this Chapter, a short introduction to the physics of semiconductor photodiodes will be given along with a description of the p-n junction and several photodiode structures, starting with basic reverse biased p-n and p-i-n photodiodes, followed by avalanche photodiodes (APD) and single-photon avalanche diode (SPAD) detectors. In addition, a summary of the main performance characteristics of photodetectors such as responsivity, dark current, and signal-to-noise ratio is given followed by a brief analysis of the advantages and constraints of the photodiodes. A description of the time-correlated single-photon counting (TCSPC) technique is then given along with a detailed description of the important characteristics of a SPAD such as single-photon detection efficiency (SPDE), dark current rate (DCR), timing jitter, noise equivalent power (NEP) and the afterpulsing phenomenon. The Chapter concludes with an overview of the reported single-photon detectors in short-wavelength infrared (SWIR) region such as InGaAs/InP SPAD detectors and superconducting nanowire single-photon detectors (SNSPDs).

2.2 p-n and p-i-n photodiodes

An intrinsic semiconductor material becomes n-type or p-type semiconductor when doped with donor or acceptor impurities respectively [1]. The names ‘n-type’ and ‘p-type’ refer to the charges of the dominating charge carriers: n-type semiconductors have greater electron concentration, while p-type semiconductors are hole dominated. The type and the concentration of the carriers defines the position of the Fermi level. It lies closer to the conduction band than the valence band in the n-type semiconductor compared to the Fermi level of the intrinsic material, and closer to the valence band for the p-type material. When an n-type semiconductor material with a donor concentration, N_d, is brought into contact with a p-type semiconductor with an acceptor concentration,

N_a, a p-n junction is formed. Due to the difference in the concentration of charge carriers between each material of the junction, free charge carriers from each side will diffuse to the opposite side of the junction. As a result, positive carriers leave negative ion acceptors with concentration N_{a-} and positive ion donors with concentration N_{d+} behind in the p-type and n-type regions, respectively. Those negative and positive ions generate an electric field, as shown on Figure 2.1. At equilibrium, this region of diffused charges expands into both regions of the p-n junction and is known as the depletion region.

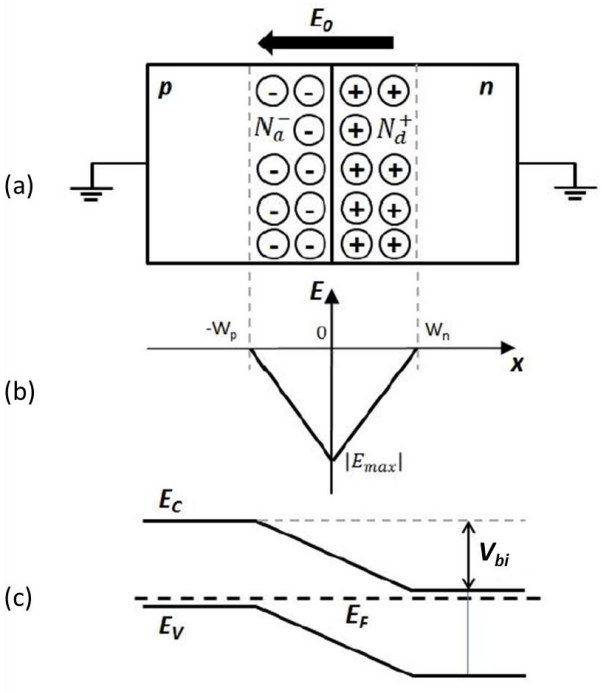

Figure 2.1. A schematic diagram of a p-n homo-junction at equilibrium showing dopant positions (a), an electric field profile of the p-n junction (b) and a schematic diagram of the band structure of the p-n junction (c).

Consequently, this electric field causes two drift currents. Both holes and electrons drift in the opposite direction to that of the diffusion component. Carrier diffusion that occurs due to the doping concentration difference balances out the drift of carriers, caused by the electric field. As a result, there is no net current flowing through the junction under equilibrium conditions. The built-in potential across the p-n junction [2], as shown in Figure 2.1.(c), can be estimated as:

$$V_{bi} = \frac{k_B T}{q_e} \ln\left(\frac{N_a N_d}{n_i^2}\right), \tag{2.1}$$

where k_B is Boltzmann's constant, *T* is the temperature, q_e is the charge of an electron, N_a and N_d are acceptor and donor concentrations respectively, and n_i is the intrinsic carrier concentration. Poisson's equation for the one-dimensional case describes the electrical field distribution:

$$\frac{dE}{dx} = \frac{\rho(x)}{\varepsilon}, \tag{2.2}$$

where ρ*(x)* is the space charge density and ε is the dielectric permittivity of the semiconductor. Charge density depends on the doping concentration, $\rho(x) = qN_d$ for the n-side and $\rho(x) = -qN_a$ for the p-side of the semiconductor. The junction can be doped asymmetrically in order to extend the electric field mostly in one side of the junction. For example, if the acceptor concentration is much greater than donor concentration, $N_a >> N_d$, the electric field will be located almost entirely in the n side of the junction.

As has been described above, an electric field and built-in voltage are generated when two semiconductors, with different dopants and concentrations, are brought into contact. The generated electric field can be further manipulated externally. By connecting the n-side of the semiconductor to the positive terminal and the p-side to the negative terminal and applying a reverse bias, V_R, an additional electric field is introduced. This field helps to expand the depletion region by forcing electrons in the n-side and holes in the p-side to move away from it. The total electric field inside the device is a sum of the initial electric field of the depletion region and the electric field created by the external reverse voltage.

A small reverse current, also known as leakage current or dark current, is always present in the reversed biased photodiode. The name 'dark current' comes from the fact that leakage current appears even under dark-room conditions when no light is incident on the photodiode. There are two main sources of this current: thermal generation of electron-hole pairs (EHPs), and reverse saturation current.

Thermal generation of EHPs is described by the Shockley-Read-Hall model [3]. EHPs spontaneously appear inside the depletion region due to lattice vibrations. Phonons, which are a representation of lattice vibrations, mediate the transfer of thermal energy to electrons in the valance band promoting them into the conduction band. The existing high electric field inside the depletion region will split the EHP and force the carriers to

drift away to neutral regions. The current density within the depletion region due to thermal generation is estimated as:

$$J_{tg} = \frac{q_e w n_i}{\tau_{tg}}, \tag{2.3}$$

q_e is the unit of electron charge, w is the width of the depletion region, n_i is the intrinsic carrier concentration, and τ_{tg} is the average time required for thermal generation of an EHP. The depletion width, *w*, increases with increased reverse bias. Hence, the current increases with higher reverse bias applied.

Reverse saturation current is caused by the diffusion of minority carriers from the neutral regions to the depletion region [4]. The concentration of minority carriers near the depletion region is significantly smaller than in the rest of the material. As a consequence of the resulting concentration gradient, electron and hole diffusion currents occur in the p-type and n-type sides, respectively. The electric field in the depletion region causes the diffusing carriers to be accelerated through to the opposite side with electrons travelling to the n-type side and holes to the p-type side.

The saturation current density can be expressed as:

$$J_s = q\left(\frac{D_e}{L_e N_d} + \frac{D_h}{L_h N_a}\right) n_i^2, \tag{2.4}$$

where q is the charge, D_e and D_h are the diffusion coefficients of electrons and holes, respectively, N_a, N_d and n_i are acceptor, donor, and intrinsic carrier concentrations, respectively, and L_e and L_h are the electron and hole diffusion lengths, respectively. The diffusion length is defined as the average length a carrier travels before recombination and is determined by the material properties of the semiconductor. Semiconductors with higher doping concentrations have shorter diffusion lengths due to greater recombination rates.

The total reverse current, combining the contributions described by Equations 2.3 and 2.4, is given by:

$$I_{rc} = \left[\left(\frac{D_e}{L_e N_d} + \frac{D_h}{L_h N_a}\right) n_i^2 + \frac{W n_i}{\tau_{tg}}\right] qA, \tag{2.5}$$

where *A* is the area of the semiconductor material cross-section. This total reverse current is known as leakage current.

The intrinsic carrier concentration depends on temperature [5]:

$$n_i \propto \exp\left(-{E_g}/{2k_BT}\right). \tag{2.6}$$

Hence, from Equation 2.5, the total reverse current depends on the temperature, *T*, owing to the fact that both currents depend on the intrinsic carrier concentration n_i and the area of the device. In addition, surface leakage and tunnelling contribute to electrical noise and increase the total amount of leakage current.

The leakage current also indicates the quality of the material and of the fabrication process. Minimising the level of dark current is very important for all optoelectronic devices. For instance, in complementary metal-oxide-semiconductor (CMOS) designed electronics, where the level of integration is often high, power dissipation is one of the reasons to keep the leakage current as low as possible. Power dissipation inevitably leads to a temperature increase which, in turn, affects device performance. In addition to increasing temperature, leakage current can affect the signal-to-noise ratio in optical receivers [6].

Photocurrent occurs as a result of EHPs generated by absorption of an incident photons. The mechanism is similar to that responsible for thermally-generated reverse current. An EHP is created within the depletion region if the energy of an incident photon is greater than the bandgap of the semiconductor. The electric field in the depletion region, enhanced by the applied reverse voltage, separates the EHPs and forces them to drift in opposite directions towards the neutral regions, thus generating photocurrent. If, however, photons are absorbed by the neutral region, the photocurrent produced is considerably lower as a large fraction of these diffusing carriers will recombine before reaching the depletion region.

The p-n junction is thus capable of forming a basic photodiode by allowing the creation of photocurrent from incident radiation. However, it can have two main practical disadvantages. First, the depletion region is relatively narrow. Therefore, a large diffusion component is created by photons absorbed outside the depletion region. Minority carriers, holes in the n-side and electrons in the p-side still have to diffuse into

the depletion region, where they will drift to the n-side or p-side respectively, to create a photocurrent. A relatively long time is required for carriers to diffuse into the depletion region because diffusion is originally a slow process (typically about 1 ns over 1 μm). Secondly, the carrier diffusion lengths limit the responsivity of the p-n junction photodiode. If the EHP is generated in the neutral region at a distance greater than the diffusion length from the depletion region, the minority carrier is likely to recombine. As such, a significant amount of carriers never reach the high field region.

The p-i-n photodiode configuration can eliminate these disadvantages. Figure 2.2 illustrates a typical p-i-n structure and the electric field profile of the device.

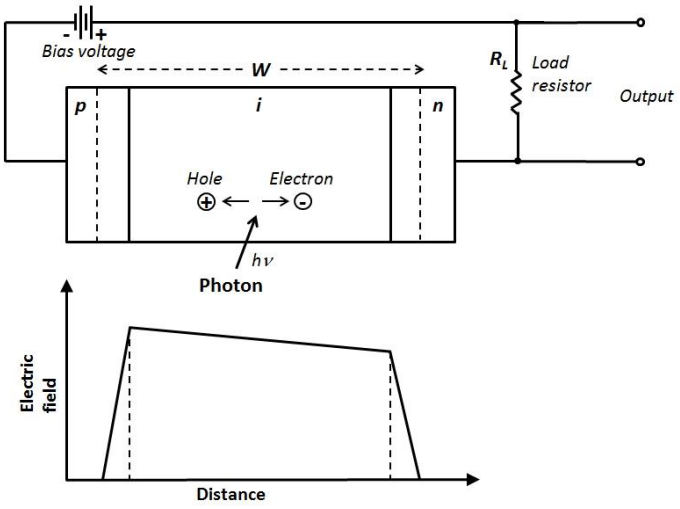

Figure 2.2. A schematic of a reverse biased p-i-n photodiode (top). An electric field diagram of the reversed biased p-i-n photodiode (bottom).

By inserting an intrinsic (undoped) 'i' region between the p and n regions, the width of the depletion region is increased. The p-i-n photodiode can be designed in such a way that the depletion region occupies almost the whole length of the diode. The intrinsic region, due to its low doping concentration, is depleted under external reverse bias conditions and it has high resistivity [7]. A high electric field within the 'i' region assists in collecting photo-generated EHPs. As a result, the drift current dominates over the diffusion component.

The responsivity of a photodiode is defined as:

$$R = \frac{I_{photo}}{P_{opt}} = \frac{q_e \eta}{h\nu} \tag{2.7}$$

where I_{photo} is the photogenerated current and P_{opt} is the power of incident light. It depends on the quantum efficiency, η, and the energy of an incident photon, $h\nu$ [8]. The quantum efficiency is the ratio between the number of EHPs created and the number of the incident photons. The fraction of incident photons that are absorbed within a semiconductor increases with the thickness of the material. In order to achieve a high detection efficiency, a low surface reflectivity is required. The surface reflectivity is determined by the material refractive index, hence anti-reflection layers are used to reduce the natural reflectivity of the semiconductor which is typically >30%. In order to increase the detection efficiency, the depletion region must be much greater than the absorption length, in order that all absorbed carriers are efficiently used in the photocurrent. Photogenerated carriers created outside the depletion region will result in a slower response as well as a reduced efficiency as carriers diffuse slowly and inefficiently into the depletion region, with many carriers recombining prior to reaching the depletion region. Hence, the responsivity increases with the increased intrinsic region which is depleted. However, increasing the absorption region can lead to a longer carrier transit time. The p-i-n photodiode uses an intrinsic layer with a high mobility to improve transit time but in many cases a compromise must be sought. Alternatively, resonant cavity structures can be used to minimise the device thickness, or by decoupling light absorption and carrier transport by using waveguide device structures.

2.3 Avalanche photodiodes

Avalanche photodiodes (APDs) exploit the impact ionisation phenomenon to generate internal gain. Impact ionisation is a multiplication process, which occurs when a single photogenerated carrier within the high electric field region gains enough kinetic energy to free bound electrons from atoms by collision, thus ionising the atoms. In other words, high-energy carriers, such as electrons, can excite a bound electron in the valance band and promote it to the conduction band. This leads to a creation of a hole in the valence band. These secondary carriers can also impact ionise, leading to further carrier multiplication. With sufficiently high field, it is possible to achieve gains of greater than 1000 [9, 10], however such a high level of gain can reduce the bandwidth of the device.

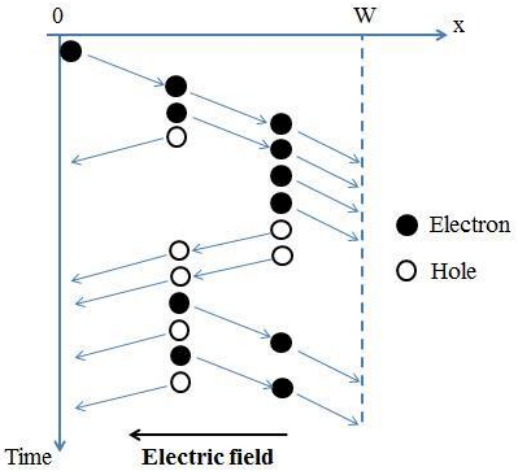

Figure 2.3. A schematic illustration of evolution of multiple impact ionisation processes. Here, w is the width of the multiplication layer and x is a direction of electron drift. In this example, there is a greater rate of electron impact ionisation than hole impact ionisation.

Figure 2.3 shows the avalanche multiplication process in which a single photogenerated carrier has been injected into the high electric field region and causes a chain of carrier collisions and excitations. This process strongly depends on the strength of the electric field and on the intrinsic material properties. The average number of EHPs created by electrons or holes during the multiplication process increases with the applied electric field.

The structure of an APD can be similar to a p-i-n photodiode, but in order to obtain more EHPs from the same input optical power it is operated at a voltage close to its breakdown voltage. The breakdown voltage is the voltage at which the current that flows across the photodiode dramatically increases as electron and hole impact ionisation is so great that a self-sustaining avalanche current is created leading to an infinite gain. Therefore, in comparison to a p-i-n photodiode, the external quantum efficiency can be improved by a multiplication factor, M, if the parameters of the absorption region are identical for both photodiodes. The external quantum efficiency of an APD can be expressed as:

$$\eta_{ext} = M \cdot (1 - R)(1 - e^{-\alpha w}), \tag{2.8}$$

where α is an absorption coefficient, w is the width of the multiplication region and M is defined as:

$$M = \frac{I_{photo} - I_{dark}}{I_{primary,photo} - I_{primary,dark}}, \tag{2.9}$$

where I_{dark} and I_{photo} are dark current and multiplied photocurrent when impact ionisation is observed and $I_{primary,dark}$ and $I_{primary,photo}$ are the primary dark current and primary photocurrent before the multiplication process has started.

In real devices, there is a fluctuation in the avalanche gain factor *M* due to the stochastic nature of the multiplication process [11]. As a result, even if *M* is relatively large, the actual value of gain that is realised in fibre optics receivers will be lower.

A high applied voltage (i.e. high electric field) is essential for APD operation so the carriers are able to gain enough kinetic energy to initiate the impact ionisation process. In addition, the carrier multiplication process is temperature dependent. As the temperature decreases, lattice vibration in the semiconductor is reduced. Hence, the ionisation coefficient will increase as the temperature decreases for a given electric field and the avalanche breakdown will occur at lower electric field values. The temperature dependence of the breakdown voltage can be described by the following formula:

$$\frac{V_{BD}}{V_{BD,RT}} = \gamma T \, , \tag{2.10}$$

where V_{BD} is a breakdown voltage, $V_{BD,RT}$ is a breakdown voltage at room temperature, *T* is a temperature of measurement and γ is a typical index of the particular device under observation. As Equation 2.10 states, the breakdown voltage increases linearly with increasing temperature [12-14]. The increment varies in different detectors, for example, in GaN photodiodes the increment can be 0.2 VK^{-1} [12] while for InGaAs/InP single-photon avalanche diode (SPAD) detectors it can be 0.17 VK^{-1} [14].

In many applications, photodetectors are required to detect a weak optical signal. In order to do so, they require high external quantum efficiencies and, typically, require external amplification. APDs can have an advantage over p-i-n photodiodes by using internal gain, which is particularly useful for optical pulses containing few photons.

2.4 Single-photon avalanche diode detectors

A wide range of modern applications, such as TCSPC applications and quantum information processing applications, require single-photon sensitivity, high detection

efficiency and the ability to operate at specific detection wavelengths. Therefore, several types of single-photon detectors have been used over the years. Among which there are photomultiplier tubes, microchannel plates, superconducting nanowires, quantum dot detectors, semiconductor avalanche photodiodes [15]. In this section, the working principles of SPADs will be described in more detail.

As mentioned previously, APDs have an internal gain. Hence, they can detect weak optical signals with an output current proportional to the input signal. Figure 2.4 illustrates the different operational modes of a photodiode. Ordinary photodiodes do not exhibit impact ionisation and have a gain of close to unity. APDs exhibit impact ionisation and show internal amplification, allowing them to detect weak optical signals when operated below breakdown voltage in so-called linear multiplication mode.

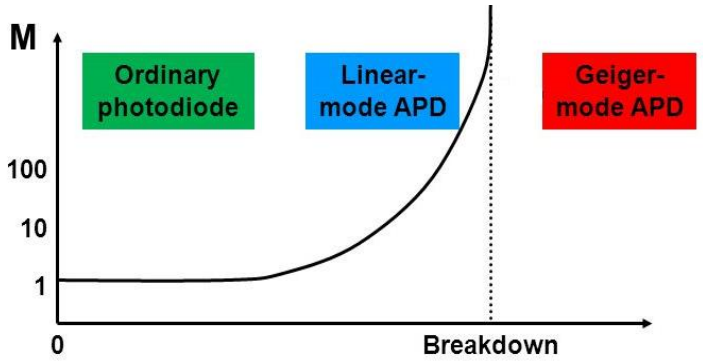

Figure 2.4. Different operation modes of the photodiode. The bias scale refers to reverse bias.

However, the internal gain of an APD operated in linear mode is generally not high enough to detect a single-photon. To overcome this problem, the APD is operated at a bias level above the breakdown voltage. This operational mode is known as the Geiger mode. In this mode, the APD works similar to the Geiger-Muller detectors [16] with a single incident photon capable of giving rise to an avalanche of carriers. Historically, the first SPAD was observed at the Shockley laboratory in the 1960s [17, 18] when the research group were investigating the physics of the avalanche breakdown of an APD. However, the first custom-made device was proposed and demonstrated 20 years later by Cova et al. in 1981 [19]. As shown in Figure 2.5, a SPAD operation is different from the linear amplification mode of APDs and can be explained by a working principle of a bistable circuit. In the OFF state, no current flows within the junction; the electric field is very high but there are no free carriers.

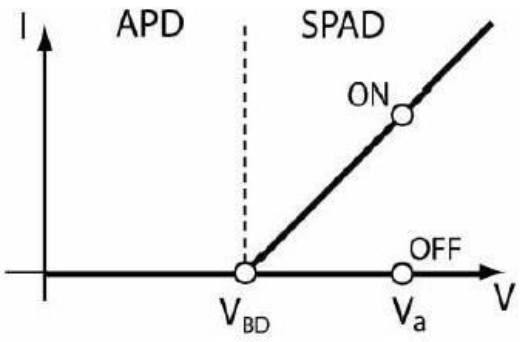

Figure 2.5. A schematic of a current-voltage characteristic of an APD and a SPAD. From Ref [19].

Under these conditions, even a single injected carrier can trigger the impact ionisation event, which leads to a self-sustaining avalanche and switches the device to the ON state. The self-sustaining current then flows through the junction until an external circuit, which decreases the applied voltage to a level below breakdown, quenches it. During the quenching process, the detector is insensitive and cannot detect any further incident photons. This time interval is called the detector dead-time and can be considered as a disadvantage of the SPAD device. The key characteristics of a SPAD are dark count rate (DCR) and afterpulsing phenomenon that contributes to DCR, single-photon detection efficiency (SPDE), noise equivalent power (NEP) and timing jitter. These will be described below.

In terms of performance, the DCR is one of the main limiting factors for a SPAD. It is very similar to the dark current in APDs. With no optical illumination present, a self-sustaining avalanche can be triggered by internal noise events. Such an event is known as a dark count and the DCR is defined as the average number of the randomly occurring noise events which cause a self-sustaining avalanche event during a 1 second time interval. Usually, it is quoted in counts/s or in Hz. In other words, the DCR represents a SPAD detector's internal noise contribution. There are several sources of DCR [20], [21]: thermally generated carriers, carrier tunnelling and carrier traps within the multiplication region.

The nature of the first two processes is the same as the one described previously for APDs. In the absence of illumination, avalanche events can occur due to thermally-generated EHPs within the active region of the device or as a result of carrier tunnelling. The afterpulsing phenomenon occurs when a carrier that has been trapped during the initial

avalanche multiplication process is later released and causes a new secondary avalanche event. This phenomenon will be discussed in more detail below and in Chapter 5.

DCR is strongly dependent on the device operating temperature. Spontaneous thermal generation decreases with temperature leading to a reduction of the DCR. Moreover, the DCR increases with the excess bias voltage. A high electric field enhances the impact ionisation rate and increases the probability of a self-sustaining avalanche being triggered by a thermally generated carrier. However, the high electric field also increases the SPDE of the detector for the same reason. In semiconductors, the generation-recombination (GR) centres are usually involved in the carrier transition between bands, particularly in Si. As a result of the high electric field, the Frenkel-Poole emission occurs leading to a field-assisted generation process [16]. In addition, tunnelling, which is a direct band-to-band transition, takes place at very high electric fields. Those effects cannot be eliminated by cooling the detector. Therefore, the electric field is maintained at the level that allows balance between the improved SPDE at high electric fields and increased DCR.

As mentioned above, afterpulsing is an important source of the detector noise in SPADs. Material defects and impurities create carrier traps that can capture carriers during the self-sustaining avalanche and release those carriers after the avalanche is quenched. These carriers are then capable of triggering new avalanches. In other words, the original avalanche pulse causes a new avalanche, called an afterpulse. To combat this effect, SPADs are typically desensitised for a period of time, known as a hold-off time, after a photon has been detected. During this time, the avalanche is quenched and traps have time to release their carriers without causing a detectable avalanche signal. The afterpulsing phenomenon is dependent on the excess bias, with the charge flow increasing with the excess bias voltage thus resulting in a higher probability of trapped carriers. Furthermore, the release time of the carriers exponentially increases with decreasing temperature. Consequently, SPADs employ longer hold-off times (i.e. dead times) when operated at cryogenic temperatures in order to avoid afterpulsing. As such, this introduces a severe limitation on the maximum count rate possible for a SPAD.

The SPDE of a SPAD depends on several factors: the absorption and primary EHP generation within the detector active area; the probability that the primary carrier reaches the avalanche region (in the case of a separate absorption region); and the avalanche triggering probability. The primary carrier should gain enough energy to trigger a self-

sustaining avalanche [22-24]. The avalanche triggering probability linearly increases with low excess bias voltages and then saturates to 1 at high excess bias voltages. The coupling efficiency describes the amount of the optical power coupled to the absorber of the device. Therefore, in order to increase the coupling efficiency and decrease reflection losses, the detector is usually coated with an anti-reflection layer. In addition, the thickness of the absorption layer and the material absorption coefficient are very important for the SPDE as it requires high external quantum efficiency, which was described previously in Equation 2.8.

The noise equivalent power (NEP) is defined as the signal power required to achieve a unity signal-to-noise ratio within one unit of integration time. A device with a higher sensitivity has a lower NEP. The following equation can be used for NEP estimation of a single-photon detector:

$$NEP = \frac{h\nu\sqrt{2DCR}}{SPDE} \tag{2.11}$$

where h is Planck's constant and ν is the incident light frequency.

The timing jitter of the device originates from the variance in the risetime of the detected event over many repeated events. The jitter is often characterised as the full-width half maximum (FWHM) timing jitter from the timing histogram. The SPDE, DCR and jitter can be determined using the TCSPC technique [14], which will be described in the next section. There are a few main sources of jitter [21]: the stochastic nature of the multiplication process, which means that there is a variation of the avalanche rise time. The origins of the jitter can come from several sources, however, in most devices, the lateral spread of the avalanche across the full active area of the device is the dominant factor [25]. This leads to improved jitter being generally found in smaller diameter devices. Increasing the excess bias also reduces the timing jitter because the carriers can reach the threshold level more rapidly and with less variance in the rise-time.

2.5 Time-correlated single-photon counting

The TCSPC technique is based on measuring a sequence of electrical pulses generated by a single-photon detector in response to incident illumination [26, 27], for example, a laser. Each detection event is recorded with respect to its arrival time. A master clock provides a reference signal, which is used to measure the photon arrival time, as shown in

Figure 2.6. The basic TCSPC setup is illustrated in Figure 2.7. A master clock sends two synchronised electronic pulses: one to the photon counting module to act as the START reference signal, and the other to trigger the photon source. Upon a detection event, the single-photon detector sends a STOP signal to the photon counting module. From this, the time elapsed between the laser pulse emission and the triggering of the SPAD by an incident photon is recorded. In the case of semiconductor SPADs, such a signal can be initiated by both a photon arrival and a dark event. The times of these detection events are usually recorded by a photon counting timing module over a significant amount of time (from sub-ms to several minutes depending on the application) and compiled into a timing histogram such as the example shown in Figure 2.8. Typically, the master clock sends a periodic START signal; however, this is not strictly necessary as the technique only measures the difference between the START and STOP signals.

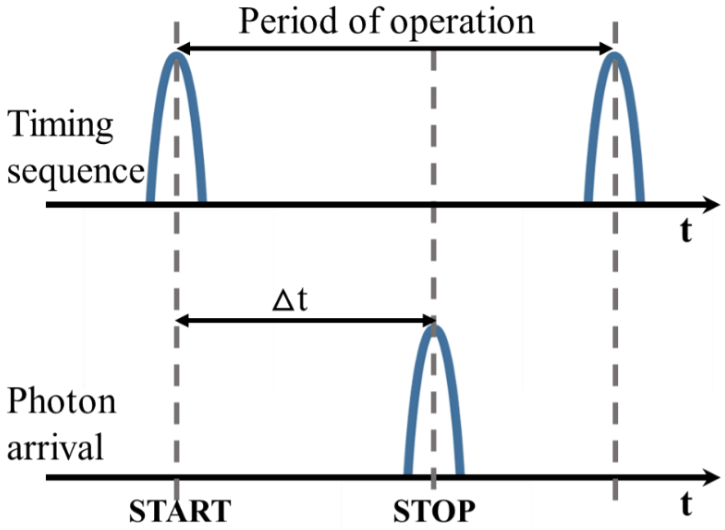

Figure 2.6. Timing schematic of the TCSPC operation. An external clock provides a START signal to the counting system indicating the emission of a laser pulse. The counting system then records the time, Δt, when it receives a STOP signal from the SPAD detector.

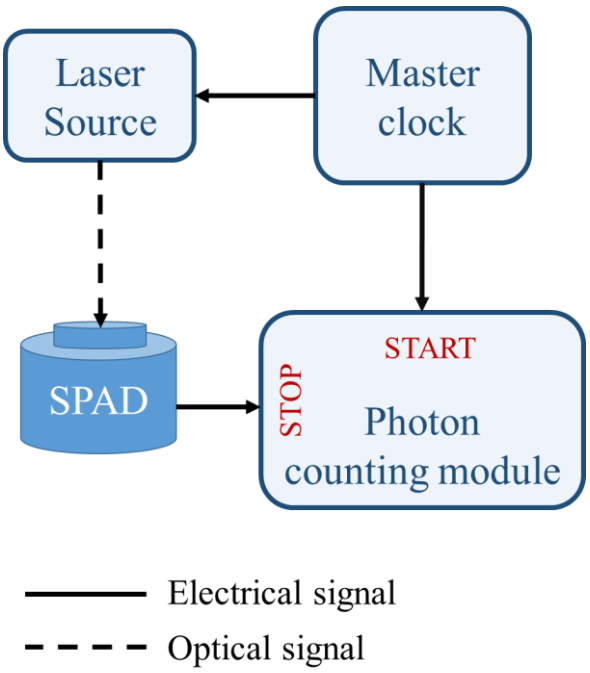

Figure 2.7. Schematic of a typical TCSPC setup. A master clock sends out two synchronised pulses: one is a reference START pulse for the photon counting card to start the timing measurement and the other one triggers the laser source to send a photon. A single-photon detector sends a STOP pulse each time an avalanche process is recorded, which has been initiated by either by a photon arrival or a dark event. (A typical timing histogram is shown in Figure 2.8).

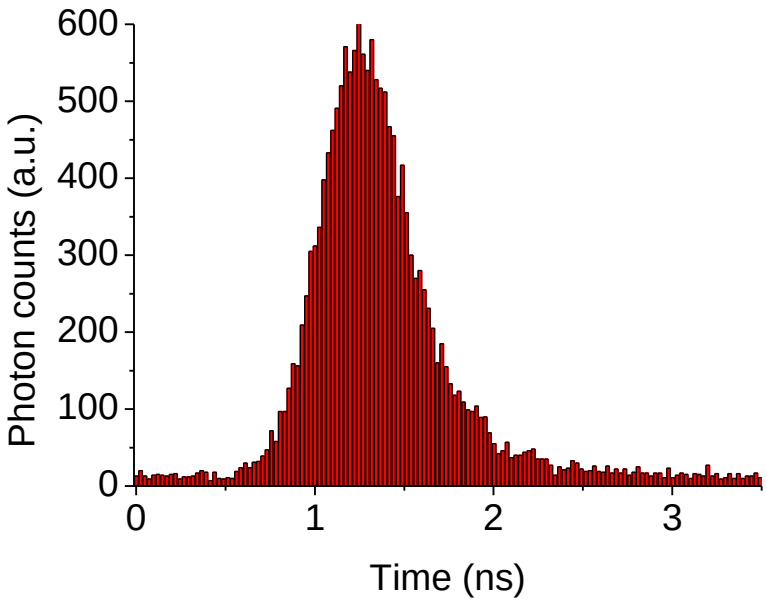

Figure 2.8 Example timing histogram of photon counts according to the arrival time. The value for each time bin represents the number of detection events recorded within that time range.

A histogram represents the number of detection events recorded for each time bin, or channel, over the duration of the measurement. Each histogram channel has a discrete width. Typically, a photon counting module has a set number of channels and a variable collection time window. As the total width of the histogram is given by this time window, varying the time window allows the bin width to be varied and, as a result, with a suitable choice of the time window, picosecond bin widths can be achieved. A longer window with wider time bins may be suited for low frequency dark count rate measurements where long acquisition times are required for data collection and the number of detection events is very low. In addition, long time windows and wider time bins may be required for LIDAR applications where one histogram may contain several peaks from different surfaces of the target.

The detection event pulses provided by a SPAD may vary in width and shape due to the stochastic nature of avalanche multiplication and also voltage recovery causing the bias levels of the SPAD to vary between measurements. If the voltage discriminator level (i.e. threshold) is set to a constant level, the arrival time will differ for different pulses. This is shown in Figure 2.9. This effect then introduces additional jitter into the timing histogram. To counteract this, the TCSPC technique uses the constant fraction discriminator (CFD) method [26]. This method uses a constant fraction of the pulse leading edge to trigger the STOP in photon counting card. This results in a constant timing point for pulses of a different amplitude.

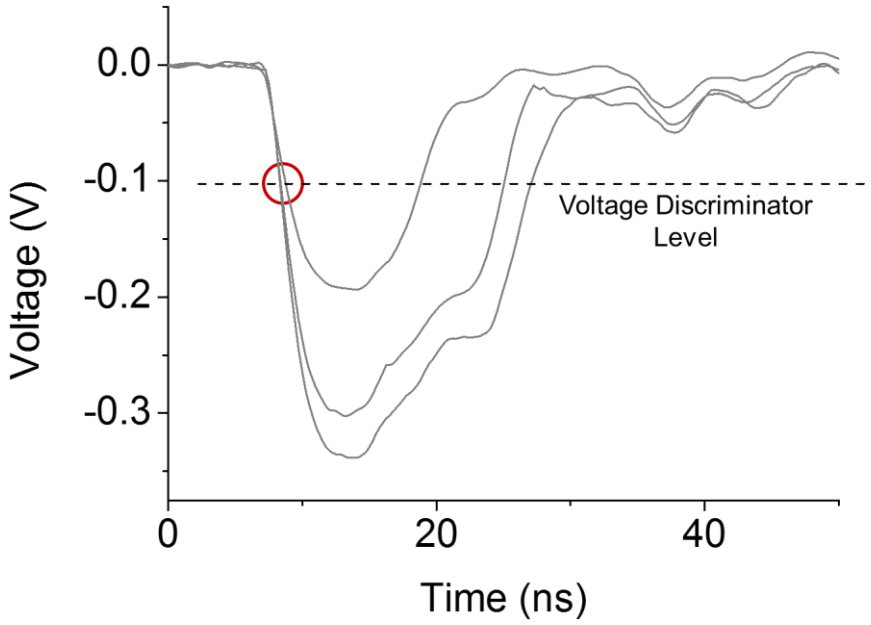

Figure 2.9. Example of several outputs from an electrically gated Ge-on-Si SPAD detector as seen on an oscilloscope. The voltage discriminator level (dashed line) is set at a value that enables all the output pulses to be registered. However, different amplitude pulses reach the discriminator level at slightly different times relative to the start of the measurement. This time difference adds to the timing jitter of the recorded histogram. The differing pulse amplitudes have been exaggerated for clarity.

The implementation of this technique is demonstrated in Figure 2.10. The detector output signal is split into two parts. The first part is inverted and delayed by δ, as shown in Figure 2.10 (a). The discriminator is set at a constant fraction, f, of the pulse amplitude V_a. The other part is attenuated to a maximum level of fV_a, as shown in Figure 2.10 (b). The sum of those pulses, as shown in Figure 2.10 (c) provides the zero crossing signal [26]. The photon-counting module stops the measurement and records the time upon receiving this signal.

The time-to-amplitude converter (TAC) within the photon counting timing module is capable of registering only one STOP per each START event. It requires a reset time, or "dead-time", during which no further stop pulses can be registered. The STOP rate of the TCSPC system must remain to less than 10% of the START repetition rate to avoid a problem called "pulse pile-up" and ensure a uniform distribution of detection probability

across the selected time range. When there are multiple photons present and only the first START-STOP pair is recorded per clock cycle the timing histogram appears to be skewed towards the start of the timing window. Such measurements are unreliable since the probability of recording a detection event in the latter time bins of the window is significantly reduced. There are algorithms available to correct this distortion [28], which add to the measurement uncertainty. However, to ensure that we safely avoid any pile-up effects, for all the measurements described in this Thesis, the STOP rate was maintained at less than 10% of the operating repetition rate.

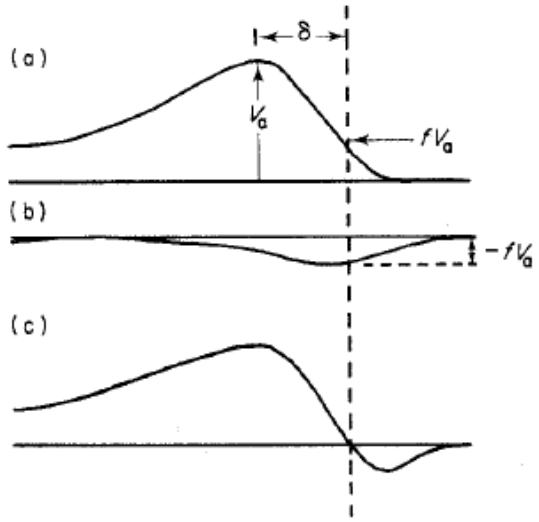

Figure 2.10. Illustration of the CFD operation. The original pulse is inverted and delayed by δ (a). The discriminator set at a constant fraction, f, of the pulse amplitude V_a. The original pulse is attenuated to fV_a (b). The sum of (a) and (b) pulses gives the zero crossing signal. CFD fires to stop the timing measurement upon receiving such a signal. From Ref. [26].

Single-photon counting is a Poissonian process where individual detection events can be considered as independent events. Equation 2.12 shows the discrete probability distribution of such a process:

$$P(n) = \frac{e^{-kt}(kt)^n}{n!}, \tag{2.12}$$

where n is the number of measured detection events over a time interval, t, and k is the expected number of the detection events per unit time. The number of expected incident photons is expressed as kt. Figure 2.11 illustrates the discrete probability distribution of a Poisson process for different values of the expected incident photons k.

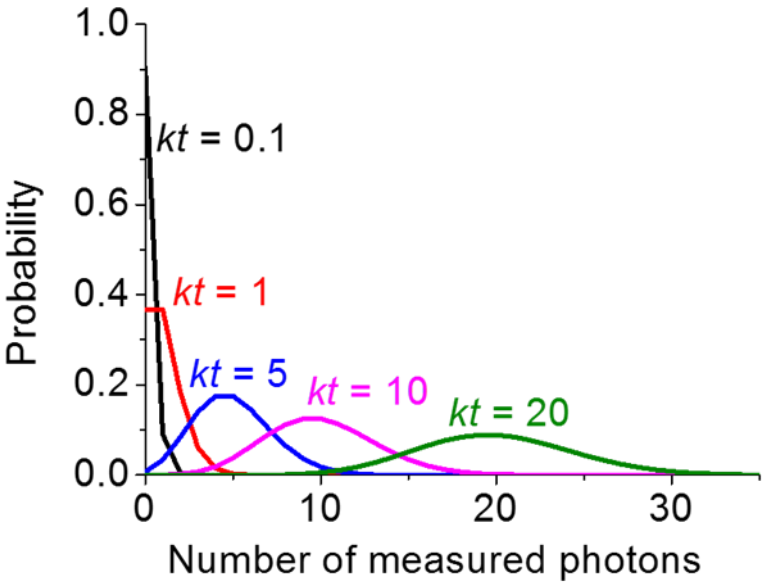

Figure 2.11 The Poisson probability distribution for different values of the expected incident photons kt.

The uncertainty associated with Poisson distribution can be estimated as a standard deviation which increases with the square root of the measured signal. This uncertainty is called a shot noise and provides the lower limit of the accuracy of the measuring light. Since the photon noise occurs due to the nature of the signal itself, it cannot be wholly eliminated and the only way to reduce the effect of this noise is to increase the signal (i.e. to collect more photons) by increasing the acquisition time. Due to the random occurrence of thermally-generated EHPs, dark count detection events also follow the Poisson distribution. In addition to photon noise, there are two more sources of noise in TCSPC systems: counts resulting from avalanches occurring within the detector due to internal carrier generations (i.e. dark counts) and due to trapped carriers released after initial avalanche (i.e. afterpulsing); and counts resulting from background illumination. Therefore, the total signal-to-noise ratio will have several components [29]. The signal-to-noise ratio in Poissonian statistics SNR_p, η, can be estimated as follows:

$$(SNR)_p = \eta_p = \frac{n_{p,i}}{\sqrt{n_{p,i}}} = \sqrt{n_{p,i}}\,, \tag{2.13}$$

where $n_{p,i}$ is the number of counts in the i-th time bin corresponding to the photon peak. Signal-to-background ratio (SBR), β, is defined as the ratio between the maximum peak

height and the background level of the histogram. Equation 2.14 shows the signal-to-background ratio.

$$SNB = \beta = \frac{n_{p,i}}{n_{b,i}}, \tag{2.14}$$

where $n_{b,i}$ is a number of background counts in the i-th time bin. The total signal-to-noise ratio is a sum of SNR_p and SBR:

$$SNR = \eta = \frac{n_{p,i}}{\sqrt{(n_{p,i} + n_{b,i})}} = \eta_p \sqrt{\left(\frac{\beta}{\beta + 1}\right)}, \tag{2.15}$$

According to Equation 2.15, the total SNR is close to the ideal one, SNR_p, only as long as the SBR is very high ($\beta \gg 1$). All the measurements described throughout this thesis were performed in a dark laboratory environment to minimise background illumination and with high $n_{p,i}$ compared to the dark counts in order to maximise the SNR of our TCSPC measurements. Appropriate collection times were employed to achieve thousands of counts in the histogram peak to minimise the photon noise.

In the next section, a review of the single-photon detectors available for SWIR region is provided in terms of the key parameters such as SPDE, DCR, timing jitter and NEP for future comparison with the experimental results described in Chapter 5 of this Thesis.

2.6 Single-photon detectors for the short-wavelength infrared region

The research presented in this Thesis is focused on the development of planar Ge-on-Si SPADs for single-photon detection in the SWIR region. All Si SPAD detectors and other single-photon detectors that operate in visible and near-infrared wavelength regions below 1 μm wavelength will not be considered. The next Chapter will present a detailed review of growth and fabrication techniques used to manufacture Ge-on-Si photodetectors. The challenges of photodiode integration onto Si photonic platforms will also be discussed along with the review of integrated InGaAs-on-Si APDs, Ge-on-Si APDs and SPADs. Here in this section, a review of alternative single-photon detectors that operate in SWIR will be presented in terms of detector performance and operating limitations.

2.6.1 InGaAs/InP SPADs

Indium gallium arsenide/indium-phosphide (InGaAs/InP) SPAD detectors have become an established technology for single-photon detection in the SWIR region. Over the past 40 years, extensive research and development have been conducted by many research groups including our group [14], which worked on the design, modelling and characterisation of these detectors. InGaAs/InP SPAD detectors operate at near-room or room temperatures and employ a separate absorption, grading, charge, and multiplication (SAGCM) structure [30] as shown in Figure 2.12.

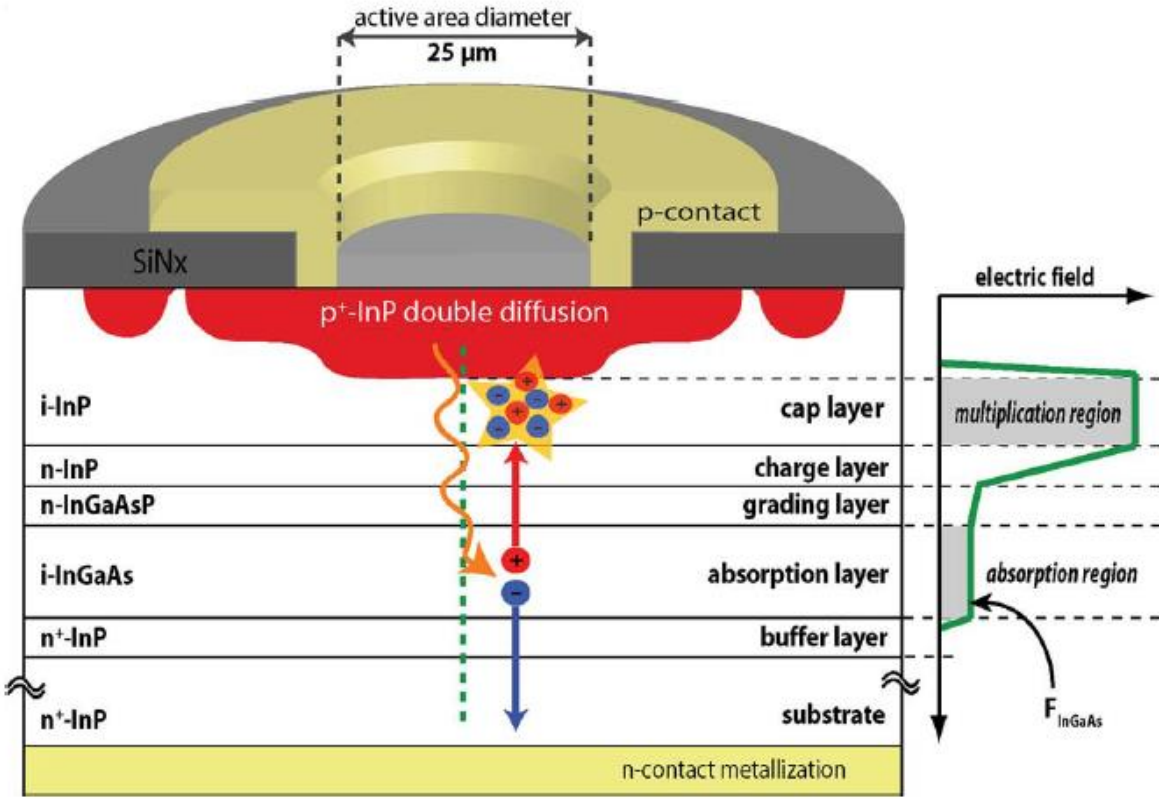

Figure 2.12 Typical planar SAGCM InGaAs/InP SPAD structure that incorporates double dopant diffusion and floating guard ring. The electric field along the centre of the active area is shown on the right. From Ref. [30]

As Figure 2.12 illustrates, photon absorption in these detectors occurs in the narrow band gap $In_{0.53}Ga_{0.47}As$ layer. The bandgap of this material is ~0.75 eV at 300 K [30], which corresponds to a wavelength of 1653 nm. Photogenerated electron-hole pairs are then separated by the electric field and holes drift to the wide-gap InP multiplication layer (E_G ~1.35 eV at 300 K) where it initiates a self-sustained avalanche. Introducing an

additional charge layer between the absorption and multiplication regions allows a low electric field to be maintained in the InGaAs absorption layer and a high electric field in the InP multiplication layer. A low electric field in the absorber layer is required to avoid the tunnelling effect; however, the electric field has to be sufficiently high in order to facilitate carrier transport into the multiplication region. A high electric field in the multiplication region is required for photogenerated holes to gain enough kinetic energy to initiate impact ionisation processes. A grading layer is utilised to mitigate the carrier pile-up effect at the hetero-interface, particularly holes in the valance band leaving the absorption region. This effect arises due to the valance band discontinuity of ~0.4 eV between InGaAs and InP [31, 32]. Figure 2.13 shows the schematic diagram of the energy band structure of the InGaAs/InP photodetectors.

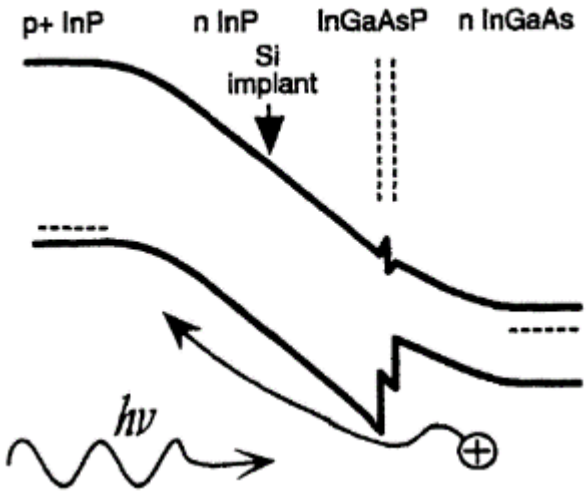

Figure 2.13 Schematic energy band diagram of the InGaAs/InP avalanche photodiode detector. From Ref. [32].

InGaAs/InP SPADs are fabricated using the double p-type Zn diffusion method first introduced in 1992 by *Liu et al.* [33]. This approach allows for the fabrication of planar geometry SPADs, which benefit from reduced edge effects [34] due to the electric field being confined to the centre of the active area of the device. The device structure reported in [33] also introduced floating guard rings (FGR), which reduce edge breakdown and surface electric fields and a stepped junction edge formed by the double Zn diffusion that confines the high electric field to the centre of the device. Figure 2.14 illustrates the difference between the electric field profile in the centre and near the edge of the detector created by the stepped junction in the InGaAs/InP SPAD reported in [35].

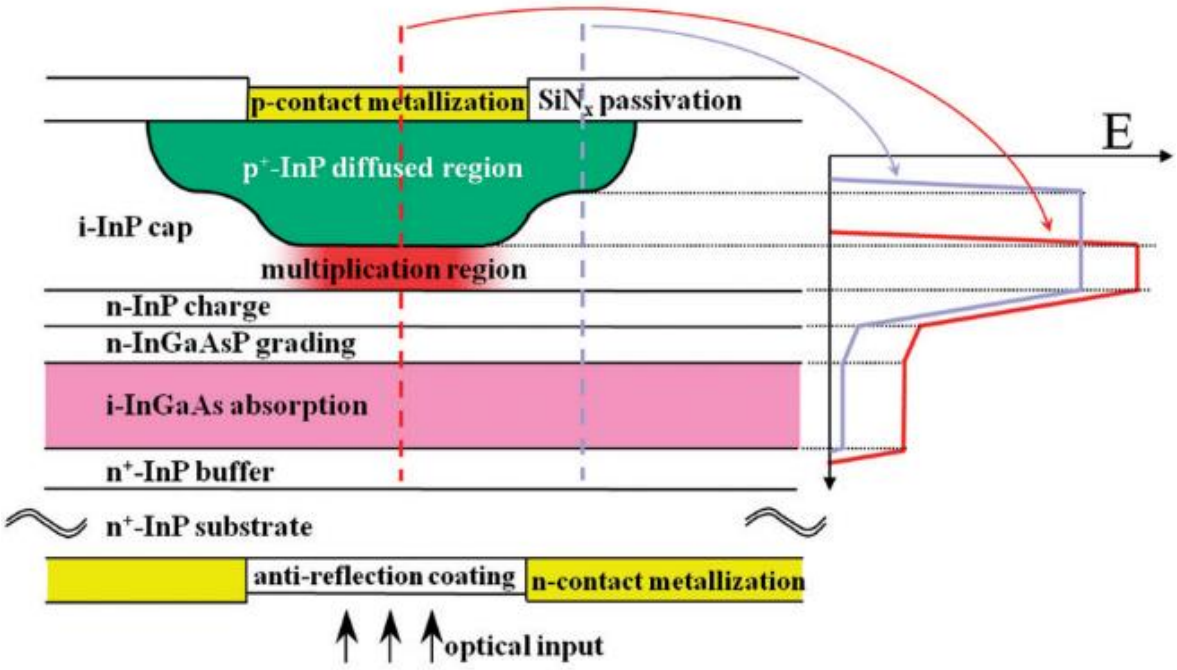

Figure 2.14 Schematic diagram of a diffused-junction planar-geometry SPAD structure reported in [35]. The electric field profiles (right) show that the peak field intensity is lower in the peripheral region of the diffused p-n junction than it is in the centre of the device.

Single-photon performance using an InGaAs/InP APD was first demonstrated in 1994 by *Zappa et al.* [32]. The authors were using an InGaAs/InP APD, produced by EG&G, of a 50 μm diameter and a breakdown voltage of ~90-110 V at room temperature. These detectors were operated in Geiger mode, with the APDs biased above breakdown for short time intervals of ~250 ns spanning the duration of the gate pulse [32]. A maximum SPDE of 1%, a minimum NEP of 1×10^{-14} $WHz^{-1/2}$ and a jitter FWHM of ~1 ns were reported for 6 V excess bias at 150 K temperature of operation under 1310 nm illumination. In addition, they measured an exponential dependence of the DCR with the operating temperature. Later, in 1996 the same research group reported an improved timing jitter of ~200 ps and a lower NEP of 2.7×10^{-16} $WHz^{-1/2}$ using a commercially available Fujitsu InGaAs/InP APD of 30 μm diameter operated at 2 V excess bias and at 77 K temperature of operation [36]. *Hiskett et al.* using two commercially available Fujitsu InGaAs/InP APDs of 80 μm and 30 μm diameters reported similar results in 2000 [21]. Their measurements were performed across a range of temperatures between 77 K and 225 K; reporting a maximum SPDE of ~16% for both devices at 140 K temperature of operation for 80 μm diameter device and at 180 K for 30 μm diameter detector. The detection

efficiency of the 30 μm diameter detector was effectively zero at temperatures below 150 K because the device could not achieve punch-through. Punch-through occurs when the electric field expands into the absorption region. allowing photogenerated carriers to drift into the multiplication region. The lowest NEP of 4.0×10^{-16} WHz$^{-1/2}$ was reported for the 80 μm diameter detector at 3 V of excess bias operated at 77 K. This detector displayed a jitter of ~400 ps. However, the authors recommended operation of the 80 μm diameter detector at 5 V excess bias to exploit both the low jitter of 250 ps and the low NEP of 4.4×10^{-16} WHz$^{-1/2}$.

Although the first single-photon counting was demonstrated using commercially available APDs, not every APD can be operated as a SPAD. There is a set of criteria that have to be satisfied for an APD to be capable of single-photon detection. First, there has to be a significant difference between the breakdown voltage V_{bd} and the punch through voltage V_{pt}. As mentioned above, V_{bd} decreases with temperature while V_{pt} remains the same over a wide temperature range because it only depends on the doping concentration levels. If the difference is too small at lower temperatures, photogenerated carriers in the InGaAs layer will fail to reach the InP multiplication region before detector breakdown, as observed in [21]. Secondly, linear mode APDs require thinner multiplication layers since the gain-bandwidth product is inversely proportional to the thickness of the multiplication layer and thinner multiplication layers lead to more deterministic avalanche processes [7]. Finally, the gain must be in the region between 10 and 20 [7, 37] for InGaAs/InP APDs to reach an optimum signal to noise ratio in fibre optic receivers that use amplifiers [11]. In SPADs, on the other hand, thicker multiplication regions of ~1 μm lead to significantly increased breakdown probability [38].

In 2006, two research groups proposed customised designs of InGaAs/InP SPADs for single-photon detection at a 1550 nm wavelength [14, 37]. *Pellegrini et al.* reported the design, fabrication, and performance of 10 μm diameter planar InGaAs/InP detectors that used a similar structure to Figure 2.12 but with graded regions composed of several sublayers with intermediate bandgaps to mitigate the large valence band offset between InGaAs and InP [14]. These detectors demonstrated a maximum SPDE of 10% at a wavelength of 1550 nm operated at 10% relative excess bias and a temperature of 200 K, a minimum NEP of 6×10^{-16} WHz$^{-1/2}$ and a timing jitter of 450 ps. A similar design was proposed by *Tosi et al.* [37], who reported a timing jitter of 65 ps with a DCR of 400 k count/s. Unfortunately, these authors did not present a value of SPDE and NEP for

those detectors. Later, in 2007, the performance of InGaAs/InP SPADs was further improved by *Liu et al.* [39], who demonstrated an SPDE of 45% at 1310 nm wavelength, a DCR of 12 k count/s and an NEP of 4.5×10^{-17} $WHz^{-1/2}$ at 200 K operating temperature. The authors used a 40 μm diameter SPAD operated in a gated mode with a gate width of 4 ns and a repetition rate of 10 kHz. Similar results at a wavelength of 1550 nm were presented by *Itzler et al.* in 2007 - 2008 [38, 40]. A maximum SPDE of up to 45%, a minimum DCR of 3 kcount/s, and minimum timing jitter of 30 ps at 200 K operating temperature were demonstrated [38]. The authors also reported an SPDE of 20% while exhibiting a DCR of 10 kcount/s and a timing jitter of 100 ps at 200 K temperature of operation [38]. A DCR of less than 200 count/s for a 15% SPDE was reported at a temperature of operation of 220 K [40].

Although InGaAs/InP SPAD detectors demonstrate high SPDEs, low jitter and can operate near room temperatures, or at temperatures compatible with thermoelectric cooling, the effect of afterpulsing still remains a major drawback for these SPADs. As mentioned before, afterpulsing occurs as a result of carriers trapped during the initial avalanche being released and triggering the secondary avalanche, therefore adding to DCR. Research has been carried out towards reducing these detrimental effects. Different electrical biasing techniques such as gated mode with longer dead-times, and free-running mode have been proposed.

In gated mode, longer dead-times, during which the detector gate is off in order to allow trapped carriers to be released, limit the maximum repetition rate. In 2012, *Tosi et al.* presented InGaAs/InP SPADs operated in gated mode at high count rates of up to 1 MHz and at a temperature of 225 K [41]. These detectors exhibited an SPDE of 25% at a detection wavelength of 1550 nm at a 5 V excess bias as well as a DCR below 100 kcount/s and a timing jitter of 90 ps. Later in 2014, *Tosi et al*. reported improved results demonstrating low DCR of ~1 k count/s at 225 K and 5 V of excess bias, SPDE of 30% at 1550 nm wavelength and a timing jitter of 90 ps [42]. These results were improved by operating the detector at lower count rate of 10 kHz.

Free-running mode operation, in which an external circuit is used to generate a standard output pulse upon the avalanche arrival and quenches the avalanche bringing the bias below breakdown voltage. A first free-running mode operated InGaAs/InP SPAD was reported by *Warburton et al.* in 2009 [43]. This mode of operation requires SPADs that exhibit low DCRs. In Reference [43] a Princeton Lightwave InGaAs/InP SPADs of a

25 μm diameter exhibited SPDEs of up to ~3% at 1550 nm wavelength and at 270 K temperature of operation, a minimum timing jitter of ~500 ps and an NEP of ~1×10^{-14} $WHz^{-1/2}$ at room temperature. The authors reported high count rates of up to 4 Mcount/s. Gated mode operation using the same detector was impossible at room temperature due to the prohibitively high DCR. New generation devices from Princeton Lightwave demonstrated DCRs of 40 k count/s and NEPs of 1×10^{-15} $WHz^{-1/2}$ under identical operation conditions [44]. At 210 K temperature of operation, these SPADs demonstrated an NEP of ~5×10^{-15} $WHz^{-1/2}$at 1550 nm wavelength, which is comparable to the values obtained employing gated mode. In 2014, *Korzh et al.* reported a DCR as low as 1 count/s and an SPDE of 10% while operating at a temperature of 163 K, which corresponds to NEP of [45]. Later in 2015, *Jiang et al.* reported similar results in a range of temperatures between 240 K and 160 K with the lowest NEPs of 1.9×10^{-16} $WHz^{-1/2}$ and 1.8×10^{-18} $WHz^{-1/2}$ at 240 K and 160 K respectively [46].

A number of references report different gating techniques for InGaAs/InP APDs in high count rate quantum communication applications such as sinusoidal [47-50], sine-wave [51, 52], and gate frequency generated harmonics to suppress the gate transient [53]. However, the afterpulsing phenomenon remains the main drawback of InGaAs/InP SPADs and research is still going on towards minimising DCR and timing jitter while achieving high SPDEs, and high count rates.

Despite their limitations, InGaAs/InP SPADs represent the state-of-the-art of single-photon detectors for the SWIR region and are currently available from commercial companies such as Micro Photon Devices and Princeton Lightwave. The SPDEs of commercial InGaAs/InP SPADs are limited to < 30% due to afterpulsing.

In contrast to InGaAs/InP SPADs, afterpulsing Si SPADs is less evident [54] and one of the reasons for that is that Si SPAD detectors are typically operated at near-room temperatures. Indeed, detectors that benefit from good multiplication properties of Si, use Ge for absorption of photons of up to 1550 nm wavelength and not restricted by afterpulsing can become an alternative technology to commercial InGaAs/InP SPADs. The research towards Ge-on-Si was enabled by progress in heteroepitaxial growth of Ge on Si and it is at the early stages at the moment. Chapters 4 and 5 of this Thesis will present the design, fabrication and characterisation of the first planar geometry Ge-on-Si SPADs operated in the SWIR region.

2.6.2 Superconducting nanowire single-photon detectors

In 1911, Kamerlingh Onnes discovered the phenomenon of superconductivity. At low temperatures, the resistance of some metals drops to zero below a particular temperature known as the critical temperature, T_c [55]. This phenomenon has been used to develop a new class of single-photon detectors. It has been found that absorption of a photon perturbs the electrical properties of the superconducting metal. The Niobium Nitride (NbN) superconducting nanowire single-photon detector (SNSPD), which is sensitive in the visible and infrared wavelength regions was developed and reported for the first time by *Gol'tsman et al* in 1991 [56]. Figure 2.15 illustrates the basic operation principle of the SNSPD.

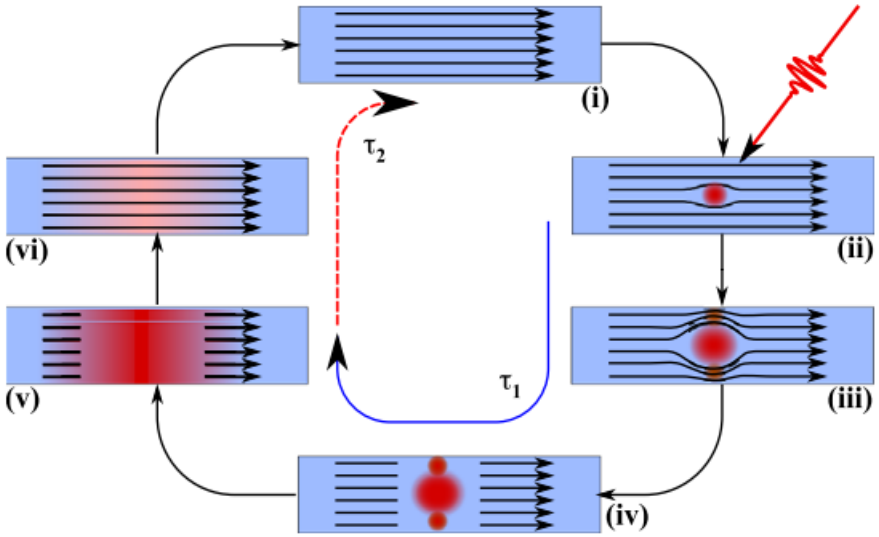

Figure 2.15 The basic operation principle of the SNSPD illustrating the detection cycle. The diagram is described fully in the main text. From Ref. [57].

The superconducting nanowire is DC biased just below the critical current density level and operated well below the critical temperature, T_c (ii). The absorption of the photon with energy much greater than the superconducting energy gap, $\hbar\omega \gg 2\,\Delta$, leads to a local nonequilibrium perturbation creating a large number of excited hot electrons. Hence, the temperature increases above T_c, creating a small resistive hotspot. (iii) This forces the supercurrent to flow along the periphery of the hotspot, which increases the local current density around the hotspot beyond the superconducting critical current

density. (iv) As a result, a resistive barrier forms across the narrow NbN nanowire [56]. (v) The resistive barrier expands along the nanowire aided by the DC bias [58] until the current flow is stopped. The voltage pulse with a rise time, τ_1, and the decay time, τ_2, can be recorded. (vi) The external circuit shunts the bias to allow the resistive region to subside. Once the nanowire is fully superconducting again the device is biased again, ready to receive the next photon event (i).

The nanowire has to be very narrow for the resistive spot to form across the width of the wire and prevent the current from flowing. However, light coupling into such a small area is challenging. Therefore, the nanowire is arranged as a meander to maximize the detection efficiency. The active area of such detectors can be up to 20 μm × 20 μm [59]. The schematic of the meander and the scanning electron microscopy (SEM) image of an SNSPD are shown in Figure 2.16 [15, 60].

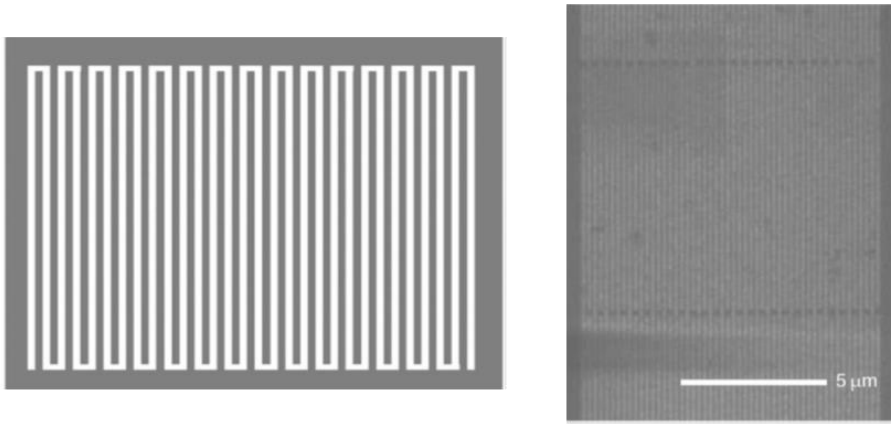

Figure 2.16 (a) A schematic of the meander design of a superconducting nanowire single-photon detector (SNSPD). From Ref. [15]. (b) A scanning electron microscope image of an SNSPD. From Ref. [60].

Although early SNSPDs demonstrated low SPDEs of less than 3% at 1550 nm wavelength [59, 61, 62], they showed a low jitter with a jitter of 68 ps reported *Verevkin et al.* in 2002 [61] using a 10 μm × 10 μm meander and 18 ps [62] reported later in 2005 by *Pearlman et al.* using a similar structure.

Device structures such as waveguide integrated SNSPDs [63] and optical cavity integrated SNSPDs [64] have been proposed to improve the SPDE of these detectors. Figure 2.17 illustrates the proposed design structures.

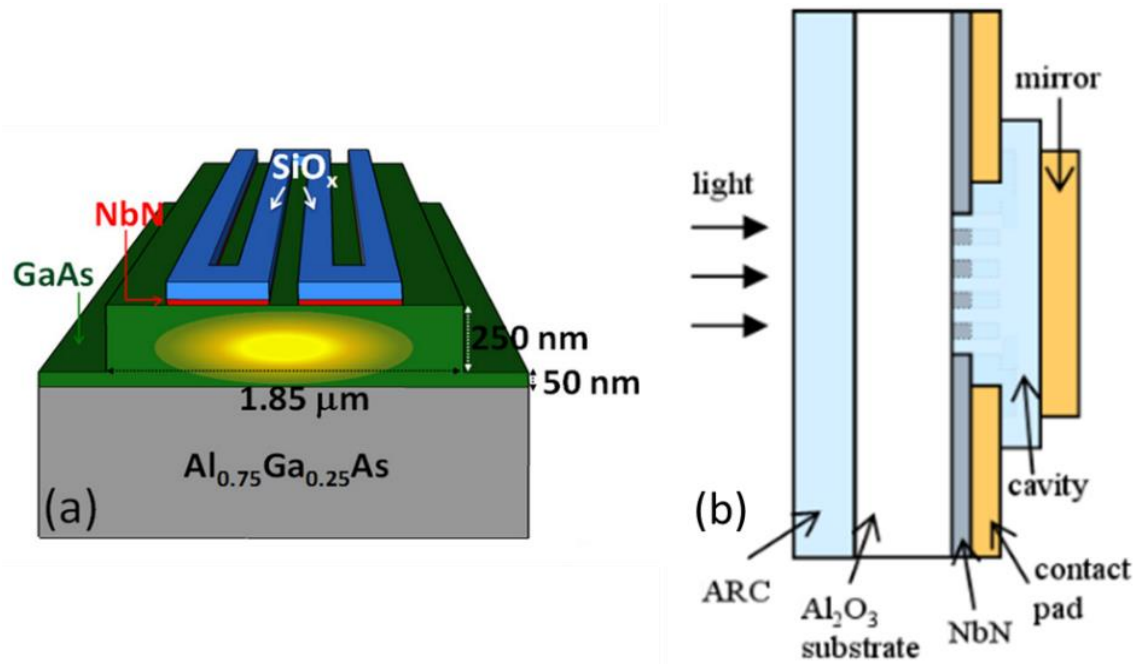

Figure 2.17 A schematic of different SNSPD structures: (a) waveguide integrated SNSPD. From Ref. [63], (b) An SNSPD integrated with an optical cavity and anti-reflective coating to improve absorption efficiency. From Ref [64].

Indeed, *Rosfjord et al.* have demonstrated an SPDE of 57% at a detection wavelength of 1550 nm using an SNSPD integrated with an optical cavity and operated at 1.8 K [64]. *Miki et al.* also reported SPDEs of ~24 – 28% (~23 – 40%) at a detection wavelength of 1550 nm (1310 nm) using optical cavity SNSPD configuration [65]. Later, in 2017, Zhang et al. reported a structure incorporating a distributed Bragg reflector mirror on a Si substrate [66]. These devices were operated at 2.1 K and have demonstrated an SPDE of 90% at a detection wavelength of 1550 nm, a DCR of 10 count/s and a timing jitter of 79 ps. The waveguide integrated SNSPD reported by *Sprengers et al.* has demonstrated an SPDE of only 3.4% at 1300 nm wavelength, a DCR of ~100 kcount/s and a jitter of 60 ps. Later in 2019, *Shibata et al.* reported an NbN SNSPD integrated on a Si photonics platform and demonstrated an SPDE of 32%, a DCR of 95 count/s, a jitter of 75 ps and a low NEP of 3.6×10^{-18} $WHz^{-1/2}$ at a detection wavelength of 1550 nm.

Different superconducting materials have been used to improve the detection efficiency. *Marsili et al.* reported the amorphous tungsten silicide $W_{0.75}Si_{0.25}$ (WSi) SNSPD, which demonstrated an SPDE of over 90% at 1550 nm detection wavelength, a DCR of ~1 k count/s and a timing jitter of ~150-200 ps [67]. However, these WSi devices were

operated at a temperature of 1 K due to a lower critical temperature than NbN nanowires. In 2014, *Verma et al.* reported a WSi SNSPD with an SPDE of 78% at a detection wavelength of 1310 nm operated at 2.5 K, a DCR of 1 k count/s and a timing jitter of 191 ps, which was limited due to the readout circuitry [68]. Later in 2015, the same research group reported on MoSi SNSPD operated at 0.7 K that demonstrated high SPDE of 87% at 1542 nm wavelength, a DCR of less than 100 count/s and a FWHM timing jitter of 76 ps [69]. At a temperature of 2.3 K, this SNSPD demonstrated a slightly lower detection efficiency of ~80%. In 2017, *Zaden et al.* reported a NbTiN SNSPD operated at ~2.5 K demonstrated SPDE of ~90% for a range of detection wavelengths between 1310 and 1625 nm [70].

Although SNSPDs demonstrate better performance compared to InGaAs/InP SPADs: lower timing jitter, higher SPDEs and similar DCR, these detectors require bulky cryogenic systems that are able to achieve operating temperatures below 3 K [71]. Such cryogenic systems make SNSPD highly expensive and impractical for some applications that require mobile and compact detectors. Low operating temperatures along with the challenges related to the light coupling into a small area (10 μm × 10 μm) of the detector remain the main disadvantages of these detectors.

2.7 Summary

In this Chapter, a review of the operating principle of semiconductor-based photodiodes has been presented, with a focus on the detectors that employ impact ionisation phenomenon for internal signal multiplication. Different factors such as properties of the material, device structure, design and temperature of operation have to be carefully considered while designing a SPAD. A brief review of the TCSPC technique, a technique of choice in applications such as quantum communications, time-resolved fluorescence, long-range imaging, and underwater imaging, have been presented. This technique allows measurements of picosecond optical transients and, for example, can provide good depth resolution in LIDAR and depth imaging applications. In addition, the key characteristics of single-photon detectors such as SPDE, DCR, timing jitter and NEP have been discussed.

Different single-photon detectors operated in the SWIR region have been discussed. A brief overview of the main advantages and constraints of these detectors have been presented. These factors have to be considered relative to the requirements of a potential

application to select the most suitable detector. At the moment, there are two mature single-photon detection technologies operating in SWIR: InGaAs/InP SPAD detectors and SNSPDs. InGaAs/InP SPADs offer low DCRs, low timing jitters and SPDEs of up to a maximum of 45% at a detection wavelength of 1550 nm. These detectors operate at temperatures compatible with Peltier cooling systems. Therefore, InGaAs/InP SPADs remain the detector of choice in applications that require compact and mobile detectors such as, for example, long-range imaging. On the other hand, SNSPDs provide significantly higher SPDEs of up to 90% at 1550 nm wavelength, improved timing jitter of down to 18 ps and low DCR. Although these detectors demonstrate excellent performance, SNSPDs require cryogenic temperatures of below 3 K for operation. This significantly limits the range of application suitable for these detectors.

An alternative semiconductor material for single-photon detection at telecommunication wavelengths is Ge. Integration of Ge photodetectors into Si platform along with the potential benefits and challenges of creating Ge-on-Si SPADs will be discussed in the next Chapter. A detailed review of the Ge-on-Si SPADs will be also be given in this Chapter.

2.8 References

1. C. Kittel, *Introduction to solid state physics*. Vol. 8. 1976: Wiley New York.

2. W. Shockley, *The Theory of p-n Junctions in Semiconductors and p-n Junction Transistors.* Bell System Technical Journal, 1949. **28**(3): p. 435-489.

3. W. Shockley and W.T. Read Jr, *Statistics of the Recombinations of Holes and Electrons.* Physical Review, 1952. **87**(5): p. 835-842.

4. R.C. Dorf, *The electrical engineering handbook*. 1997: CRC press.

5. T.P. Pearsall and M.A. Pollack, *Chapter 2 Compound Semiconductor Photodiodes*, in *Semiconductors and Semimetals*, W.T. Tsang, Editor. 1985, Elsevier. p. 173-245.

6. K. Gerd, *Optical Fiber Communications*. 2 ed. 1991, New-York: McGraw-Hill.

7. G.P. Agrawal, *Fiber-Optic Communication Systems*. 3 ed. 2002: John Wiley & Sons, Inc.

8. H.J. Dutton, *Understanding optical communications*. 1 ed. 1998, IBM Corporation: Prentice Hall PTR New Jersey.

9. K. Nishida, K. Taguchi and Y. Matsumoto, *InGaAsP heterostructure avalanche photodiodes with high avalanche gain.* Applied Physics Letters, 1979. **35**(3): p. 251-253.

10. O. Kim, S. Forrest, W. Bonner and R. Smith, *A high gain In0. 53Ga0. 47As/InP avalanche photodiode with no tunneling leakage current.* Applied Physics Letters, 1981. **39**(5): p. 402-404.

11. R. McIntyre, *Multiplication noise in uniform avalanche diodes.* IEEE Transactions on Electron Devices, 1966(1): p. 164-168.

12. R. Aggarwal, I. Melngailis, S. Verghese, R. Molnar, M. Geis, and L. Mahoney, *Temperature dependence of the breakdown voltage for reverse-biased GaN p–n–n+ diodes.* Solid State Communications, 2001. **117**(9): p. 549-553.

13. K. Kajiyama and H. Kanbe, *Temperature dependence of avalanche breakdown voltage in Si p-n junctions.* Journal of Applied Physics, 1976. **47**(6): p. 2744-2745.

14. S. Pellegrini, R.E. Warburton, L.J. Tan, J.S. Ng, A.B. Krysa, K. Groom, J.P. David, S. Cova, M.J. Robertson, and G.S. Buller, *Design and performance of an InGaAs-InP single-photon avalanche diode detector.* IEEE Journal of Quantum Electronics, 2006. **42**(4): p. 397-403.

15. G. Buller and R. Collins, *Single-photon generation and detection.* Measurement Science and Technology, 2009. **21**(1): p. 012002.

16. S. Cova, M. Ghioni, A. Lotito, I. Rech and F. Zappa, *Evolution and prospects for single-photon avalanche diodes and quenching circuits.* Journal of Modern Optics, 2004. **51**(9-10): p. 1267-1288.

17. A. Goetzberger, B. McDonald, R.H. Haitz and R.M. Scarlett, *Avalanche Effects in Silicon p—n Junctions. II. Structurally Perfect Junctions.* Journal of Applied Physics, 1963. **34**(6): p. 1591-1600.

18. R.H. Haitz, *Mechanisms Contributing to the Noise Pulse Rate of Avalanche Diodes.* Journal of Applied Physics, 1965. **36**(10): p. 3123-3131.

19. S. Cova, A. Longoni and A. Andreoni, *Towards picosecond resolution with single-photon avalanche diodes.* Review of Scientific Instruments, 1981. **52**(3): p. 408-412.

20. A. Lacaita, P. Francese, F. Zappa and S. Cova, *Single-photon detection beyond 1 μm: performance of commercially available germanium photodiodes.* Applied Optics, 1994. **33**(30): p. 6902-6918.

21. P.A. Hiskett, G.S. Buller, A.Y. Loudon, J.M. Smith, I. Gontijo, A.C. Walker, P.D. Townsend, and M.J. Robertson, *Performance and design of InGaAs/InP photodiodes for single-photon counting at 1.55 μm.* Applied Optics, 2000. **39**(36): p. 6818-6829.

22. R.J. McIntyre, *The distribution of gains in uniformly multiplying avalanche photodiodes: Theory.* IEEE Transactions on Electron Devices, 1972. **19**(6): p. 703-713.

23. R.J. McIntyre, *On the avalanche initiation probability of avalanche diodes above the breakdown voltage.* IEEE Transactions on Electron Devices, 1973. **20**(7): p. 637-641.

24. W.G. Oldham, R.R. Samuelson and P. Antognetti, *Triggering phenomena in avalanche diodes.* IEEE Transactions on Electron Devices, 1972. **19**(9): p. 1056-1060.

25. A. Lacaita and M. Mastrapasqua, *Strong dependence of time resolution on detector diameter in single photon avalanche diodes.* Electronics Letters, 1990. **26**(24): p. 2053-2054.

26. D. O'Connor and D. Phillips, *Time-Correlated Single Photon Counting (London: Academic).* 1984.

27. W. Becker, *Advanced time-correlated single photon counting techniques*. Vol. 81. 2005: Springer Science & Business Media.

28. P. Coates, *The correction for photonpile-up'in the measurement of radiative lifetimes.* Journal of Physics E: Scientific Instruments, 1968. **1**(8): p. 878.

29. S. Pellegrini, G.S. Buller, J.M. Smith, A.M. Wallace and S. Cova, *Laser-based distance measurement using picosecond resolution time-correlated single-photon counting.* Measurement Science and Technology, 2000. **11**(6): p. 712.

30. F. Acerbi, M. Anti, A. Tosi and F. Zappa, *Design criteria for InGaAs/InP single-photon avalanche diode.* IEEE Photonics Journal, 2013. **5**(2): p. 6800209-6800209.

31. S. Forrest, O. Kim and R. Smith, *Optical response time of In0. 53Ga0. 47As/InP avalanche photodiodes.* Applied Physics Letters, 1982. **41**(1): p. 95-98.

32. F. Zappa, A. Lacaita, S. Cova and P. Webb, *Nanosecond single-photon timing with InGaAs/InP photodiodes.* Optics Letters, 1994. **19**(11): p. 846-848.

33. Y. Liu, S.R. Forrest, J. Hladky, M. Lange, G.H. Olsen, and D. Ackley, *A planar InP/InGaAs avalanche photodiode with floating guard ring and double diffused junction.* Journal of Lightwave Technology, 1992. **10**(2): p. 182-193.

34. S. Sze and G. Gibbons, *Effect of junction curvature on breakdown voltage in semiconductors.* Solid-State Electronics, 1966. **9**(9): p. 831-845.

35. M.A. Itzler, X. Jiang, M. Entwistle, K. Slomkowski, A. Tosi, F. Acerbi, F. Zappa, and S. Cova, *Advances in InGaAsP-based avalanche diode single photon detectors.* Journal of Modern Optics, 2011. **58**(3-4): p. 174-200.

36. A. Lacaita, F. Zappa, S. Cova and P. Lovati, *Single-photon detection beyond 1 μm: performance of commercially available InGaAs/InP detectors.* Applied Optics, 1996. **35**(16): p. 2986-2996.

37. A. Tosi, S. Cova, F. Zappa, M.A. Itzler and R. Ben-Michael. *InGaAs/InP single photon avalanche diode design and characterization*. in *2006 European Solid-State Device Research Conference*. 2006. IEEE.

38. M.A. Itzler, R. Ben-Michael, C.-F. Hsu, K. Slomkowski, A. Tosi, S. Cova, F. Zappa, and R. Ispasoiu, *Single photon avalanche diodes (SPADs) for 1.5 μ m*

photon counting applications. Journal of Modern Optics, 2007. **54**(2-3): p. 283-304.

39. M. Liu, C. Hu, X. Bai, X. Guo, J.C. Campbell, Z. Pan, and M.M. Tashima, *High-performance InGaAs/InP single-photon avalanche photodiode.* IEEE Journal of Selected Topics in Quantum Electronics, 2007. **13**(4): p. 887-894.

40. M.A. Itzler, X. Jiang, B. Nyman, R. Ben-Michael and K. Slomkowski. *InP-based single photon avalanche diodes*. in *LEOS 2008-21st Annual Meeting of the IEEE Lasers and Electro-Optics Society*. 2008. IEEE.

41. A. Tosi, F. Acerbi, M. Anti and F. Zappa, *InGaAs/InP single-photon avalanche diode with reduced afterpulsing and sharp timing response with 30 ps tail.* IEEE Journal of Quantum Electronics, 2012. **48**(9): p. 1227-1232.

42. A. Tosi, N. Calandri, M. Sanzaro and F. Acerbi, *Low-noise, low-jitter, high detection efficiency InGaAs/InP single-photon avalanche diode.* IEEE Journal of Selected Topics in Quantum Electronics, 2014. **20**(6): p. 192-197.

43. R.E. Warburton, M. Itzler and G.S. Buller, *Free-running, room temperature operation of an InGaAs/InP single-photon avalanche diode.* Applied Physics Letters, 2009. **94**(7): p. 071116.

44. R. Warburton, M. Itzler and G. Buller, *Improved free-running InGaAs/InP single-photon avalanche diode detectors operating at room temperature.* Electronics Letters, 2009. **45**(19): p. 996-997.

45. B. Korzh, N. Walenta, T. Lunghi, N. Gisin and H. Zbinden, *Free-running InGaAs single photon detector with 1 dark count per second at 10% efficiency.* Applied Physics Letters, 2014. **104**(8): p. 081108.

46. X. Jiang, M. Itzler, K. O'Donnell, M. Entwistle, M. Owens, K. Slomkowski, and S. Rangwala, *InP-based single-photon detectors and geiger-mode APD arrays for quantum communications applications.* IEEE Journal of Selected Topics in Quantum Electronics, 2015. **21**(3): p. 5-16.

47. N. Namekata, S. Adachi and S. Inoue, *1.5 GHz single-photon detection at telecommunication wavelengths using sinusoidally gated InGaAs/InP avalanche photodiode.* Optics Express, 2009. **17**(8): p. 6275-6282.

48. Z. Lu, W. Sun, Q. Zhou, J. Campbell, X. Jiang, and M.A. Itzler, *Improved sinusoidal gating with balanced InGaAs/InP single photon avalanche diodes.* Optics Express, 2013. **21**(14): p. 16716-16721.

49. A. Tosi, C. Scarcella, G. Boso and F. Acerbi, *Gate-free InGaAs/InP single-photon detector working at up to 100 Mcount/s.* IEEE Photonics Journal, 2013. **5**(4): p. 6801308-6801308.

50. H. Chen, M. Jiang, S. Sun, G. Tang and L. Liang, *Room temperature continuous frequency tuning InGaAs/InP single-photon detector.* AIP Advances, 2018. **8**(7): p. 075106.

51. N. Namekata, S. Sasamori and S. Inoue, *800 MHz single-photon detection at 1550-nm using an InGaAs/InP avalanche photodiode operated with a sine wave gating.* Optics Express, 2006. **14**(21): p. 10043-10049.

52. Y. Nambu, S. Takahashi, K. Yoshino, A. Tanaka, M. Fujiwara, M. Sasaki, A. Tajima, S. Yorozu, and A. Tomita, *Efficient and low-noise single-photon avalanche photodiode for 1.244-GHz clocked quantum key distribution.* Optics Express, 2011. **19**(21): p. 20531-20541.

53. A. Restelli, J.C. Bienfang and A.L. Migdall, *Single-photon detection efficiency up to 50% at 1310 nm with an InGaAs/InP avalanche diode gated at 1.25 GHz.* Applied Physics Letters, 2013. **102**(14): p. 141104.

54. M. Ghioni, A. Gulinatti, I. Rech, F. Zappa and S. Cova, *Progress in silicon single-photon avalanche diodes.* IEEE Journal of Selected Topics in Quantum Electronics, 2007. **13**(4): p. 852-862.

55. H.K. Onnes, *Investigations into the properties of substances at low temperatures, which have led, amongst other things, to the preparation of liquid helium.* Nobel Lecture, 1913. **4**.

56. G. Gol'tsman, A. Semenov, Y.P. Gousev, M. Zorin, I. Godidze, E. Gershenzon, P. Lang, W. Knott, and K. Renk, *Sensitive picosecond NbN detector for radiation from millimetre wavelengths to visible light.* Superconductor Science and Technology, 1991. **4**(9): p. 453.

57. C.M. Natarajan, M.G. Tanner and R.H. Hadfield, *Superconducting nanowire single-photon detectors: physics and applications.* Superconductor Science and Technology, 2012. **25**(6): p. 063001.

58. J.K. Yang, A.J. Kerman, E.A. Dauler, V. Anant, K.M. Rosfjord, and K.K. Berggren, *Modeling the electrical and thermal response of superconducting nanowire single-photon detectors.* IEEE Transactions on Applied Superconductivity, 2007. **17**(2): p. 581-585.

59. S. Miki, M. Fujiwara, M. Sasaki, B. Baek, A.J. Miller, R.H. Hadfield, S.W. Nam, and Z. Wang, *Large sensitive-area NbN nanowire superconducting single-photon detectors fabricated on single-crystal MgO substrates.* Applied Physics Letters, 2008. **92**(6): p. 061116.

60. H. Takesue, S.W. Nam, Q. Zhang, R.H. Hadfield, T. Honjo, K. Tamaki, and Y. Yamamoto, *Quantum key distribution over a 40-dB channel loss using superconducting single-photon detectors.* Nature Photonics, 2007. **1**(6): p. 343.

61. A. Verevkin, J. Zhang, R. Sobolewski, A. Lipatov, O. Okunev, G. Chulkova, A. Korneev, K. Smirnov, G. Gol'tsman, and A. Semenov, *Detection efficiency of large-active-area NbN single-photon superconducting detectors in the ultraviolet to near-infrared range.* Applied Physics Letters, 2002. **80**(25): p. 4687-4689.

62. A. Pearlman, A. Cross, W. Slysz, J. Zhang, A. Verevkin, M. Currie, A. Korneev, P. Kouminov, K. Smirnov, and B. Voronov, *Gigahertz counting rates of NbN single-photon detectors for quantum communications.* IEEE Transactions on Applied Superconductivity, 2005. **15**(2): p. 579-582.

63. J. Sprengers, A. Gaggero, D. Sahin, S. Jahanmirinejad, G. Frucci, F. Mattioli, R. Leoni, J. Beetz, M. Lermer, and M. Kamp, *Waveguide superconducting single-photon detectors for integrated quantum photonic circuits.* Applied Physics Letters, 2011. **99**(18): p. 181110.

64. K.M. Rosfjord, J.K. Yang, E.A. Dauler, A.J. Kerman, V. Anant, B.M. Voronov, G.N. Gol'Tsman, and K.K. Berggren, *Nanowire single-photon detector with an integrated optical cavity and anti-reflection coating.* Optics Express, 2006. **14**(2): p. 527-534.

65. S. Miki, T. Yamashita, M. Fujiwara, M. Sasaki and Z. Wang, *Multichannel SNSPD system with high detection efficiency at telecommunication wavelength.* Optics Letters, 2010. **35**(13): p. 2133-2135.

66. W. Zhang, L. You, H. Li, J. Huang, C. Lv, L. Zhang, X. Liu, J. Wu, Z. Wang, and X. Xie, *NbN superconducting nanowire single photon detector with efficiency over 90% at 1550 nm wavelength operational at compact cryocooler temperature.* Science China Physics, Mechanics & Astronomy, 2017. **60**(12): p. 120314.

67. F. Marsili, V.B. Verma, J.A. Stern, S. Harrington, A.E. Lita, T. Gerrits, I. Vayshenker, B. Baek, M.D. Shaw, R.P. Mirin, and S. Nam, *Detecting single infrared photons with 93% system efficiency.* Nature Photonics, 2013. **7**(3): p. 210.

68. V.B. Verma, B. Korzh, F. Bussieres, R.D. Horansky, A.E. Lita, F. Marsili, M. Shaw, H. Zbinden, R. Mirin, and S. Nam, *High-efficiency WSi superconducting nanowire single-photon detectors operating at 2.5 K.* Applied Physics Letters, 2014. **105**(12): p. 122601.

69. V.B. Verma, B. Korzh, F. Bussieres, R.D. Horansky, S.D. Dyer, A.E. Lita, I. Vayshenker, F. Marsili, M.D. Shaw, and H. Zbinden, *High-efficiency superconducting nanowire single-photon detectors fabricated from MoSi thin-films.* Optics Express, 2015. **23**(26): p. 33792-33801.

70. I. Esmaeil Zadeh, J.W. Los, R.B. Gourgues, V. Steinmetz, G. Bulgarini, S.M. Dobrovolskiy, V. Zwiller, and S.N. Dorenbos, *Single-photon detectors combining high efficiency, high detection rates, and ultra-high timing resolution.* Apl Photonics, 2017. **2**(11): p. 111301.

71. R.H. Hadfield, *Single-photon detectors for optical quantum information applications.* Nature Photonics, 2009. **3**(12): p. 696.

Chapter 3. Ge-on-Si single-photon avalanche diode detectors

3.1 Introduction

As mentioned in the previous Chapter, a range of modern applications such as terrain mapping [1], long-range imaging [2-4] and quantum communications [5-8] require single-photon detection in the short-wavelength infrared region. In particular, light detection and ranging (LIDAR) applications require compact single-photon detectors capable of operation at near room temperature. InGaAs/InP SPAD detectors have been developed and commercialised to satisfy at least some of the requirements of these applications. Although InGaAs/InP SPAD detectors are well established and have been used in demonstrations of single-photon LIDAR applications, the maximum count rate of these detectors has been limited by the deleterious effect of afterpulsing, which is explained in Chapters 2 and 4 in more detail. In addition, many applications, such as those using planar lightwave circuitry, require the integration of optoelectronic devices onto Si photonic platforms. Over the past several decades, Si has become a well-established material of choice for optoelectronic devices such as low-loss optical waveguides, photodiodes, and SPADs that operate at detection wavelengths up to 1 μm. Hence, integration into the existing Si photonic platform is a key requirement for developing efficient, compact and inexpensive photonic devices. For example, in linear optical quantum computing systems [9, 10], the single-photon detectors should be fully integrated onto the same chip as the low-loss waveguide circuitry to achieve high efficiency by eliminating high insertion losses, and to reduce the overall system size. Unfortunately, Si is relatively insensitive to radiation beyond 1 μm wavelength due to its bandgap of 1.12 eV at 300 K [11] and cannot be used for optical detection in the low loss fibre optical windows of 1310 nm and 1550 nm wavelengths [12]. Hence, other semiconductor materials or material combinations must be explored for developing single-photon detectors at these wavelengths.

In this Chapter, a discussion of alternative semiconductor materials for single-photon detection in the SWIR region, with a focus on Ge, will be provided along with their potential for integration onto Si platforms. A brief overview of semiconductor growth and fabrication techniques will be given. Finally, a review of the research towards developing Ge-on-Si SPAD detectors will be presented.

3.2 Material selection for the photodetectors operated in the short-wavelength infrared region

As discussed in the previous Chapter, the absorption properties of the semiconductor material used is one of the key parameters to consider in the design of a photodetector. The Beer-Lambert Law describes the absorption of light in a uniform semiconductor:

$$P(x) = P_0(1 - e^{-\alpha(\lambda)x}), \tag{3.1}$$

where $P(x)$ is the optical power at a distance x into the material, P_0 is the optical power of the incident light, and $\alpha(\lambda)$ is the absorption coefficient of the material at a wavelength λ.

The responsivity of a detector, defined as the ratio of the amount of photocurrent generated within the depletion region and the power of the incident light, is also dependent on the absorption coefficient:

$$R = \frac{q\lambda}{hc}(1 - e^{-\alpha(\lambda)x}), \tag{3.2}$$

where q is the elementary charge, h is Planck's constant, and c is the speed of light in vacuo. This expression assumes all photo-generated carriers contribute to the photocurrent. Hence, the intrinsic properties of the semiconductor such as bandgap energy, which is directly related to the cut-off wavelength ($\lambda_{cut\text{-}off} = hc/E_G$) and the absorption coefficient define the responsivity of a photodetector. Consequently, the responsivity also varies with the incident light wavelength.

Figure 3.1 illustrates the dependence of the absorption coefficient on the wavelength of incident light for different semiconductor materials. The cut-off wavelength depends on the band-gap energy of the semiconductor. If the wavelength of the incident light is greater than the cut-off wavelength, the energy of a photon is insufficient for exciting an electron into the valence band. As such, choosing an appropriate semiconductor material is crucial to optimising the performance of a photodetector aimed at a given wavelength range.

From Figure 3.1, it can be observed that $In_{0.53}Ga_{0.47}As$ and Ge are particularly suitable candidates for photon detection at wavelengths up to 1.6 μm in the SWIR region due to their high absorption coefficients at these wavelengths. However, as shown in Figure 3.2, the lattice constant of both these materials is significantly different from the Si lattice

constant. The lattice constant of Si is 0.543 nm, while the lattice constants of the Ge and $In_{0.53}Ga_{0.47}As$ are 0.565 nm and 0.587 nm, respectively [13].

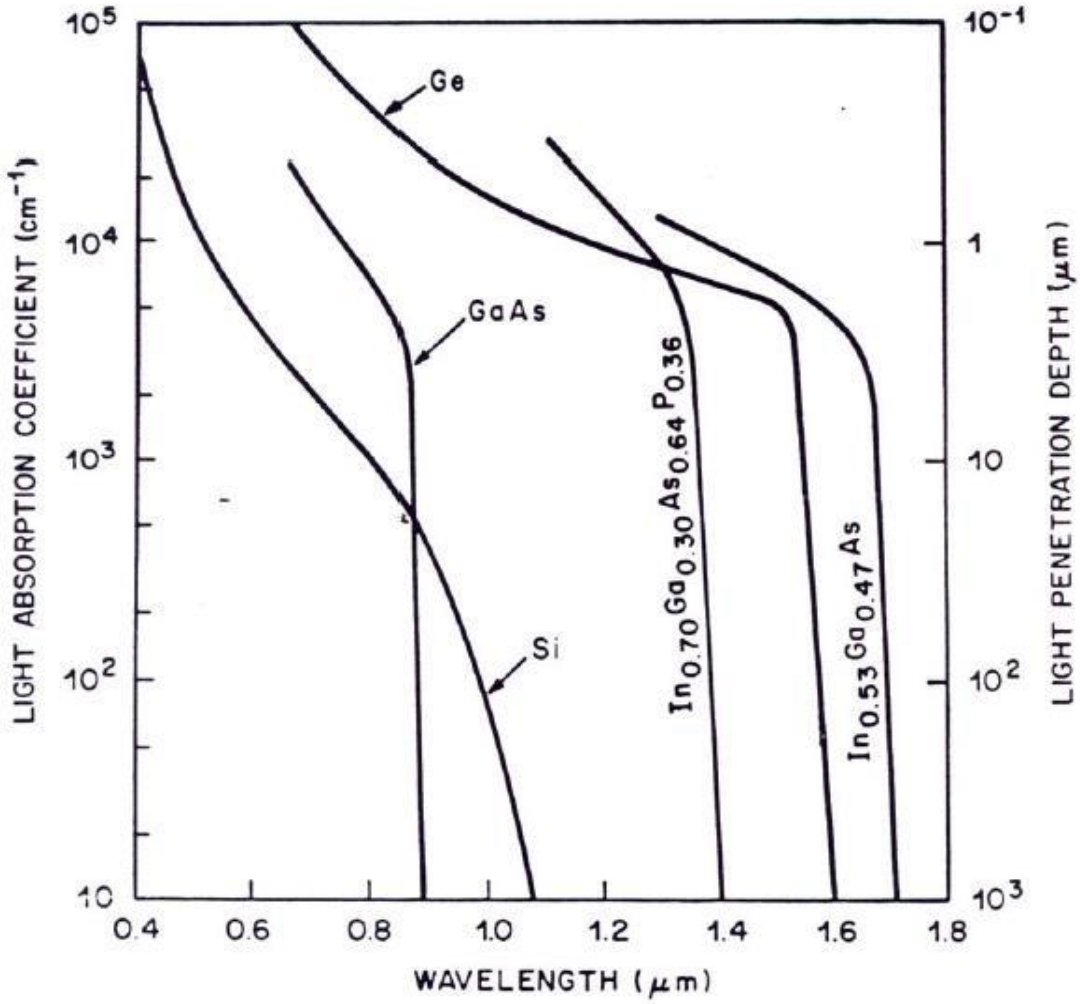

Figure 3.1. Wavelength dependence of the optical absorption coefficient for different semiconductor materials. From Ref. [12].

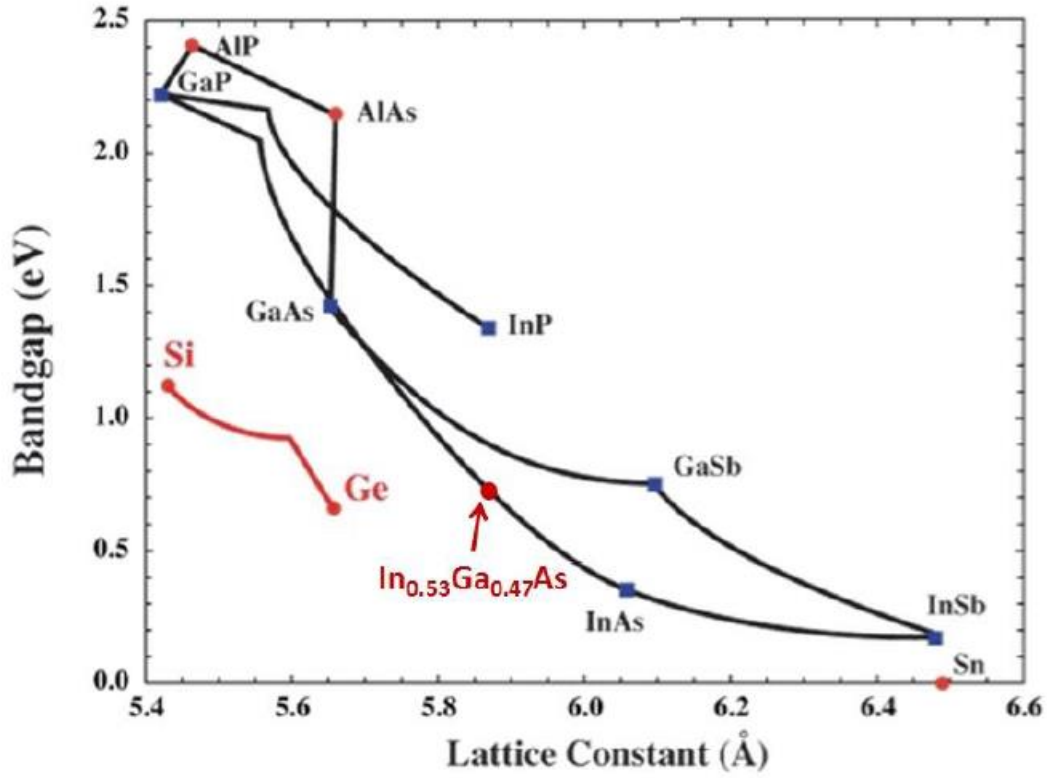

Figure 3.2. Lattice constant and band-gap energy for different semiconductors. From Ref. [13].

Because of the ~4.2 % and ~8 % lattice mismatch, Ge and $In_{0.53}Ga_{0.47}As$, photodiodes are usually fabricated using lattice-matched InP and Ge wafers, respectively. Nevertheless, due to the reasons mentioned above, research has been conducted towards the integration of InGaAs and Ge Si platforms to form photodetectors and a review of these results will be presented in the end of this Chapter.

In the past century, the electronic and optical properties of Ge have been studied in detail by many authors [11, 14-16]. The band structure of Ge at a temperature of 300 K is shown in Figure 3.3.

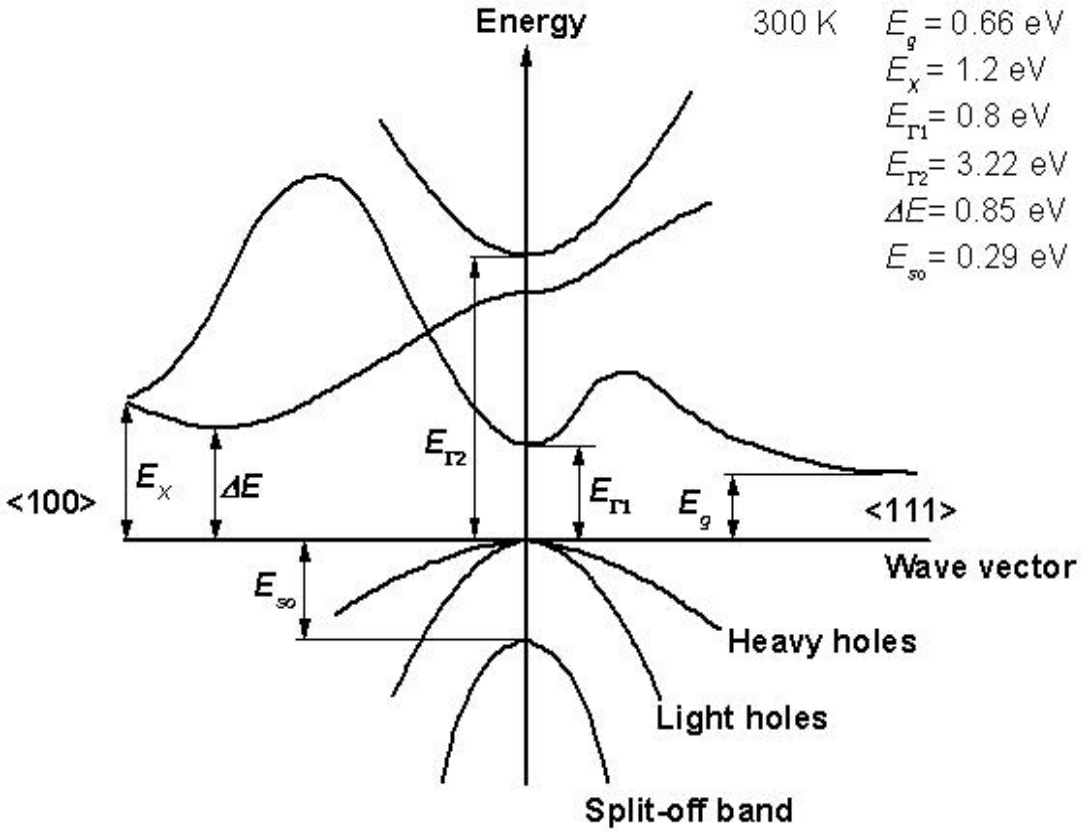

Figure 3.3. Band structure of Ge. From Ref. [11]. Although Ge has an indirect bandgap of 0.66 eV, promotion of an electron into that valley of the conduction band requires a change of momentum. Hence, a photon with the energy greater than direct band gap energy of 0.8 eV is required to promote an electron from the valance band into the conduction band.

The indirect band gap energy of Ge, E_g, is 0.66 eV. However, a direct band gap exists with an energy, $E_{\Gamma 1}$, of 0.80 eV. As a result of this direct band gap, the possibility of a direct electron transition from the valence band to the conduction band after absorption of a photon with energy equal or greater than $E_{\Gamma 1}$ is very high. This means that Ge can behave as a direct band gap semiconductor. Direct band gap materials usually exhibit high absorption properties because direct transition is a two-particle process (photon and electron-hole) while in indirect band gap semiconductors, such as Si and Ge, a third particle, a phonon, is required for electron promotion. Lattice vibrations of the material (phonons) give a change of the momentum in order to promote an electron from the valence band to the conduction band after photon absorption with required energy. Of course, such three-particle processes are less efficient compared to the direct band gap transitions. With this considered, "direct" band gap Ge can efficiently absorb light of up

to ~1.6 μm wavelength at room temperature. This explains the high absorption coefficient up to this wavelength range shown in Figure 3.1.

3.3 Growth and fabrication techniques of Ge-on-Si photodetectors

Epitaxial growth is a deposition of a crystalline overlayer on top of a crystalline substrate. There are a few main challenges in epitaxial growth of Ge on Si substrates. The 4.2% lattice mismatch leads to the high surface roughness of Ge due to Stranski–Krastanov growth, also known as 'layer-plus-island growth' [17]. Above a certain number of layers, which is determined by the critical thickness, Ge starts to grow by nucleation of Ge "islands" resulting in high surface roughness. Moreover, the lattice mismatch introduces misfit dislocations (MDs) and threading dislocations (TDs) in the epilayer. MDs occur in place of a missing or dangling bond in the lattice between two layers that have different lattice constants. For every MD, two TDs at the ends of the misfit are formed. These dislocations form a loop so that the ends of TDs are joined or thread to a surface [18]. Figure 3.4 illustrates a schematic diagram of MD and TDs (a) and a transmission electron microscopy (TEM) image of Si/SiGe heterostructure, which clearly shows a large number of MDs and TDs (b).

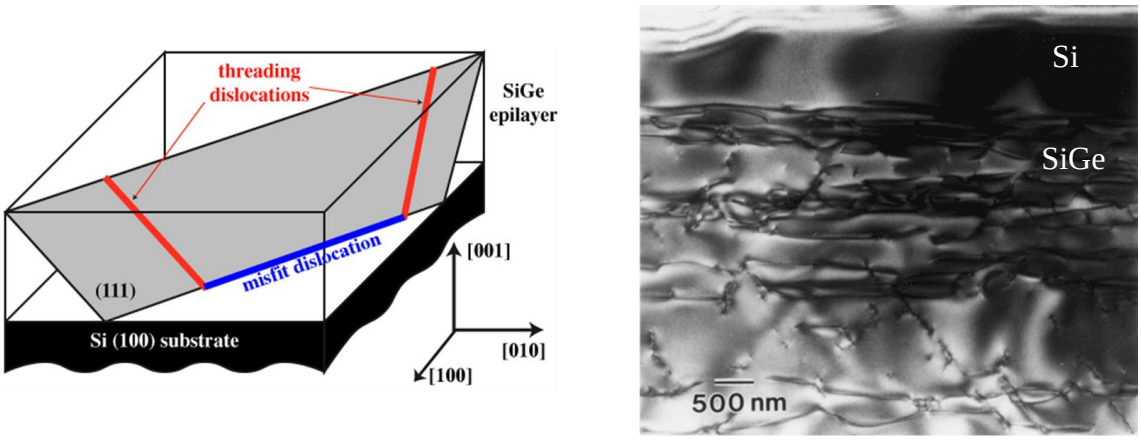

Figure 3.4. A schematic diagram of a misfit and two threading dislocations in SiGe epilayer grown on Si substrate (a). A TEM image of Si(top)/SiGe(bottom) heterosructure clearly shows a large number of dislocations (b). From Ref. [18, 19]

There are several sources of MD formation. In addition to missing and dangling bonds in the lattice at the substrate-layer interface, substrate inhomogeneities such as dust,

mechanical damage or impurities can cause the relaxation of the epilayer, which leads to formation of TDs and MDs. TDs can also transform into MDs [20]. Figure 3.5 illustrates this process. When the misfit strain force is stronger than the tension in the MD line and the tension in the surface step, TD transforms into MD.

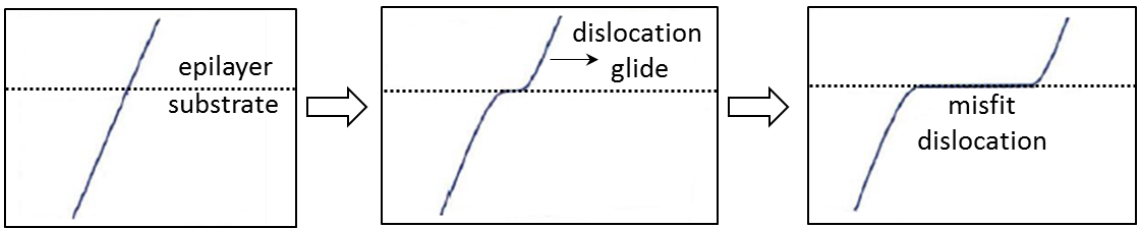

Figure 3.5. A schematic diagram of TD transformation into a MD. From Ref. [20]

Due to their nature, they are confined between the Si surface and the Ge epilayers. TDs typically form across the epilayer surface and, since devices are made near the surface, TDs cannot be avoided. Furthermore, TDs lead to a reduction of carrier mobility and lifetime [21] and compromise device reliability [22].

As discussed previously, the epitaxial growth of Ge is a challenging process. Different growth techniques have been developed to obtain pure Ge on Si with minimal dislocation densities and smooth surfaces. Among them, Molecular Beam Epitaxy (MBE) and Chemical Vapour Deposition (CVD) will be discussed as the most common techniques.

Many different materials, such as metals, semiconductors and insulator films, can be produced using MBE. A schematic of a typical MBE process is shown in Figure 3.6.

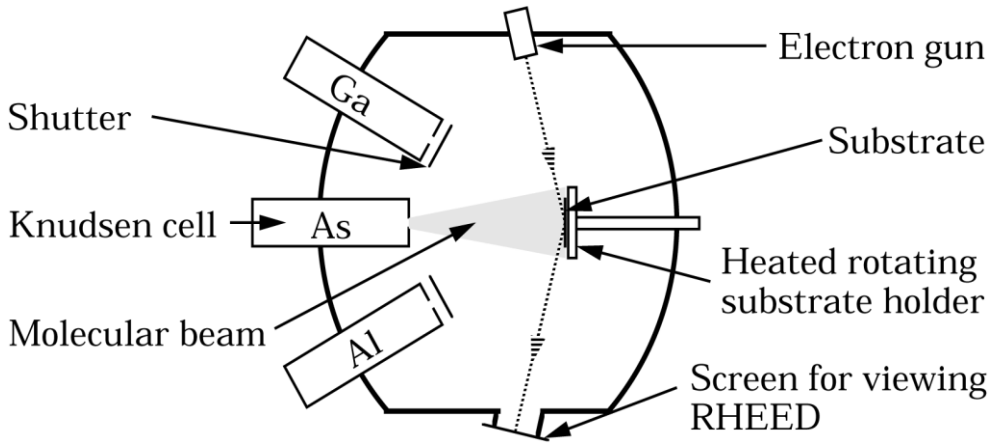

Figure 3.6. A schematic of a typical MBE growth system. From Ref. [23]. A substrate is placed on the heated rotating substrate holder. Different materials located in Knudsen cells can be deposited onto the substrate. Reflection high-energy electron diffraction is used for monitoring the growth process.

A substrate material is placed on heated rotating substrate holder. Different semiconductor materials located in Knudsen cells are heated until they sublime. The gaseous elements then form a thermal-energy molecular beam, which condenses on the substrate surface creating a crystallised film of the component elements. Furthermore, the doping level and the composition can be controlled by adjusting the evaporation rates of the respective sources [24]. Reflection high-energy electron diffraction (RHEED) is used for monitoring the growth process. MBE technique requires an ultra-high vacuum, usually of a pressure of around 10^{-10} mbar. A drawback of this technique is the possibility of contamination when different materials are deposited due to materials previously deposited on the walls of the growth chamber.

On the other hand, in chemical vapour deposition (CVD), the wafers are exposed to volatile precursor gases, which react and/or decompose on the substrate surface to produce the desired material film. One of the advantages of the CVD method is the ability to remove the undesirable, volatile by-products using the gas flow through the growth chamber. This chemical process is used to produce high quality, high-performance, solid materials with low background contamination and good uniformity [25]. Other advantages are the relatively high deposition rates and good reproducibility as CVD processes often do not require a high vacuum. On the other hand, CVD has some disadvantages as well. First, precursor gases can be very toxic and some of them are explosive or corrosive as well as expensive. Secondly, due to the nature of the reaction,

films are usually deposited under high temperature conditions. In other words, there is a restriction on the substrate material. In addition, when two materials have different thermal expansion coefficients high deposition temperatures can cause mechanical instabilities due to stresses in the deposited epilayer.

Depending on the pressure used, the CVD methods are classified:

- Reduced-pressure CVD (RP-CVD) for pressure range from 133 mbar to 1.3 mbar
- Low-Pressure CVD (LP-CVD) for pressure range from 1.3 mbar to 1.3 10^{-3} mbar
- Ultra-High Vacuum CVD (UHV-CVD) for pressure > 1.3 10^{-7} mbar

In addition to these, there are a large variety of improved CVD techniques using lasers, plasma, ions to increase deposition rates or/and decrease deposition temperature.

Over the past three decades, extensive research has been conducted towards developing the processes for heteroepitaxial growth of Ge on Si and consequently Ge-on-Si photonic devices. In this section, epitaxial growth techniques such as direct epitaxial growth using a SiGe buffer layer, epitaxial growth of pure Ge on Si, two temperature steps growth, selective epitaxial growth (SEG) and wafer bonding will be discussed.

First, Ge-on-Si heterostructures were grown using MBE and employed a SiGe buffer layer to reduce the TD density (TDD) at the SiGe/Si interface [26-30]. While this buffer helped to reduce the TDD, it had a low absorption coefficient due to the indirect bandgap of SiGe alloy. As such, this prevents the fabrication of efficient infrared photodetectors using this method.

The epitaxial growth of pure Ge on Si has been demonstrated as well [30-35]. With the aim of TDD reduction, the effects of different growth temperatures and post-growth annealing have been investigated. Direct deposition of pure Ge on Si (001) at a growth temperature of 610°C resulted in the lowest TDD of ~2×10^7 cm^{-2} as reported by *Baribeau et al.* in 1989 [35]. The authors also demonstrated almost an order of magnitude reduction in TDD after 30 minutes annealing at 700°C, thus verifying that annealing improves the crystalline quality of Ge epilayer as was previously reported by *Fukuda et al.* [33]. In 1992, *Malta et al.* demonstrated improved results with a TDD of 10^5 cm^{-2}. The authors reported on a method in which Ge growth is initiated at a temperature of 500°C and then raised to 900°C. However, 900°C is close to the melting point of Ge (937°C). As a result, they observed the formation of a SiGe alloy at the interface. An

epitaxial growth at a temperature of 370°C has been demonstrated by *Liu et al.* [32] with the aim of the tensile strain reduction due to the thermal mismatch between Ge and Si. However, the authors reported a TDD of ~4×10^{10} cm^{-2}.

A two-temperature step growth using UHV-CVD has been demonstrated by *Colace et al.* [36, 37] in 1998. First, a substrate was thoroughly cleaned and a thin buffer layer of pure Ge of ~50 nm – 100 nm was grown at a temperature of ~300°C - 400°C to prevent the strain release through island growth. Following this step, the temperature was increased to up to ~500°C - 700°C and a thick layer of Ge was subsequently grown. The authors reported a density of recombination centres of ~10^{14} cm^{-3}, which suggests a high TDD. An improved process was later reported by *Luan et al.* [38]. The authors added a cyclic thermal annealing step, where a wafer is annealed between a high annealing temperature and a low annealing temperature after the material growth.

Another alternative growth method, selective epitaxial growth (SEG), has been developed to decrease the TDD. In this method, a SiO_2 or Si_3N_4 patterned mask is employed to allow epitaxial growth of Ge only in small confined areas. The first example of SEG of Ge on Si was presented by Luan et al. in 1999 [39]. This method, combined with the previously described two-temperature steps growth method and cyclic thermal annealing, allowed for a significant reduction of TDD. The threading arms of the MDs that originate at the heterointerface during SEG propagate at a 45° angle from the substrate and terminate at the oxide sidewalls [40]. Figure 3.7 illustrates this process, which is called epitaxial necking.

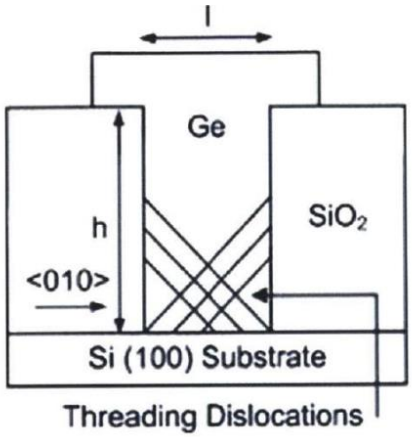

Figure 3.7. A schematic diagram of epitaxial necking. This cross-section demonstrates that threading dislocations propagate at a 45° angle and terminate at the sidewalls. From Ref. [40].

In 2007, a defect-free SEG was demonstrated by *Park et al*. [41]. The authors investigated SEG of Ge with a maximum thickness of up to 450 nm for different height/width ratio of SiO_2 trenches that were used for epitaxial necking. Later, in 2010, *Wang et al.* demonstrated similar results [42]. However, the authors found that combining SEG with two temperature steps method and performing cyclic thermal annealing proved more effective for TDD reduction. The SEG technique allows the selective introduction Ge detectors onto the complementary metal-oxide-semiconductor (CMOS) Si technology commonly used for manufacturing Si photonics components.

Finally, use of the low temperature wafer bonding technique for fabricating Ge-on-Si photodiodes has been reported by *Kanbe et al.* in 2008 and *Gity et al*. in 2013 [43, 44]. The wafer bonding process starts by cleaning the substrates in order to remove any organic compounds and metals. A dilute HF solution was then used to remove native oxides. Then, the Si and Ge wafers were dipped into H_2SO_4:H_2O_2:H_2O and HCl:H_2O solutions, respectively, to make the surfaces hydrophilic. After cleaning, the wafers are brought into contact. The Van der Waals forces that are formed upon surface-to-surface contact initially bind the samples. Finally, the wafers were annealed to create strong covalent bonds between the two samples. Originally, this technique has been developed for integration of InGaAs, which has a greater lattice mismatch of 8% onto Si. (InGaAs-on-Si photodetectors will be discussed at the end of this Chapter.) *Gity et al.* have demonstrated the fabrication of mesa p-n photodiodes of different diameters from 20 μm to 500 μm. The authors reported a responsivity of 1.6 A/W at 1550 nm wavelength for a 500 μm device and a lower responsivity of 0.3 A/W for a 30 μm diameter device. The traps at the heterointerface limited the performance of these photodiodes. Epitaxial growth of Ge on Si demonstrates superior results in terms of defect density, therefore, the amount of literature on wafer bonded Ge-on-Si photodiodes is limited.

All the planar Ge-on-Si SPAD detectors that will be discussed in Chapters 4, 5 and 6 were epitaxially grown by the commercial company IQE using RP-CVD system.

3.4 Separate absorption charge multiplication structure of APDs and SPADs

As discussed previously, the development of suitable growth techniques allowed the realisation of Ge-on-Si heteroepitaxial structures. During the past decade, research has been conducted towards the fabrication of high-speed and high efficiency APDs and SPAD detectors. Compared to p-i-n photodiodes, APDs have the potential to detect weak

optical signals. Higher internal gain, high sensitivity and high speed in APDs are achieved by applying a large external bias to create high electric fields within the photodiode. However, these high electric fields can cause issues with tunnelling assisted traps and surface states which are much less apparent in the lower field p-i-n structures. For optimal performance, the electric field must be carefully controlled for different semiconductor materials within a heterostructure due to the difference in each of their internal properties. The separate absorption charge multiplication (SACM) avalanche photodiode structure [45] is such an example. In the multiplication region of an APD, a high electric field is required to accelerate the carriers to cause impact ionisation. On the other hand, materials that are sensitive to long-wavelength light have a small band gap and, consequently, the high electric fields necessary to instigate impact ionisation can lead to inter-band tunnelling, resulting in an undesirable source of dark current. The SACM design addresses this issue by separating absorption and multiplication layers. A charge layer, which is designed to keep the electrostatic potential across the absorption material low, is situated between the absorption and multiplication layers, such that only the wide-gap multiplication layer experiences the high electric fields necessary for impact ionisation. The low-bandgap material, necessary for long-wavelength light absorption, is a separate adjacent layer. A small electric field, however, is maintained in the absorption layer to ensure successful carrier transport to the multiplication region. By designing the structure correctly, it is also possible to ensure that the primary carriers drifting to the multiplication region are predominantly the species (either electron or hole) that have the highest impact ionisation coefficients. By doing this, we have the lowest excess noise factor possible with the APD. Overall, the SACM approach has led to the fabrication of low dark current APDs, with high gain-bandwidth performance. So much so, that the InGaAs/InP SACM APD is a standard detector in long-haul optical telecommunications. A brief review of the SACM Ge-on-Si APDs will be presented in the next section.

3.4.1 Ge-on-Si APDs

The first demonstration of an SACM Ge-on-Si APD was reported by *Kang et al.* in 2008 [45], and its structure is shown schematically in Figure 3.8.

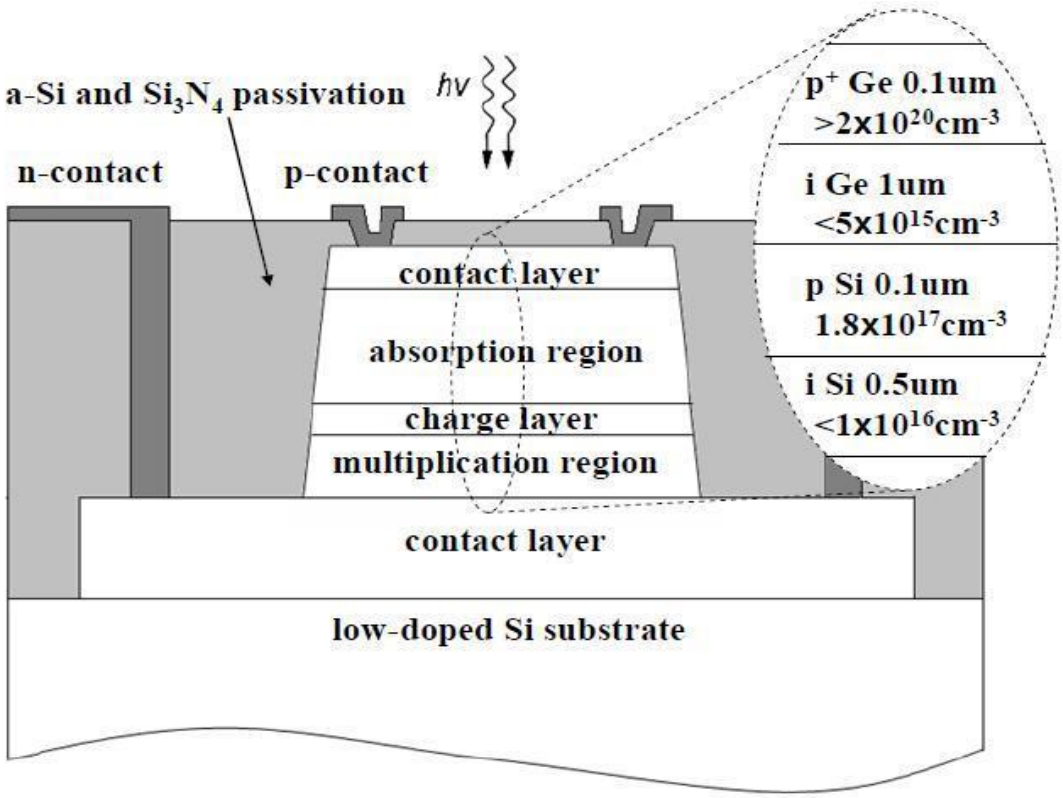

Figure 3.8. A schematic SACM structure for the Ge-on-Si APD proposed by Kang et al. [45].

In this work, the semiconductor structures were grown using a CVD reactor. The devices were fabricated as circular mesas of diameters between 10 μm and 200 μm. The sidewalls were passivated with silicon nitride and amorphous silicon (a-Si). The punch-through voltage, V_{PT}, when the depletion region extends into the Ge absorption layer, occurred between -12 V and -20 V. The avalanche breakdown voltage, V_{BD}, defined at a dark current at a level of 10 μA was measured as -25.8 V. Furthermore, a dark current density (DCD) of 237 mA/cm^2 was measured at 90% of V_{BD} and the responsivity at the gain equal to 1 was 0.54 A/W at a detection wavelength of 1310 nm.

Later, in 2009, the same research group reported a double mesa SACM APD structure fabricated using different processing approach [46]. Figure 3.9 illustrates a schematic and an SEM cross-section of a fabricated double mesa SACM structure APD.

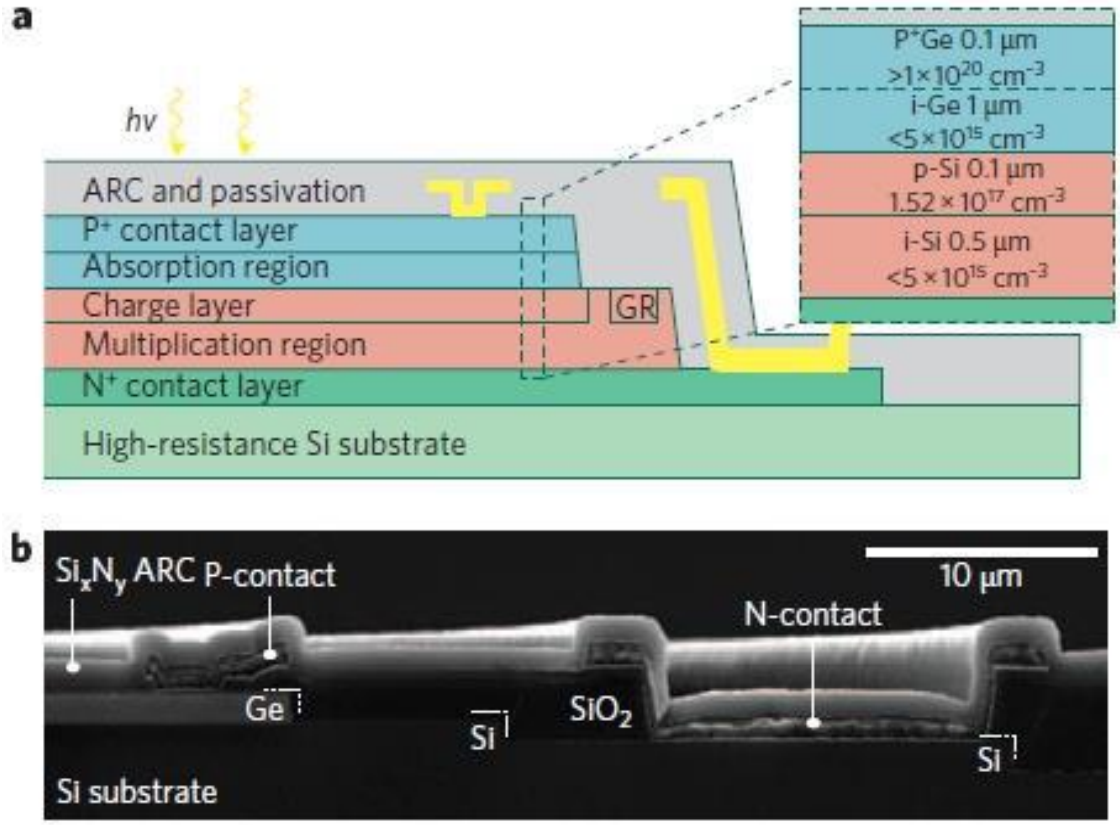

Figure 3.9. A schematic (a) and an SEM image of a double mesa Ge-on-Si SACM APD cross-section (b). From Ref. [46].

As a first improvement, they added a floating guard ring (GR), to prevent premature breakdown along the device perimeter. The distance between the guard ring and the mesa edge was varied from 1 µm to 3 µm. The resulting measurements of V_{PT} and V_{BD} were -22 V and -25 V, respectively. In addition, a DCD of 175 mA/cm2 at 90% of V_{BD} and a primary responsivity of 5.88 A/W at 1310 nm wavelength were obtained. Finally, a gain-bandwidth product of 340 GHz was observed, which is almost three times greater than found previously in to InGaAs/InP APDs [47]. From here, the development of Ge-on-Si APDs continued [48-50], including the demonstration of CMOS compatible Ge-on-Si APD arrays [51] and first Ge-on-Si SPADs. In the next section, a detailed review of the Ge-on-Si SPAD detectors reported in the literature is given. For completion, a brief overview of another integrating approach such as waveguide Ge-on-Si structures will be presented in the end of this Chapter.

3.4.2 Ge-on-Si SPADs

In 2011, *Lu et al.* reported the first Geiger mode operation of Ge-on-Si APDs [52]. These devices were epitaxially grown on (100) Si substrates by CVD. The device structure is

shown in Figure 3.10. It consisted of a 100 nm p^+-doped Ge contact layer, a 1 μm thick intrinsic Ge absorption layer, a 100 nm thick p-doped Si charge layer and a 500 nm intrinsic Si multiplication layer.

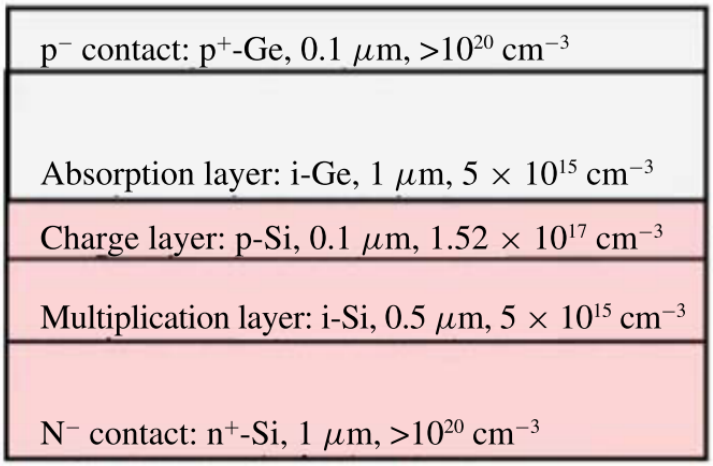

Figure 3.10 A schematic structure of the normal incidence Ge-on-Si SPAD reported in Ref. [52].

The diameter of the device active area was 30 μm. A pulsed laser diode source at 1310 nm wavelength and 100 kHz repetition rate was used to characterise the SPADs. The SPDE measurements were performed at a level of 1 photon per pulse. The authors reported a DCR of ~100 M counts/s, FWHM timing jitter of 195 ps and SPDE of up to 14% at a temperature of 200 K, which corresponds to an NEP of 1.5 10^{-14} $WHZ^{-1/2}$.

Later in 2013, Warburton et al. reported the fabrication and characterisation of normal incidence mesa Ge-on-Si SPAD detectors. The device diameters investigated varied between 25 μm and 500 μm. The detector structure was grown on highly doped n^{++} Si substrates by RP-CVD. As illustrated in Figure 3.11, the structure consisted of a 100 nm p^+-doped Ge top contact layer, a 1 μm thick intrinsic Ge absorption layer, a 100 nm thick p-doped Si charge layer and a 1 μm thick intrinsic Si multiplication layer. Two pulsed picosecond laser diode sources of 1310 nm and 1550 nm wavelengths were used to characterise these detectors. The laser repetition rate was varied between 1 kHz and 1 MHz. The SPDE, DCR, timing jitter and NEP were determined using the TCSPC technique, as discussed in Chapter 2. The authors reported an SPDE of 4% at a detection wavelength of 1310 nm, DCRs of between 1 M counts/s and 10 M counts/s and a timing jitter of 300 ps at 100 K operating temperature and 10% excess bias. Consequently, a NEP of 1×10^{-14} $WHz^{-1/2}$ was reported. In addition, the authors reported an SPDE of

0.15% and a jitter of 420 ps using a 1550 nm detection wavelength when operated at 6% excess bias and a temperature of 125 K. This resulted in a NEP of 5×10^{-12} $WHz^{-1/2}$.

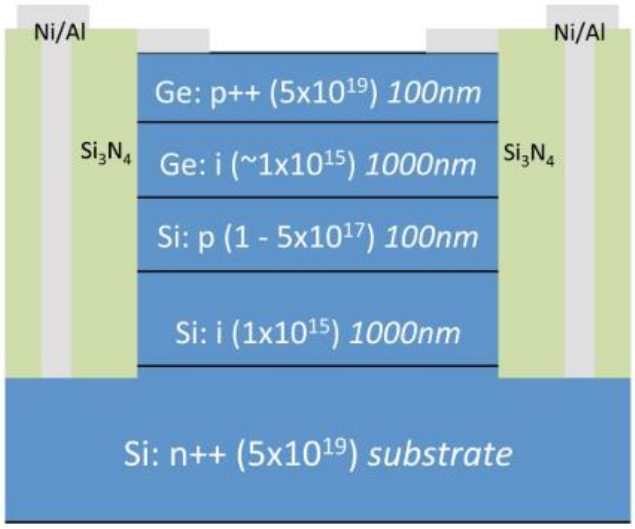

Figure 3.11. A cross-section of the normal incident Ge-on-Si mesa SPAD reported in Ref. [53].

The NEP at 1310 nm wavelength reported by *Warburton et al.* remained the lowest reported for Ge-on-Si SPADs until the planar Ge-on-Si SPAD detectors presented in this thesis were developed.

3.5 Waveguide integrated Ge-on-Si photodetectors

Waveguide structure designs have several advantages over the mesa ones. First, they can allow the optical absorption length and the carrier transit time to be de-coupled. This can be an important factor in the design of detectors for high data rate applications. Further to this, these designs enable the integration of APDs with other planar lightwave optical components such as viable wavelength demultiplexers and monolithic attenuators.

The first waveguide integrated Ge-on-Si photodetectors were presented by *Zhu et al.* in 2009 [54]. As illustrated in Figure 3.12, the authors developed a separate vertical selectively epitaxial growth (SEG) Ge absorption region, lateral Si charge and multiplication structure [54].

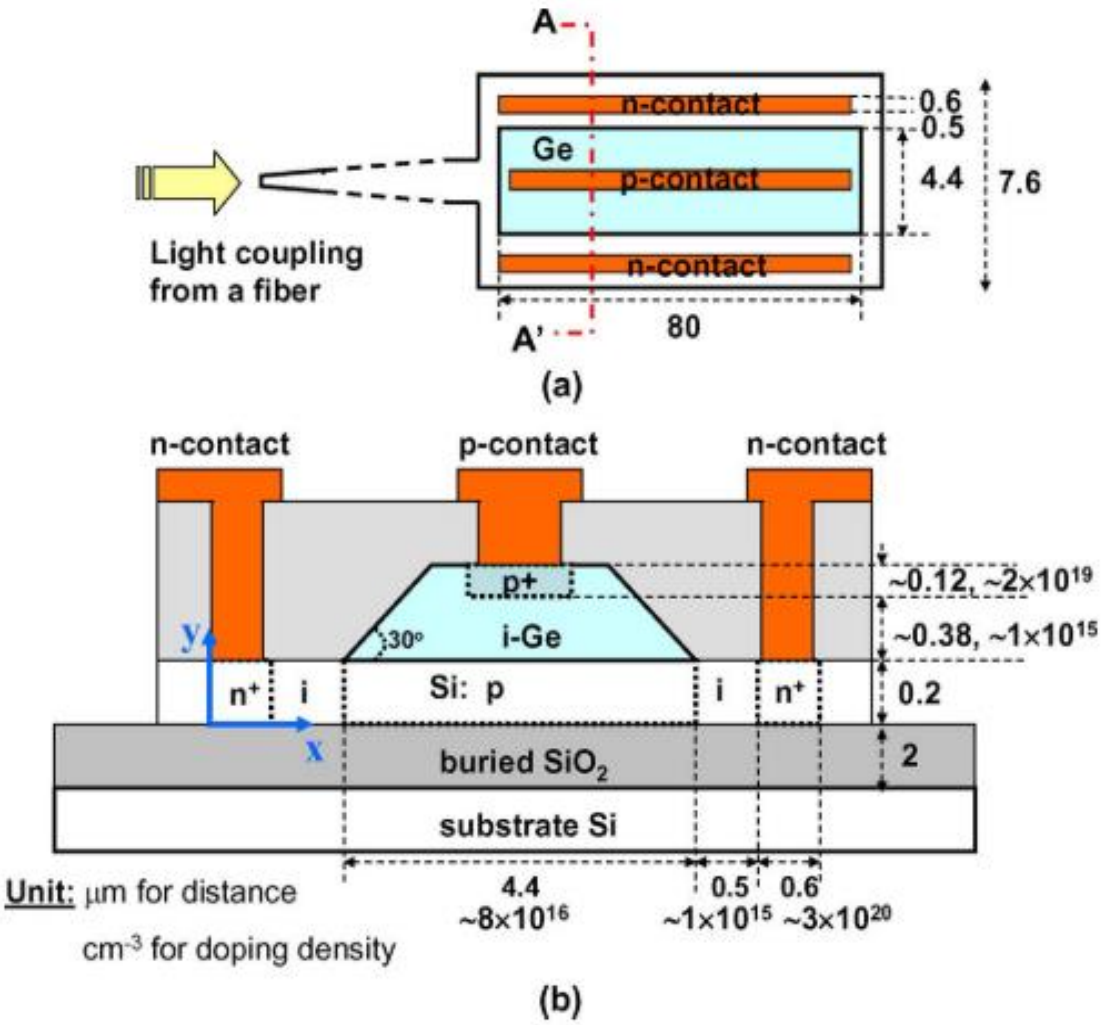

Figure 3.12. A schematic structure of a top view (a) and a cross section (b) of the waveguided Ge/Si APD. From Ref. [54].

The waveguide structures were grown on silicon-on-insulator (SOI) substrates, which had ~200 nm thick p-type top Si layers and ~2 μm buried oxides, using UHV-CVD. First, after the channel waveguide and detector region were defined, an n-contact region and the charge region were implanted with arsenic (As) and boron (B), respectively, and annealed at 1000 C for 60 s using rapid thermal annealing (RTA). Secondly, after wet cleaning, a ~500 nm thick high-quality Ge layer with a thin Si/SiGe buffer layer were selectively grown on the charge Si region. The p-contact of the top Ge layer was implanted with boron and annealed at 500 C for 5 minutes to activate the dopants. After the metal contact deposition and dicing, the samples were polished at the sidewall for light coupling from a lensed fibre into an inverted taped waveguide. These detectors demonstrated a low dark current of ~22 μA at a reverse bias of 22 V and a responsivity

of ~7.2 A/W at a detection wavelength of 1550 nm, which is greater than the responsivity reported for the normal incident APDs.

Later in 2009, *Kang et al.* also reported a waveguide-type Ge/Si APD [55]. Figure 3.13 illustrates the structure of these waveguide APDs, which was similar to the one shown in Figure 3.10 except for a thinner Ge absorption layer of ~0.6 μm thickness and a lower doping concentration in the Si charge layer. These photodetectors were fabricated on an SOI wafer and were 40 μm to 100 μm long with a 3 μm to 7 μm wide junction area. These detectors were integrated with a 6 μm wide and 2 mm long multimode Si rib waveguide, as shown in Figure 3.13. In these detectors, light is evanescently coupled up to the Ge absorption region after propagating through the passive Si waveguide. The authors reported internal responsivities of 0.9 A/W and 0.6 A/W at 10 V reverse bias at detection wavelengths of 1310 nm and 1550 nm, respectively.

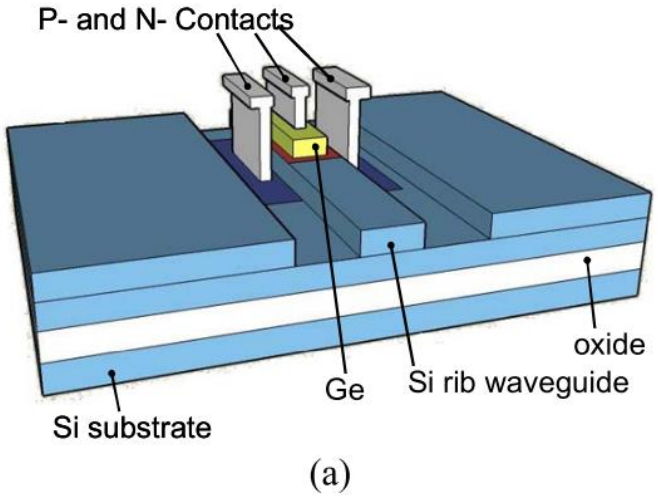

Figure 3.13. A schematic structure of a waveguide-type Ge/Si. From Ref. [55].

Detectors of similar structure have also been reported: a responsivity of ~0.8 A/W at a detection wavelength of 1550 nm was shown by *Ang et al.* in 2010 [56]; and in 2011 *DeRose et al.* presented 0.8A/W responsivity at 1530 nm wavelength [57]. Development of waveguide integrated devices continued and a significantly improved responsivity of 22 A/W at 1550 nm was reported by *Duan et al.* in 2013 [58]. Later, in 2016, Martinez et al. reported high performance Ge-on-Si APDs operated at room temperature with a responsivity of 54.5 A/W and gain-bandwidth product of 432 GHz [59] at a detection wavelength of 1510 nm, which is 3.5 times greater compared to InGaAs/InP [47]. Later, in 2017, the same research group demonstrated Geiger mode operation of waveguide-

coupled Ge-on-Si lateral APDs at a temperature of 80 K for the first time [60]. Figure 3.14 illustrates a schematic cross-section of the detector and an SEM image of the device showing a waveguide in (a) and (b), respectively.

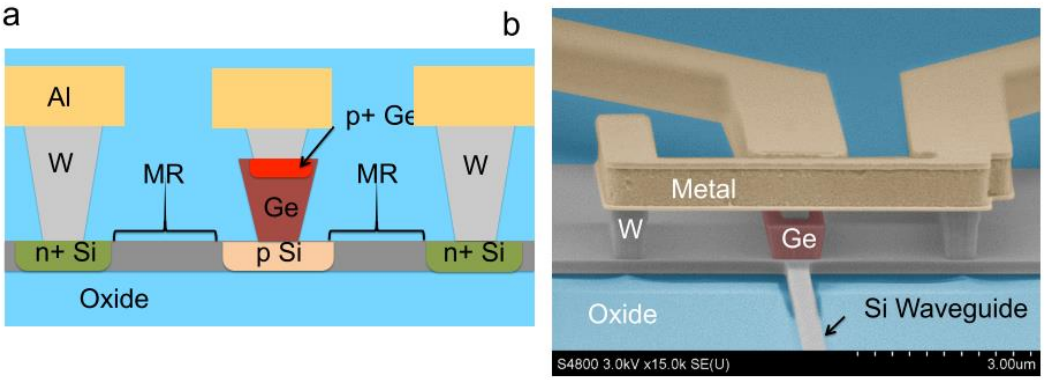

Figure 3.14. A schematic diagram of the cross-section for the lateral APD (a) and an angled SEM image of the APD with oxide cladding removed (b). The input waveguide is shown. From Ref. [60].

These detectors were fabricated using selective epitaxial growth. The SACM structures were grown on the SOI substrate. First, a 1.5 µm wide Si charge layer was implanted with boron difluoride (BF_2). Then, a 1 µm wide Ge absorption region was grown and implanted with BF_2 to create a p^+-doped top contact. The APDs had two symmetric multiplication regions (MRs) of 1.2 µm widths. As the authors noted, the p-doped charge layer has to extend beyond the footprint of the SEG Ge to prevent the penetration of the high electric field into Ge absorption region as was observed in their previous work [59]. A layer of Ti/TiN metal was used to create an ohmic contact to Ge prior to the deposition of Al metal contacts. For the Si contacts, heavily n^+ doped regions were formed prior to the Ge growth. Figure 3.14 (b) illustrates an angled SEM image of the detectors. The detector length varied from 8 µm to 32 µm with the 15.9 µm long detectors showing the lowest dark currents among the tested devices while maintaining high responsivities. The authors reported an SPDE of 5.27% at a detection wavelength of 1310 nm, a DCR of 534 k count/s and a jitter of 105 ps at an operating temperature of 80 K. These results correspond to an NEP of 2.9 10^{-15} $WHz^{-1/2}$.

3.6 Integration of InGaAs/InP detectors on Si

The integration of InGaAs/InP photodetectors into Si platforms was reported by *Kang et al.* [61-63]. Although these materials have 8% lattice mismatch and the epitaxial growth is impossible, direct wafer bonding (i.e. wafer fusion) processes were developed. As

illustrated in Figure 3.15, photons were absorbed in the InGaAs layer, while the Si layer was used for carrier multiplication.

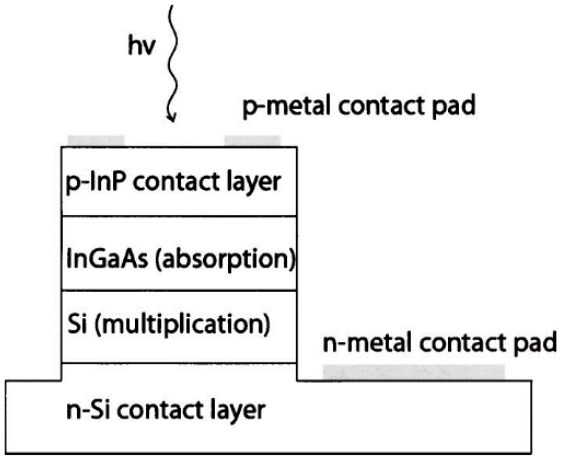

Figure 3.15. A schematic diagram of an InGaAs-on-Si APD. From Ref. [62].

The wafer bonding process starts by cleaning the substrates in order to remove any organic compounds and metals. A dilute HF solution is then used to remove native oxides and to activate the surfaces. After cleaning, the wafers were brought into contact. The Van der Waals forces that are formed upon contact hold the samples together. Finally, the wafers were baked at 650°C for 30 minutes to create strong covalent forces.

Single-photon detection using InGaAs-on-Si APDs was demonstrated by Kang et al. [62]. The authors connected a 150 μm diameter detector on the wafer by means of high-frequency probes and operated in Geiger mode. In doing so, they obtained SPDEs in the range of 2.5% to 33% at a wavelength of 1550 nm, a 100 kHz repetition rate and at a temperature of 223 K. Although obtaining promising results, the fabrication and operation of these devices remains a great challenge due to factors such as lattice mismatch and different temperature expansion coefficients.

3.7 Summary

In this Chapter, the importance of the detector integration on the Si photonics platforms has been discussed. Since Si is only sensitive to wavelengths below 1 μm wavelength, in order to detect longer wavelengths, other semiconductor materials must be considered as a part of the optical detector structure. Candidate materials for photon detection of wavelengths up to 1.6 μm have been discussed along with the main challenges of integration of these materials onto Si. Both Ge and InGaAs are lattice mismatched to Si,

8% and 4%, respectively. Overcoming the issues introduced by this lattice mismatch have been the focus of several decades of research. The band structure and intrinsic properties of Ge, which is a promising candidate for single-photon detection in SWIR, have been discussed.

An overview of the epitaxial growth techniques has been presented. MBE and CVD techniques that have been developed to enable growth of lattice mismatched Ge and InGaAs on Si substrates such as wafer bonding, SEG, two temperature steps growth, cyclic thermal annealing, and introducing a SiGe buffer layer during direct epitaxial growth have been discussed in detail. Although SiGe buffer layer solves the problem of lattice mismatch between Si and Ge it has a low absorption coefficient at telecommunication wavelength and significantly reduces the responsivity of the photodetectors. SEG combined with cyclic thermal annealing demonstrated the lowest TDDs. In addition, SEG allows for integrating Ge detectors using CMOS processes along with other photonics components.

A literature review of the Ge-on-Si and InGaAs-on-Si integrated photodetectors have been presented with a focus on Ge-on-Si photodetectors. InGaAs-on-Si photodetectors have proven difficult to fabricate. Heteroepitaxy is more challenging for InGaAs due to the 8% lattice mismatch compared to Ge. Wafer bonding technique has also been used for fabricating InGaAs-on-Si photodetectors. However, SPAD fabrication using this technology remains a great challenge due to the lattice mismatch and the difference in temperature expansion coefficients.

SACM and waveguided structures have been discussed in detail. A detailed review of Ge-on-Si SPAD detectors and a Ge-on-Si waveguide integrated single-photon detector has been presented with SPDEs of up to 5.27% at 1310 nm wavelength and at a temperature of 80 K – 100 K, the lowest DCR of 534 k counts/s and the lowest timing jitter of 105 ps.

3.8 References

1. B. Schwarz, *LIDAR: Mapping the world in 3D.* Nature Photonics, 2010. **4**(7): p. 429.

2. R. Tobin, A. Halimi, A. McCarthy, X. Ren, K.J. McEwan, S. McLaughlin, and G.S. Buller, *Long-range depth profiling of camouflaged targets using single-photon detection.* Optical Engineering, 2017. **57**(3): p. 031303.

3. A.M. Pawlikowska, A. Halimi, R.A. Lamb and G.S. Buller, *Single-photon three-dimensional imaging at up to 10 kilometers range.* Optics Express, 2017. **25**(10): p. 11919-11931.

4. A. McCarthy, X. Ren, A. Della Frera, N.R. Gemmell, N.J. Krichel, C. Scarcella, A. Ruggeri, A. Tosi, and G.S. Buller, *Kilometer-range depth imaging at 1550 nm wavelength using an InGaAs/InP single-photon avalanche diode detector.* Optics Express, 2013. **21**(19): p. 22098-22113.

5. R.H. Hadfield, *Single-photon detectors for optical quantum information applications.* Nature Photonics, 2009. **3**(12): p. 696.

6. A. Boaron, B. Korzh, R. Houlmann, G. Boso, D. Rusca, S. Gray, M.-J. Li, D. Nolan, A. Martin, and H. Zbinden, *Simple 2.5 GHz time-bin quantum key distribution.* Applied Physics Letters, 2018. **112**(17): p. 171108.

7. P.J. Clarke, R.J. Collins, P.A. Hiskett, M.-J. García-Martínez, N.J. Krichel, A. McCarthy, M.G. Tanner, J.A. O'Connor, C.M. Natarajan, S. Miki, M. Sasaki, Z. Wang, M. Fujiwara, I. Rech, M. Ghioni, A. Gulinatti, R.H. Hadfield, P.D. Townsend, and G.S. Buller, *Analysis of detector performance in a gigahertz clock rate quantum key distribution system.* New Journal of Physics, 2011. **13**(7): p. 075008.

8. P.J. Clarke, R.J. Collins, V. Dunjko, E. Andersson, J. Jeffers, and G.S. Buller, *Experimental demonstration of quantum digital signatures using phase-encoded coherent states of light.* Nature Communications, 2012. **3**: p. 1174.

9. J.L. O'brien, *Optical quantum computing.* Science, 2007. **318**(5856): p. 1567-1570.

10. M.G. Thompson, A. Politi, J.C. Matthews and J.L. O'Brien, *Integrated waveguide circuits for optical quantum computing.* IET Circuits, Devices & Systems, 2011. **5**(2): p. 94-102.

11. A. Dargys and J. Kundrotas, *Handbook on physical properties of Ge, Si, GaAs and InP*. 1994: Science and Encyclopedia Publ.

12. K. Gerd, *Optical Fiber Communications*. 2 ed. 1991, New-York: McGraw-Hill.

13. S. Ghandhi, *VLSI Fabrication Principles: Silicon and Gallium Arsenide. 1994*. New York: John Wiley & Sons, Inc.

14. E.M. Conwell, *Properties of silicon and germanium.* Proceedings of the IRE, 1952. **40**(11): p. 1327-1337.

15. E. Conwell, *Properties of silicon and germanium: II.* Proceedings of the IRE, 1958. **46**(6): p. 1281-1300.

16. J.R. Chelikowsky and M.L. Cohen, *Nonlocal pseudopotential calculations for the electronic structure of eleven diamond and zinc-blende semiconductors.* Physical Review B, 1976. **14**(2): p. 556-582.

17. I.N. Stranski and L. Krastanow, *Zur Theorie der orientierten Ausscheidung von Ionenkristallen aufeinander.* Monatshefte für Chemie und verwandte Teile anderer Wissenschaften, 1937. **71**(1): p. 351-364.

18. D.J. Paul, *Si/SiGe heterostructures: from material and physics to devices and circuits.* Semiconductor Science and Technology, 2004. **19**(10): p. R75.

19. E. Kasper and D. Paul, *Material Science.* Silicon Quantum Integrated Circuits: Silicon-Germanium Heterostructure Devices: Basics and Realisations, 2005: p. 13-47.

20. J.W. Matthews, S. Mader and T.B. Light, *Accommodation of Misfit Across the Interface Between Crystals of Semiconducting Elements or Compounds.* Journal of Applied Physics, 1970. **41**(9): p. 3800-3804.

21. D.L. Dexter and F. Seitz, *Effects of Dislocations on Mobilities in Semiconductors.* Physical Review, 1952. **86**(6): p. 964-965.

22. L. Colace, P. Ferrara, G. Assanto, D. Fulgoni and L. Nash, *Low Dark-Current Germanium-on-Silicon Near-Infrared Detectors.* IEEE Photonics Technology Letters, 2007. **19**(22): p. 1813-1815.

23. J.H. Davies, *The physics of low-dimensional semiconductors: an introduction*. 1998: Cambridge University Press.

24. A. Rajan, R.T. Moug and K.A. Prior, *Epitaxial growth of zinc blende MgS directly on GaAs (0 0 1) substrates.* Semiconductor Science and Technology, 2014. **29**(2): p. 025006.

25. J. Park and T. Sudarshan, *Chemical vapor deposition: ASM International.* Metals Park, OH, 2001.

26. S. Luryi, A. Kastalsky and J.C. Bean, *New infrared detector on a silicon chip.* IEEE Transactions on Electron Devices, 1984. **31**(9): p. 1135-1139.

27. H. Temkin, J. Bean, T. Pearsall, N. Olsson and D. Lang, *High photoconductive gain in Ge x Si1− x/Si strained-layer superlattice detectors operating at λ= 1.3 μm.* Applied Physics Letters, 1986. **49**(3): p. 155-157.

28. F. Huang, X. Zhu, M. Tanner and K. Wang, *Normal-incidence strained-layer superlattice Ge0. 5Si0. 5/Si photodiodes near 1.3 μm.* Applied Physics Letters, 1995. **67**(4): p. 566-568.

29. A. Splett, T. Zinke, K. Petermann, E. Kasper, H. Kibbel, H.-J. Herzog, and H. Presting, *Integration of waveguides and photodetectors in SiGe for 1.3 μm operation.* IEEE Photonics Technology Letters, 1994. **6**(1): p. 59-61.

30. J. Baribeau, T. Jackman, D. Houghton, P. Maigne and M. Denhoff, *Growth and characterization of Si1− x Ge x and Ge epilayers on (100) Si.* Journal of Applied Physics, 1988. **63**(12): p. 5738-5746.

31. D. Malta, J. Posthill, R. Markunas and T. Humphreys, *Low-defect-density germanium on silicon obtained by a novel growth phenomenon.* Applied Physics Letters, 1992. **60**(7): p. 844-846.

32. J. Liu, H. Kim, O. Hul'Ko, Y. Xie, S. Sahni, P. Bandaru, and E. Yablonovitch, *Ge films grown on Si substrates by molecular-beam epitaxy below 450 C.* Journal of Applied Physics, 2004. **96**(1): p. 916-918.

33. Y. Fukuda and Y. Kohama, *Effect of in situ thermal annealing on crystalline quality of Ge layers grown by molecular beam epitaxy on Si (100).* Japanese Journal of Applied Physics, 1987. **26**(5A): p. L597.

34. Y. Fukuda, Y. Kohama, M. Seki and Y. Ohmachi, *Dislocation reduction in MBE-grown Ge on Si (001) by in situ thermal annealing.* Japanese Journal of Applied Physics, 1988. **27**(9A): p. L1591.

35. J.M. Baribeau, D. Houghton, T. Jackman and J. McCaffrey, *Molecular beam epitaxy growth of Ge on (100) Si.* Journal of The Electrochemical Society, 1989. **136**(4): p. 1158-1162.

36. L. Colace, G. Masini, F. Galluzzi, G. Assanto, G. Capellini, L. Di Gaspare, E. Palange, and F. Evangelisti, *Metal–semiconductor–metal near-infrared light detector based on epitaxial Ge/Si.* Applied Physics Letters, 1998. **72**(24): p. 3175-3177.

37. L. Colace, G. Masini, F. Galluzzi, G. Assanto, G. Capellini, L. Di Gaspare, E. Palange, and F. Evangelisti, *Metal–Ge-Si heterostructures for near-infrared light detection.* Journal of Vacuum Science & Technology B: Microelectronics and Nanometer Structures Processing, Measurement, and Phenomena, 1999. **17**(2): p. 465-467.

38. H.-C. Luan, D.R. Lim, L. Colace, G. Masini, G. Assanto, K. Wada, and L.C. Kimerling, *Germanium photodetectors for silicon microphotonics by direct epitaxy on silicon.* MRS Online Proceedings Library Archive, 1999. **607**.

39. H.-C. Luan, D.R. Lim, K.K. Lee, K.M. Chen, J.G. Sandland, K. Wada, and L.C. Kimerling, *High-quality Ge epilayers on Si with low threading-dislocation densities.* Applied Physics Letters, 1999. **75**(19): p. 2909-2911.

40. T. Langdo, C. Leitz, M. Currie, E. Fitzgerald, A. Lochtefeld, and D. Antoniadis, *High quality Ge on Si by epitaxial necking.* Applied Physics Letters, 2000. **76**(25): p. 3700-3702.

41. J.-S. Park, J. Bai, M. Curtin, B. Adekore, M. Carroll, and A. Lochtefeld, *Defect reduction of selective Ge epitaxy in trenches on Si (001) substrates using aspect ratio trapping.* Applied Physics Letters, 2007. **90**(5): p. 052113.

42. G. Wang, R. Loo, S. Takeuchi, L. Souriau, J. Lin, A. Moussa, H. Bender, B. De Jaeger, P. Ong, and W. Lee, *Fabrication of high quality Ge virtual substrates by selective epitaxial growth in shallow trench isolated Si (001) trenches.* Thin Solid Films, 2010. **518**(9): p. 2538-2541.

43. H. Kanbe, M. Miyaji and T. Ito, *Ge/Si heterojunction photodiodes fabricated by low temperature wafer bonding.* Applied Physics Express, 2008. **1**(7): p. 072301.

44. F. Gity, A. Daly, B. Snyder, F.H. Peters, J. Hayes, C. Colinge, A.P. Morrison, and B. Corbett, *Ge/Si heterojunction photodiodes fabricated by low temperature wafer bonding.* Optics Express, 2013. **21**(14): p. 17309-17314.

45. Y. Kang, M. Zadka, S. Litski, G. Sarid, M. Morse, M. Paniccia, Y.-H. Kuo, J. Bowers, A. Beling, and H.-D. Liu, *Epitaxially-grown Ge/Si avalanche photodiodes for 1.3 μm light detection.* Optics Express, 2008. **16**(13): p. 9365-9371.

46. Y. Kang, H.-D. Liu, M. Morse, M.J. Paniccia, M. Zadka, S. Litski, G. Sarid, A. Pauchard, Y.-H. Kuo, H.-W. Chen, W.S. Zaoui, J.E. Bowers, A. Beling, D.C. McIntosh, X. Zheng, and J.C. Campbell, *Monolithic germanium/silicon avalanche photodiodes with 340 GHz gain–bandwidth product.* Nature Photonics, 2008. **3**(1): p. 59-63.

47. L. Tarof, J. Yu, R. Bruce, D. Knight, T. Baird, and B. Oosterbrink, *High-frequency performance of separate absorption grading, charge, and multiplication InP/InGaAs avalanche photodiodes.* IEEE Photonics Technology Letters, 1993. **5**(6): p. 672-674.

48. C. Xue, H. Xue, B. Cheng, A. Bai, W. Hu, Y. Yu, and Q. Wang. *Si/Ge separated absorption charge multiplication avalanche photodetector with low dark current*. in *2009 6th IEEE International Conference on Group IV Photonics*. 2009. IEEE.

49. X. Wang, L. Chen, W. Chen, H. Cui, Y. Hu, P. Cai, R. Yang, C.-Y. Hong, D. Pan, and K.-W. Ang. *80 GHz bandwidth-gain-product Ge/Si avalanche photodetector by selective Ge growth*. in *Optical Fiber Communication Conference*. 2009. Optical Society of America.

50. N. Duan, T.-Y. Liow, A.E.-J. Lim, L. Ding and G. Lo, *310 GHz gain-bandwidth product Ge/Si avalanche photodetector for 1550 nm light detection.* Optics Express, 2012. **20**(10): p. 11031-11036.

51. A. Sammak, M. Aminian, L.K. Nanver and E. Charbon, *CMOS-Compatible PureGaB Ge-on-Si APD Pixel Arrays.* IEEE Transactions on Electron Devices, 2016. **63**(1): p. 92-99.

52. Z. Lu, Y. Kang, C. Hu, Q. Zhou, H.-D. Liu, and J.C. Campbell, *Geiger-Mode Operation of Ge-on-Si Avalanche Photodiodes.* IEEE Journal of Quantum Electronics, 2011. **47**(5): p. 731-735.

53. R.E. Warburton, G. Intermite, M. Myronov, P. Allred, D.R. Leadley, K. Gallacher, D.J. Paul, N.J. Pilgrim, L.J.M. Lever, Z. Ikonic, R.W. Kelsall, E. Huante-Ceron, A.P. Knights, and G.S. Buller, *Ge-on-Si Single-Photon Avalanche Diode Detectors: Design, Modeling, Fabrication, and Characterization at Wavelengths 1310 and 1550 nm.* IEEE Transactions on Electron Devices, 2013. **60**(11): p. 3807-3813.

54. S. Zhu, K.-W. Ang, S.C. Rustagi, J. Wang, Y. Xiong, G. Lo, and D. Kwong, *Waveguided Ge/Si avalanche photodiode with separate vertical SEG-Ge absorption, lateral Si charge, and multiplication configuration.* IEEE Electron Device Letters, 2009. **30**(9): p. 934-936.

55. Y. Kang, M. Morse, M.J. Paniccia, M. Zadka, Y. Saad, G. Sarid, A. Pauchard, W.S. Zaoui, H.-W. Chen, and D. Dai. *Monolithic Ge/Si avalanche photodiodes*. in *2009 6th IEEE International Conference on Group IV Photonics*. 2009. IEEE.

56. K.-W. Ang, J.W. Ng, A.E.-J. Lim, M.-B. Yu, G.-Q. Lo, and D.-L. Kwong. *Waveguide-integrated Ge/Si avalanche photodetector with 105GHz gain-bandwidth product*. in *Optical Fiber Communication Conference*. 2010. Optical Society of America.

57. C.T. DeRose, D.C. Trotter, W.A. Zortman, A.L. Starbuck, M. Fisher, M.R. Watts, and P.S. Davids, *Ultra compact 45 GHz CMOS compatible Germanium waveguide photodiode with low dark current.* Optics Express, 2011. **19**(25): p. 24897-24904.

58. N. Duan, T.-Y. Liow, A.E. Lim, L. Ding and G. Lo. *High speed waveguide-integrated Ge/Si avalanche photodetector*. in *Optical Fiber Communication Conference*. 2013. Optical Society of America.

59. N.J. Martinez, C.T. Derose, R.W. Brock, A.L. Starbuck, A.T. Pomerene, A.L. Lentine, D.C. Trotter, and P.S. Davids, *High performance waveguide-coupled Ge-on-Si linear mode avalanche photodiodes.* Optics Express, 2016. **24**(17): p. 19072-81.

60. N.J. Martinez, M. Gehl, C.T. Derose, A.L. Starbuck, A.T. Pomerene, A.L. Lentine, D.C. Trotter, and P.S. Davids, *Single photon detection in a waveguide-coupled Ge-on-Si lateral avalanche photodiode.* Optics Express, 2017. **25**(14): p. 16130-16139.

61. Y. Kang, P. Mages, A. Clawson, P. Yu, M. Bitter, Z. Pan, A. Pauchard, S. Hummel, and Y. Lo, *Fused InGaAs-Si avalanche photodiodes with low-noise performances.* IEEE Photonics Technology Letters, 2002. **14**(11): p. 1593-1595.

62. Y. Kang, Y.-H. Lo, M. Bitter, S. Kristjansson, Z. Pan, and A. Pauchard, *InGaAs-on-Si single photon avalanche photodetectors.* Applied Physics Letters, 2004. **85**(10): p. 1668-1670.

63. Y. Kang, P. Mages, A. Pauchard, A. Clawson, S. Lau, Y. Lo, and P. Yu. *Dark current reduction in fused InGaAs/Si avalanche photodiode*. in *LEOS 2001. 14th Annual Meeting of the IEEE Lasers and Electro-Optics Society (Cat. No. 01CH37242)*. 2001. IEEE.

Chapter 4. Design, modelling, fabrication and optical characterisation

4.1 Introduction

In Chapters 2 and 3, the advantages and disadvantages of single-photon detectors made using different material systems and different structures were described. Silicon SPADs are well developed and commonly used for single-photon applications in the visible and near-infrared (NIR) wavelength regions. However, Si detectors are not capable of efficiently detecting light at wavelengths greater than ~1 μm. A hetero-structure device that uses Ge for the absorption layer and Si for the multiplication layer benefits from well-developed Si technology while expanding the wavelength of operation beyond the Si cut-off, up to 1.55 μm. Such detectors show promise for high sensitivity, high count rate and low cost. In addition, when integrated on Si platforms these devices provide the route towards the development of large arrays of Ge-on-Si SPADs for use in eye-safe automotive light detection and ranging (LIDAR) and future quantum technology applications. Previous generations of Ge-on-Si single-photon avalanche diodes (SPADs) have been designed, simulated and characterised by previous members of our group as well as several other research groups [1-5]. A brief summary of relevant work by previous group members will be given, followed by a description of the new Ge-on-Si SPAD designs. The modelling software Silvaco ATLAS was used to perform simulations of dark current and electric field profiles of the prospective detectors. A comparison of the electric field simulation results for each design will be given along with a discussion of the key findings. A brief summary of the device fabrication will be followed by an initial current-voltage characterisation of the resulting SPADs.

4.2 Device structure. Challenges of a mesa geometry Ge-on-Si SPADs

As mentioned in Chapter 3, previous Ge-on-Si SPADs developed by our group were designed as mesa geometry separate absorption charge multiplication (SACM) structures [1]. The main advantage of such a structure is that absorption and multiplication regions can be optimised independently [6]. This is especially important when designing a hetero-structure device using materials with different electrical properties. In the case of Ge-on-Si SPADs the incident short-wave infrared (SWIR) radiation is absorbed in the Ge absorption region, which is sensitive to radiation of up to 1.6 μm wavelength at room temperature, while signal amplification takes place in the Si multiplication region. In

between these regions, a charge sheet is used to control the electric field such that the field is high enough in the multiplication region to ensure that avalanche breakdown is reached and low enough in the absorption region to prevent band-to-band and trap-assisted tunnelling. A low electric field, however, is maintained in the Ge layer to allow efficient drift of photo-generated electrons into the multiplication region. The SPAD is operated above the avalanche breakdown voltage in Geiger mode.

In this device, a single photon absorbed in the Ge layer creates an electron-hole-pair, and the electron drifts into the Si multiplication region. Here it accelerates, gaining sufficient kinetic energy to undergo impact ionisation, creating an electron-hole-pair. The secondary electrons and holes are in turn accelerated and impact ionise, creating further electron-hole pairs. Further impact ionisation of both holes and electrons rapidly creates a large avalanche current (~mA) which can be self-sustaining if the device is biased above avalanche breakdown. Under these conditions, this results in a detectable electronic signal, which can be timed relative to the initial laser pulse. After detection, it is necessary to bias the SPAD momentarily below avalanche breakdown to quench the avalanche, after which the SPAD can return to its quiescent state ready to detect further incident photons. At room temperature, electrons reach the saturation velocity at ~30 kV/cm in Ge [7]. Assuming the doping profile of the germanium absorber is low and the electric field of the region is uniform, this number represents the lower limit of the electric field strength required to reach the velocity saturation. Figure 4.1 illustrates the typical carrier characteristics for both electrons and holes for Si, Ge and GaAs. It can be observed from Figure 4.1 that carrier mobility in Ge is greater compared to Si. Although electrons in Ge reach saturation velocity at relatively low electric field of 4 kV/cm while electrons in Si reach saturation at 20 kV/cm, their saturation velocity is a factor of 2 greater compared to electrons in Ge. SPAD detectors are operated above breakdown voltage, which corresponds to high electric fields of ~300 kV/cm in Si multiplication layer.

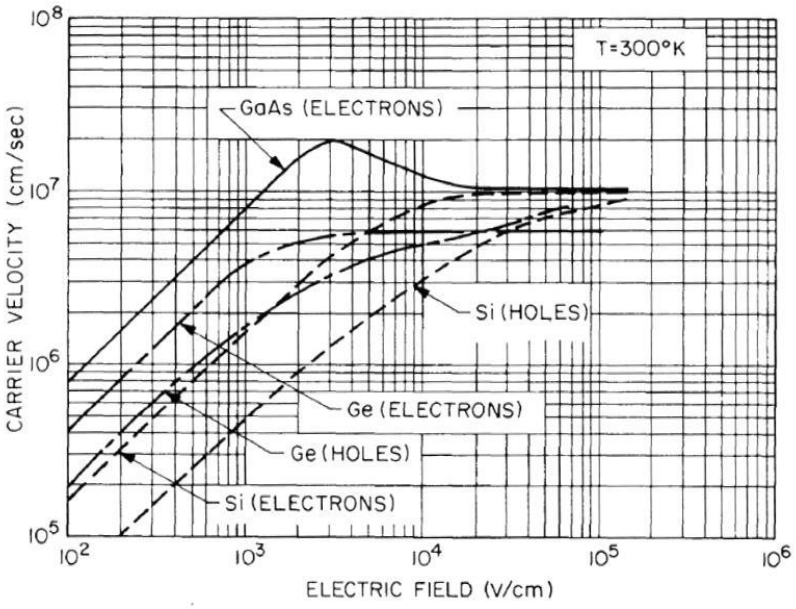

Figure 4.1. Measured carrier velocity as a function of the electric field for intrinsic Ge, Si and GaAs [7].

Figure 4.2 illustrates the cross section of a cylindrical mesa Ge-on-Si SPAD reported by Warburton *et al.* [1].

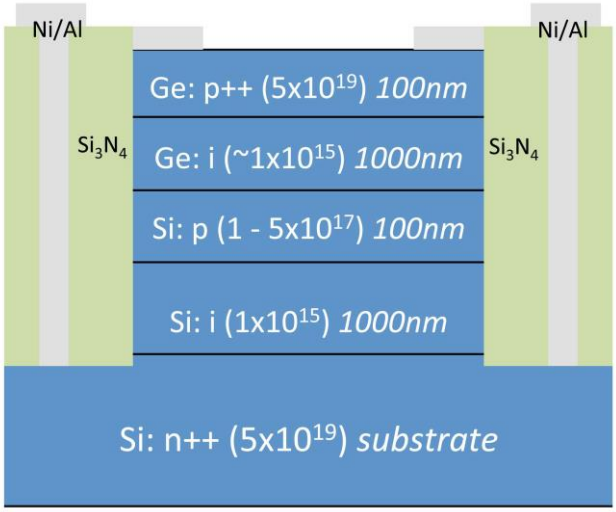

Figure 4.2. A cross section of a mesa structure Ge-on-Si SPAD reported in [1].

In order to fabricate these mesa devices, a device fabrication process was developed. An inductively coupled plasma reactive ion etch using fluorine-based chemistry (SF_6/C_4F_8) was used to define the individual mesas. Si_3N_4 was used for the sidewall passivation. These detectors exhibited high dark count rates (DCR) of ~Mcount/s and considerably low single-photon detection efficiency (SPDE) of 4% at a detection wavelength of 1310 nm. It has been shown previously that the main contribution to the leakage current

of small active area devices is related to the sidewall component [8]. Defects and threading dislocations at the Ge/Si interface along the exposed sidewalls make a significant contribution to the dark current and DCR as a result. It was possible to draw a similar conclusion for the dark current of the mesa geometry Ge-on-Si SPAD devices. Therefore, different passivation techniques such as SiO_2, GeO_2, and atomic layer deposition (ALD) were investigated with the aim of mitigating the current contribution from the sidewalls of the device. However, optimal passivation for two different materials, Ge and Si, remains challenging.

Modern Si and InGaAs/InP SPADs are typically fabricated in a planar geometry [9-11], with the p-n junction formed by post-growth dopant diffusion or ion implantation [12, 13]. Initial research utilises mesa structures due to reproducibility and fabrication simplicity. However, planar geometry structures are more reliable and have several advantages over the mesa geometry. The main and most immediate issues being addressed are the sidewall contribution to the dark current, and reduced efficiency due to premature edge breakdown. Hence, the main focus of our work was to design and characterise a planar geometry Ge-on-Si SPAD.

4.3 Proposed planar geometry Ge-on-Si SPADs

For the basic underlying design for a planar geometry Ge-on-Si SPAD, we have retained the SACM layer structure discussed previously. Such a structure allows an electric field lower than breakdown field (100 kV/cm) to be maintained in the Ge absorption region while allowing the high electric field (over 300 kV/cm) in the Si multiplication region necessary to trigger a self-sustaining avalanche. Fabrication of planar geometry devices involves two growth steps. First, the Si multiplication layer was grown and ion beam implantation was employed to form charge sheets for prospective devices. Next, after surface cleaning, the Ge absorption layer was grown and second round of ion implantation was used to form p^{++} Ge top contacts. The initial idea for a planar geometry device was to define the SPADs only by means of ion implanted charge and p^{++} top contact layers. However, preliminary tests of those structures showed a lack of electrical isolation between the devices. Hence, a decision was made to etch through Ge absorption layer to insure the isolation, thus creating a superpixel structure.

Three different designs varying the widths of the p^{++} Ge top contact in respect to the charge sheet were developed. In addition, a partially etched mesa geometry device was

developed in order to confirm that defects along the exposed sidewalls significantly contribute to the DCR. Figures 4.3 – 4.6 illustrate the proposed designs. All four designs consisted of a 1.5 µm thick intrinsic Si layer as a multiplication layer, 0.1 µm thick Si charge sheet layer, a 1 µm thick intrinsic Ge layer as an absorber and 50 nm thick Ge top contact layer. The charge sheet diameter for all designs varied between 25 µm and 200 µm. The doping concentration of the p++ top contact was 5×10^{19} cm^{-3}. As will be discussed in Section 4.5, the charge sheet layer doping concentrations varied between 1×10^{19} cm^{-3} and 5×10^{19} cm^{-3}. In Design 1, as illustrated in Figure 4.3, the p^{++} top contact and the charge layer have the same diameter. In Design 2, as illustrated in Figure 4.4, the diameter of the top contact was increased by 10 µm and reduced by the 10 µm in Design 3, which is illustrated in Figure 4.5. The isolating trenches were created 10 µm away from the charge sheet layer. The structure of Design 4, which is illustrates in Figure 4.6 is similar to Design 1 except for the position of the trench. The structure was fabricated as a partially etched mesa device.

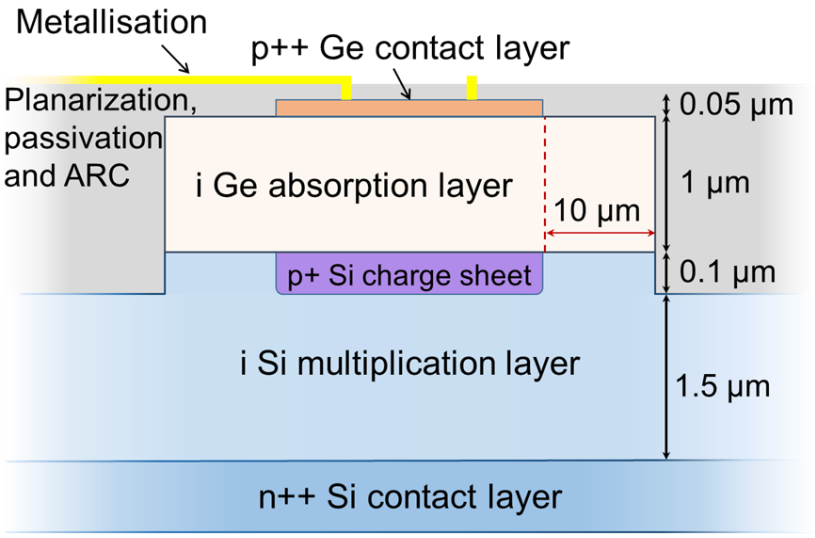

Figure 4.3. Proposed Design 1: the width of the top contact layer is equal to the width of the charge layer. The distance between the charge layer and the trench is 10 µm. The diameter of the charge sheet varied between 25 µm and 200 µm.

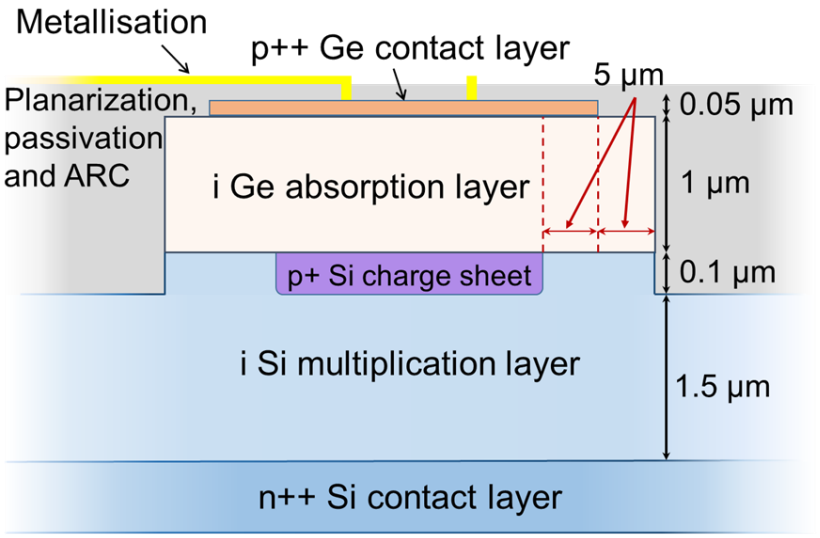

Design 2: $w_{tc} > w_{cs}$

Figure 4.4. Proposed Design 2: the width of the top contact layer is 10 µm greater than the width of the charge layer. The distance between the charge layer and the trench is 10 µm. The diameter of the charge sheet varied between 25 µm and 200 µm.

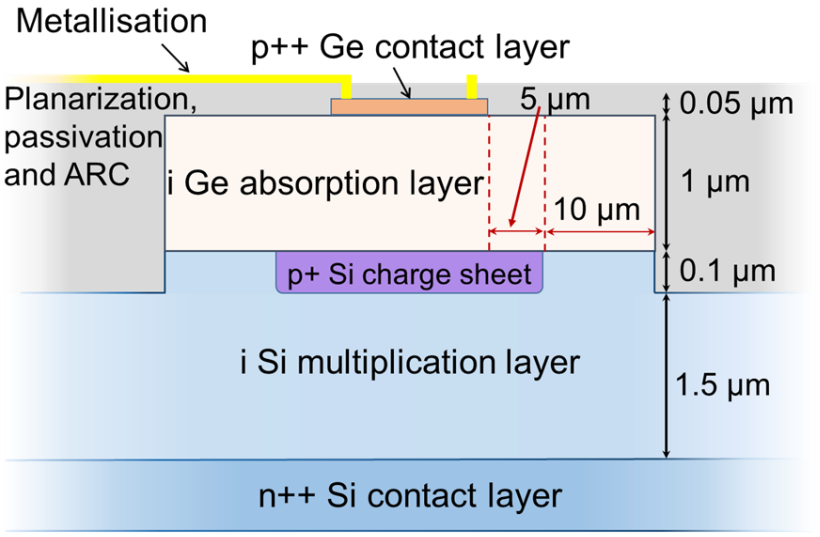

Design 3: $w_{tc} < w_{cs}$

Figure 4.5. Proposed Design 3: the width of the top contact layer is 10 µm smaller than the width of the charge layer. The distance between the charge layer and the trench is 10 µm. The diameter of the charge sheet varied between 25 µm and 200 µm. This diagram was also used in Ref. [14].

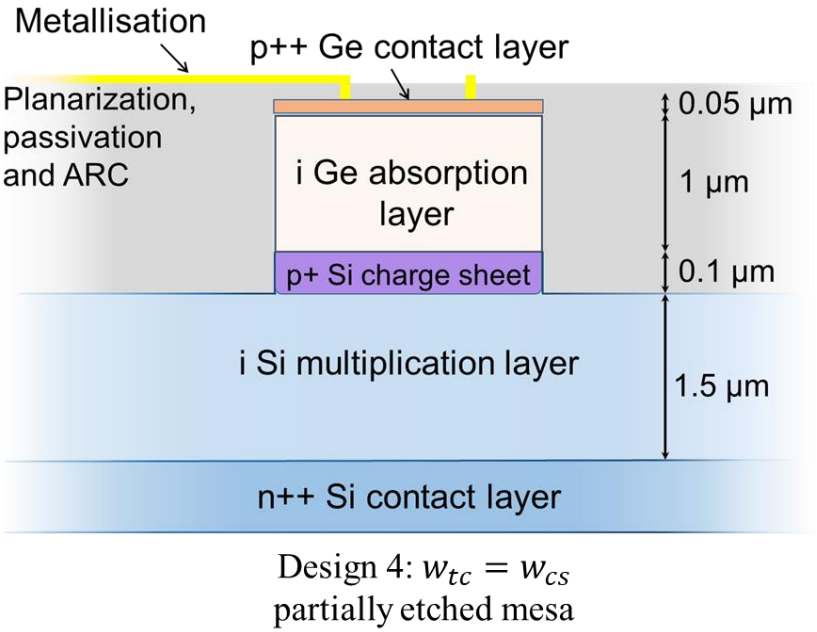

Figure 4.6. Proposed Design 4: partially etched mesa geometry. The width of the top contact layer is equal to the width of the charge layer. The diameter of the charge sheet varied between 25 µm and 200 µm.

The top contact, aligned with the charge sheet layer, defined the SPAD. The main aim of the new planar geometry design was to confine the high electric field along the centre of the device away from the exposed sidewalls introduced by the superpixel. By varying the diameter of the Ge p^{++} top contact in respect to the charge layer we investigated the distribution of the electric field inside the detector. Next section will present an investigation into the simulation of these proposed designs performed prior to the device manufacture.

4.4 Modelling of Ge-on-Si hetero-structures

To understand the implications of the design choices presented above, finite element analysis modelling using Silvaco ATLAS have been performed to examine the electric field profiles. By observing which designs had optimal electric fields profiles throughout, the charge sheet doping levels and the thicknesses of the multiplication and absorption regions, as well as the optimum overall design dimensions of the SPAD have been determined.

The first step of the simulation process is to define the structure and generate the appropriate mesh. The simulation mesh represents the points of the structure where the

software solves the model used for electric field analysis. Those points are called nodes, and the number of these nodes directly influences the simulation computational time and detailed spatial resolution. High accuracy requires a fine mesh, however, the total number of grid point in 2D Atlas simulations is limited to 20 000. Of course, computational time significantly increases with the higher number of nodes [15]. Hence, a compromise between the accuracy and the simulation efficiency has to be established. To effectively balance accuracy against efficiency, a finer grid is used in critical parts of the device structure where the electric field gradient is high, such as the vicinity of the ion implantation, or near sharp corners of the structure. For the simulations of the 25 µm diameter cylindrical detectors discussed in this Chapter, the mesh parameters displayed in Table 4.1 were used:

Table 4.1. The mesh parameters used for the simulations shown in this Chapter

Region and thickness of the simulated 25 µm planar Ge-on-Si SPAD	Minimum width of the mesh triangle	Minimum height of the mesh triangle
Ge p^{++} top contact, 50 nm	100 nm	5 nm
Ge i absorption, 1000 nm	100 nm	50 nm
Si p charge sheet, 100 nm	100 nm	5 nm
Si i multiplication, 1400 nm	100 nm	50 nm
Si n^{++} substrate, 500 nm	100 nm	50 nm

The fine mesh was used in the Ge p^{++} top contact layer and the Si charge layer since both of those regions have been created using ion implantation and had high doping concentrations. In the Ge absorption region and the Si multiplication region we used an order of magnitude greater mesh since those regions were an order of magnitude wider and have more uniform electric fields. The spacing in the lateral direction was 1-2 orders of magnitude larger since the electric field is created in the vertical direction. All the electric field profiles are simulations of the 2D cross section of the device. Figures 4.7 – 4.10 show the simulations of the electric field profiles for 5% excess bias or a potential held at 5% above the avalanche breakdown voltage. It is clear that the electric field profile is different for each design. Design 3 illustrated in Figure 4.9 showed the most promising electric field distribution. There is a low electric field in the Ge absorber at breakdown, and, crucially, the high electric field is confined to the centre of the SPAD preventing carriers originating at the sidewalls from causing breakdown events.

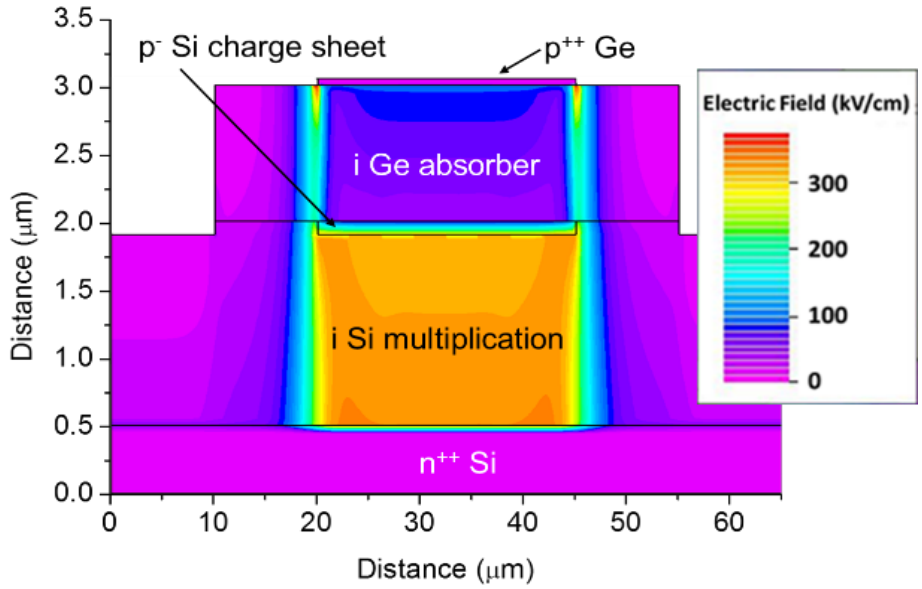

Figure 4.7. The electric field profile of a Design 1 Ge-on-Si SPAD at 5 % excess bias above the breakdown. Design 1 is described in Figure 4.3. The charge sheet diameter of the simulated detector is 25 μm and the mesh parameters used as described in Table 4.1.

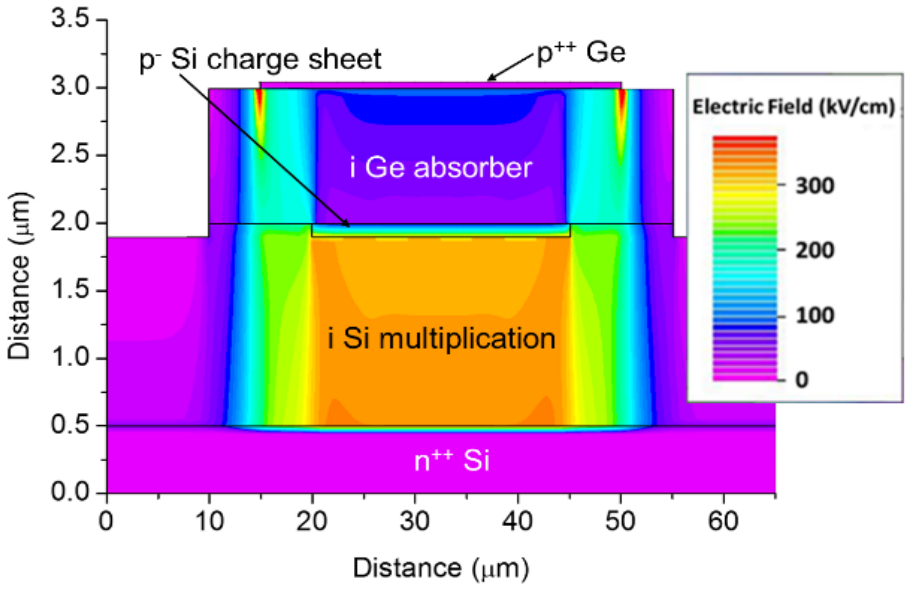

Figure 4.8. The electric field profile of a Design 2 Ge-on-Si SPAD at 5 % excess bias above the breakdown. Design 2 is described in Figure 4.4. The charge sheet diameter of the simulated detector is 25 μm and the mesh parameters used as described in Table 4.1.

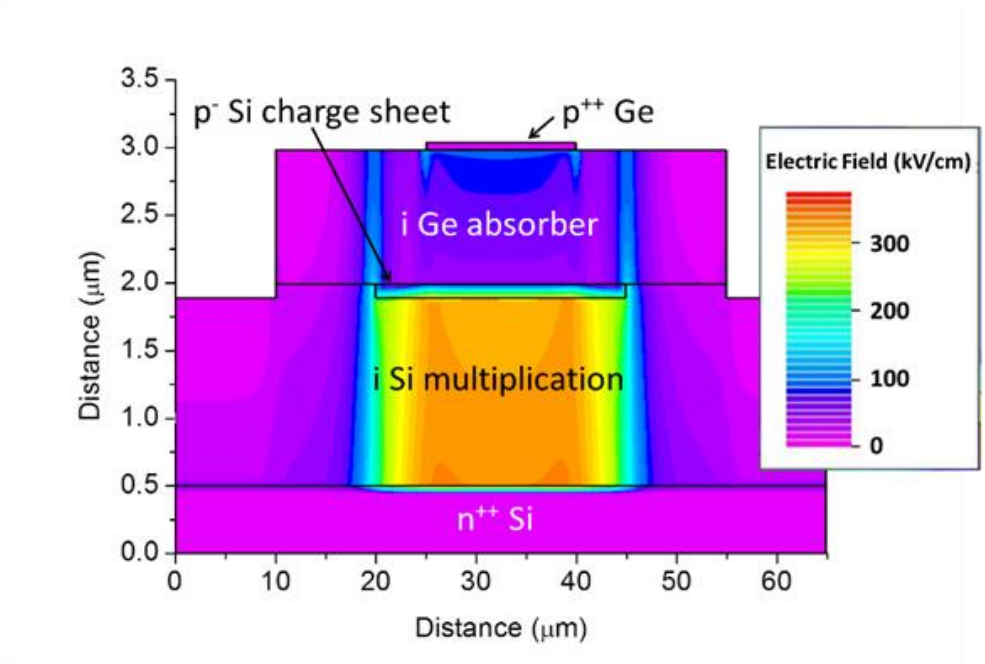

Figure 4.9. The electric field profile of a Design 3 Ge-on-Si SPAD at 5 % excess bias above the breakdown. Design 3 is described in Figure 4.5. The charge sheet diameter of the simulated detector is 25 μm and the mesh parameters used as described in Table 4.1. This diagram was also used in Ref. [14].

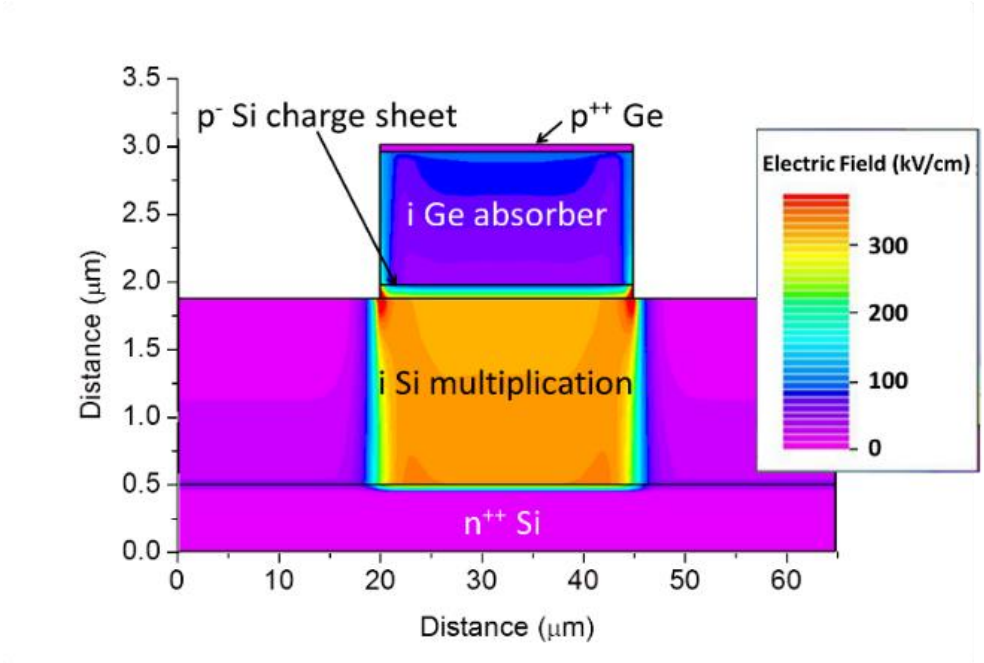

Figure 4.10. The electric field profile of a Design 4 Ge-on-Si SPAD at 5 % excess bias above the breakdown. Design 4 is described in Figure 4.6. The charge sheet diameter of the simulated detector is 25 μm and the mesh parameters used as described in Table 4.1. This diagram was also used in Ref. [14].

Other designs also had similar electric field profiles along the centre of the device. However, it is clear from Figure 4.7 and Figure 4.8 that even though electric field is low at the sidewalls it is significantly high at the edges of the top contact. This can potentially cause edge breakdown [16] which will ultimately cause reduced device detection efficiency as the central region will have a lower electric field. For both designs the field there is higher than the breakdown field strength for Ge of 100 kV/cm [7]. Thermally generated events under such high electric field will cause a detectible current and lead to dark events.

Using the same mesh parameters, the electric field profiles of the structures similar to Design 3 (Figure 4.5) varying the distance between the charge sheet and the sidewall have been also investigated. This dimension may also prove important for creating future Ge-on-Si SPAD arrays since it will directly affect the fill factor, which is a ratio between the pixel's active area to its total area.

Figure 4.11 – 4.14 show sections of the electric field profiles from the FiguresFigure 4.7 – 4.10 zoomed in near the edge of the charge sheet for clarity. This is to demonstrate that designs 1, 2 and 4 (partially etched mesa) had potential issues due to the high electric field near the edge of the top contact and along the sidewalls for the Design 4. These figures illustrate 20 μm wide cross sections of the prospective detectors near the edge of the charge layer. It can be observed that the electric field is above the breakdown in Si multiplication layer (> 300 kV/cm) and it is well below breakdown and the tunnelling threshold in the Ge absorber (< 100 kV/cm) along the centre of the device for all the designs. However, the electric field near the edge of the top contact is ~ 300 kV/cm in Ge absorber for Design 1 and significantly higher than 300 kV/cm for Design 2. In partially etched mesa, Design 4, the electric field along the sidewalls is ~ 200 kV/cm and significantly greater than 300 kV/cm at the sidewall etch near the edge of the charge layer. As for Design 3, the electric field is above breakdown in Si multiplication region and below breakdown in Ge absorber and the high electric field is confined in the centre of the device as desired. From these results, it is clear that Design 3 shows the greater promise of our proposed devices due to high electric field confined along the centre of the device away from the exposed sidewalls and due to absence of the high electric field features near the edge of the top contact. Therefore, further simulations were performed for Design 3 only.

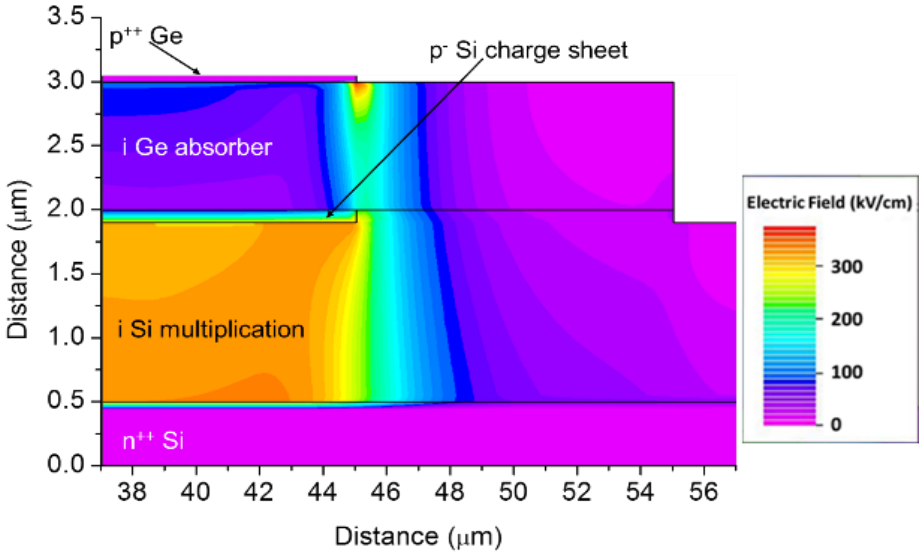

Figure 4.11. A section of the electric field profile of a Design 1 Ge-on-Si SPAD at 5 % excess bias above the breakdown. It displays a 20 μm wide cross section of the simulated detectors zoomed in near the edge of the charge sheet layer. The charge sheet diameter of the simulated detectors is 25 μm and the mesh parameters used as described in Table 4.1.

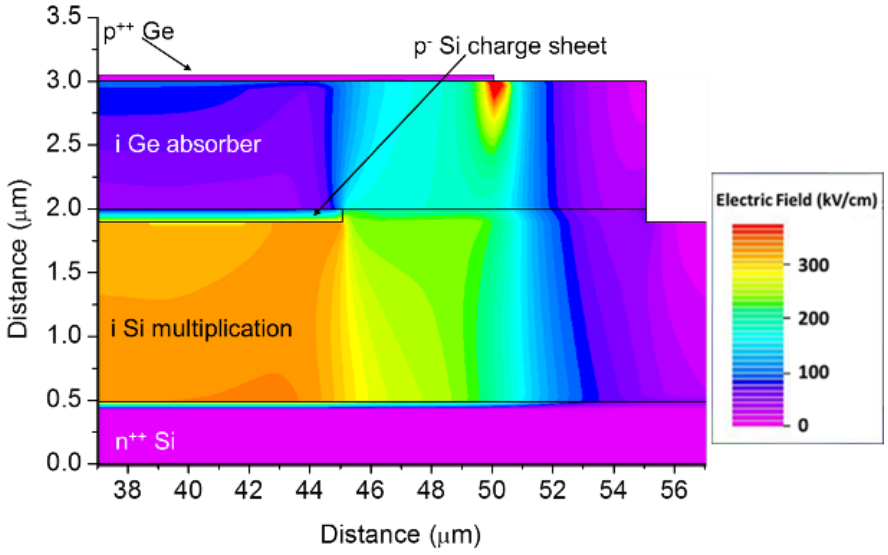

Figure 4.12. A section of the electric field profile of a Design 2 Ge-on-Si SPAD at 5 % excess bias above the breakdown. It displays a 20 μm wide cross section of the simulated detectors zoomed in near the edge of the charge sheet layer. The charge sheet diameter of the simulated detectors is 25 μm and the mesh parameters used as described in Table 4.1.

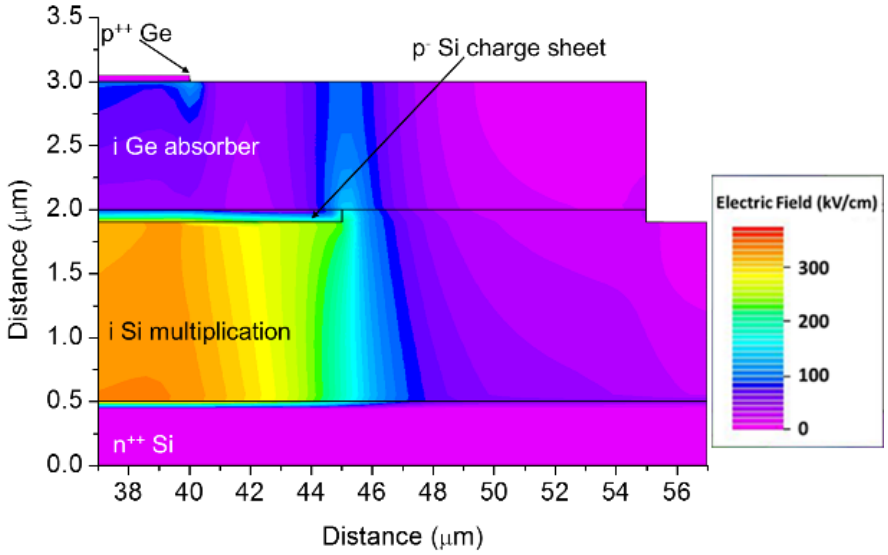

Figure 4.13. A section of the electric field profile of a Design 3 Ge-on-Si SPAD at 5 % excess bias above the breakdown. It displays a 20 μm wide cross section of the simulated detectors zoomed in near the edge of the charge sheet layer. The charge sheet diameter of the simulated detectors is 25 μm and the mesh parameters used as described in Table 4.1.

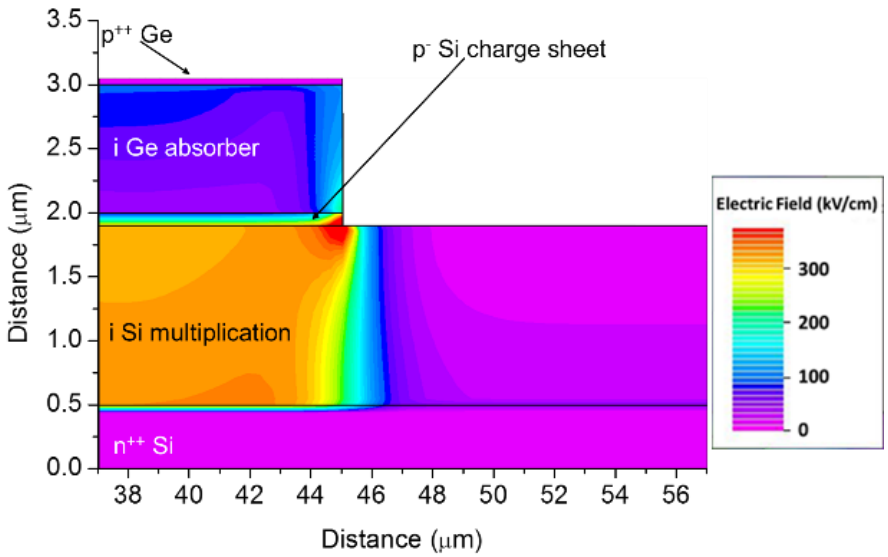

Figure 4.14. A section of the electric field profile of a Design 4 Ge-on-Si SPAD at 5 % excess bias above the breakdown. It displays a 20 μm wide cross section of the simulated detectors zoomed in near the edge of the charge sheet layer. The charge sheet diameter of the simulated detectors is 25 μm and the mesh parameters used as described in Table 4.1.

The next round of simulations was aimed to determine the minimum distance between the charge sheet layer and the trench. Based on the results for partially etched mesa design we suspected that having the trench next to the charge layer could lead to issues such as sidewall current leakage and edge breakdown. However, reducing this distance further is useful for future Ge-on-Si SPAD arrays, since a smaller distance between the SPAD and the trench would allow individual SPADs to be placed closer together in the array, thus increasing the fill factor. Distances from 5 μm down to 0 μm between the implanted charge sheet to the trench were considered. Figure 4.15 – 4.18 show 20 μm wide sections of the corresponding electric field profiles of a 25 μm diameter planar Ge-on-Si SPAD configured in the Design 3 geometry at 5% excess bias above breakdown zoomed in near the edge of the charge sheet layer. It is clear from Figure 4.15 that if the sidewall is formed in line with the charge layer, a region of high electric field will be formed near the bottom of the trench, which can lead to edge breakdown and increased dark count rates. It can be observed from the Figures 4.15 – 4.18 that this high electric field region at the edge of the charge sheet near the bottom of the sidewall decreases as the distance to the charge sheet increases. When the distance between the charge sheet and the sidewall is zero, the field is greater than breakdown field of Si (300 kV/cm) and this is reduced to ~ 150 kV/cm when the distance is increased to 2 μm, and further reduced down to ~100 kV/cm at a distance of 3 μm. The electric field near the bottom of the trench becomes negligible at a distance of 5 μm. Hence, the isolating trench has to be positioned at distances greater than 3 μm.

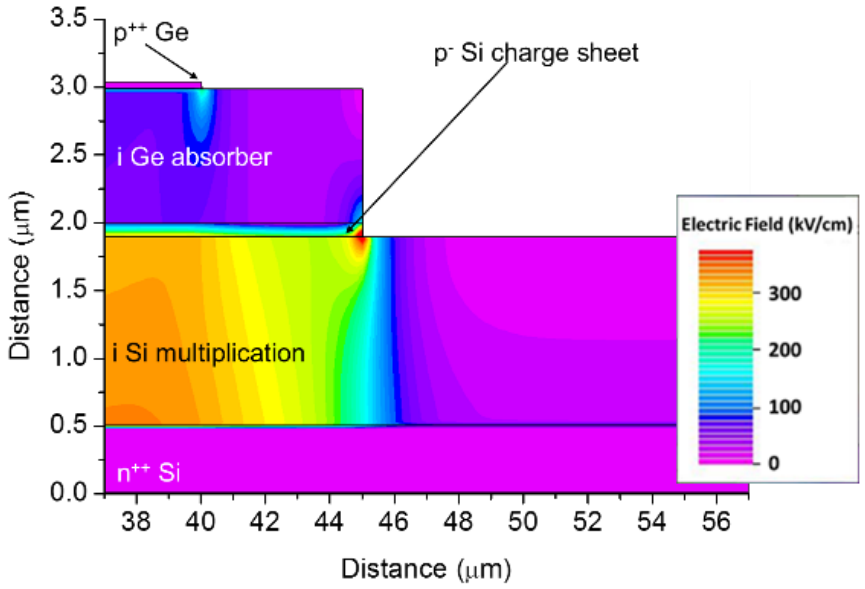

Figure 4.15. A section of the electric field profile at 5 % excess bias above the breakdown of a 25 μm diameter planar Ge-on-Si SPAD configured in the Design 3 geometry. The diagrams display a 20 μm wide cross section of the detectors zoomed in at near the edge of the charge sheet layer. The distance between the charge sheet layer of the device and the sidewall is 0 μm.

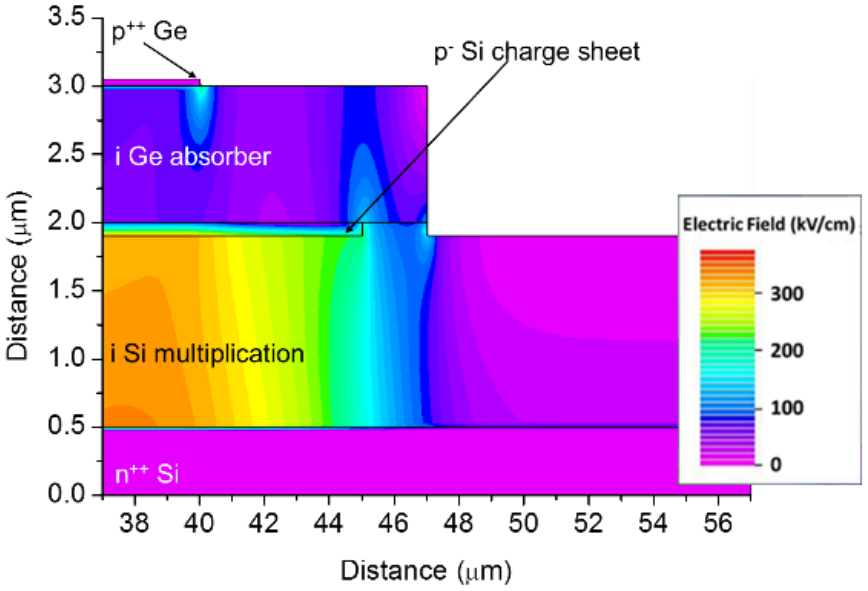

Figure 4.16. A section of the electric field profile at 5 % excess bias above the breakdown of a 25 μm diameter planar Ge-on-Si SPAD configured in the Design 3 geometry. The diagrams display a 20 μm wide cross section of the detectors zoomed in at near the edge of the charge sheet layer. The distance between the charge sheet layer of the device and the sidewall is 2 μm.

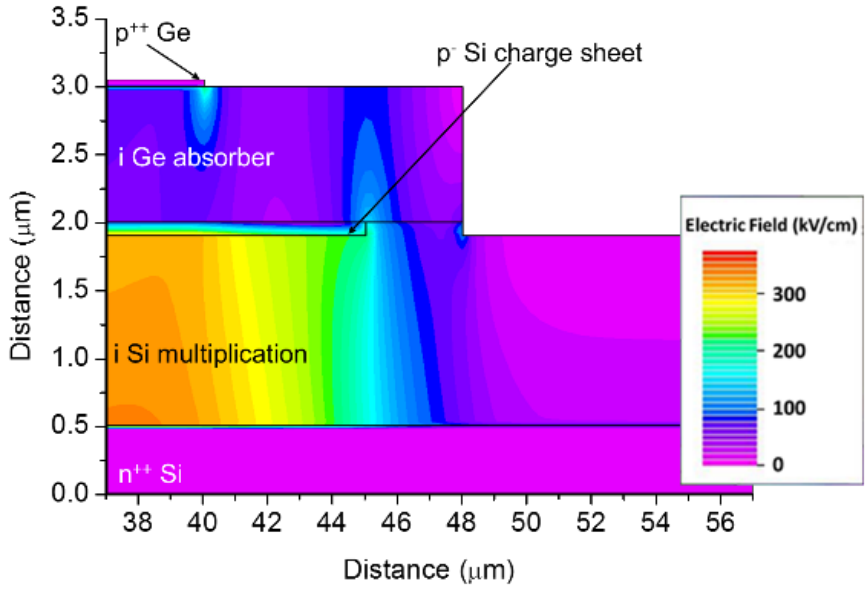

Figure 4.17. A section of the electric field profile at 5 % excess bias above the breakdown of a 25 μm diameter planar Ge-on-Si SPAD configured in the Design 3 geometry. The diagrams display a 20 μm wide cross section of the detectors zoomed in at near the edge of the charge sheet layer. The distance between the charge sheet layer of the device and the sidewall is 3 μm.

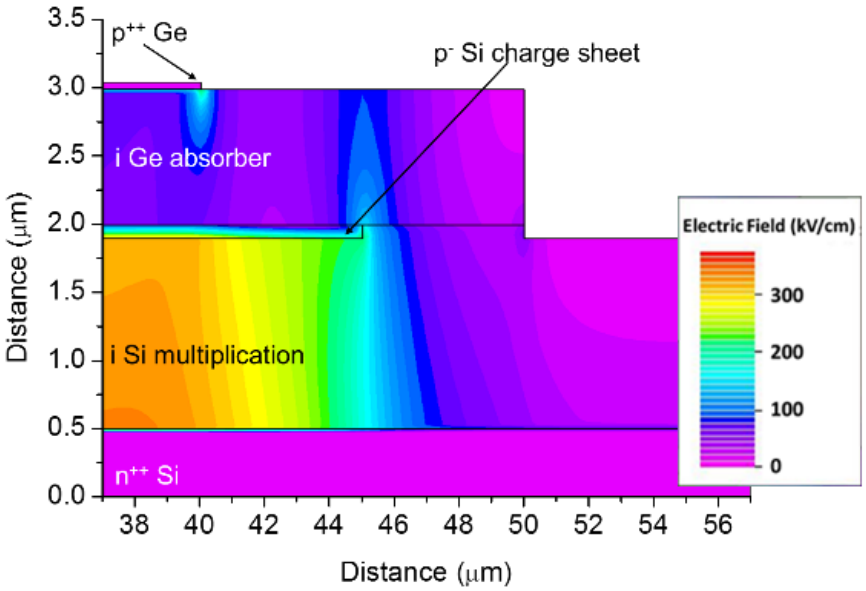

Figure 4.18. A section of the electric field profile at 5 % excess bias above the breakdown of a 25 μm diameter planar Ge-on-Si SPAD configured in the Design 3 geometry. The diagrams display a 20 μm wide cross section of the detectors zoomed in at near the edge of the charge sheet layer. The distance between the charge sheet layer of the device and the sidewall is 5 μm.

The above device designs were mainly focused on confining the high electric field along the centre of the device. However, the thickness of the absorption layer directly affects the performance of the SPAD. In principle, a thicker absorber leads to greater absorption and greater numbers of photogenerated carriers. The amount of light absorbed by a semiconductor can be estimated using Lambert-Beer´s Law:

$$I(\lambda, x) = [1 - R(\lambda)]I_0(\lambda)e^{-\alpha(\lambda)x}; \quad (1)$$

where λ is the wavelength of illumination, x is the distance into the semiconductor from the illuminated surface and $I_0(\lambda)$, $R(\lambda)$ and $\alpha(\lambda)$ are the intensity of illumination, surface reflectance and absorption coefficient, respectively, at wavelength λ. Assuming the presence of the anti-reflective coating, $R(\lambda) = 0$, and using the absorption coefficients for intrinsic Ge at 300 K ($\alpha \sim 0.55\times10^4$ cm^{-1}) and 77 K ($\alpha \sim 0.7\times10^4$ cm^{-1}) from reference [17], we estimate that less than 50% of 1310 nm wavelength light is absorbed in the 1 µm Ge absorption layer. According to our estimation 67% of light would be absorbed at 77 K (75% at 300 K) and 80% at 77 K (88% at 300 K) within 2 µm and 3 µm thick Ge absorber respectively. Therefore, it has been proposed to fabricate the future generations of Ge-on-Si SPADs with absorber layers of 2 µm and 3 µm thickness. Figures 4.19 – 4.21 show the corresponding electric field simulations.

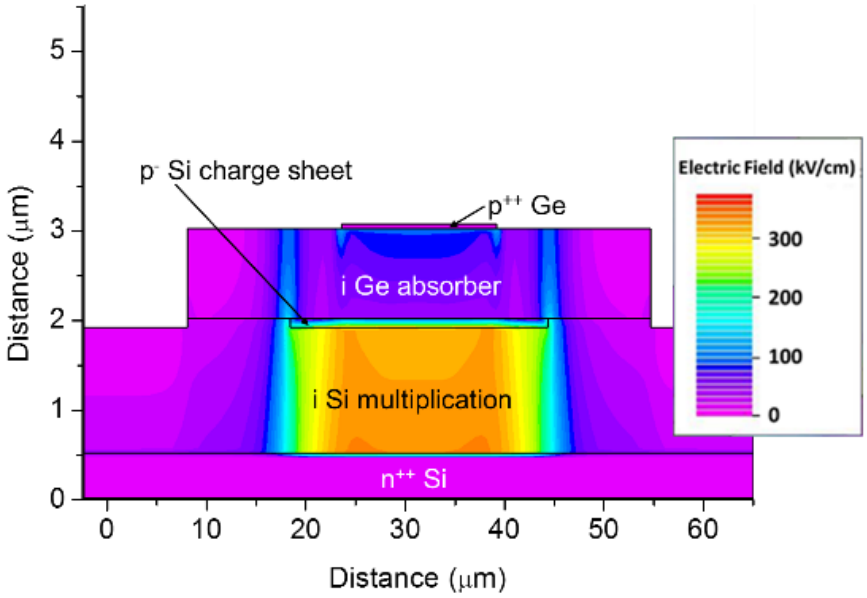

Figure 4.19. The electric field profile at 5% excess bias above the breakdown of a Design 3 25 µm diameter planar Ge-on-Si SPAD. The distance between the charge sheet layer of the device and the trench is 10 µm. The thickness of the absorption layer is 1 µm.

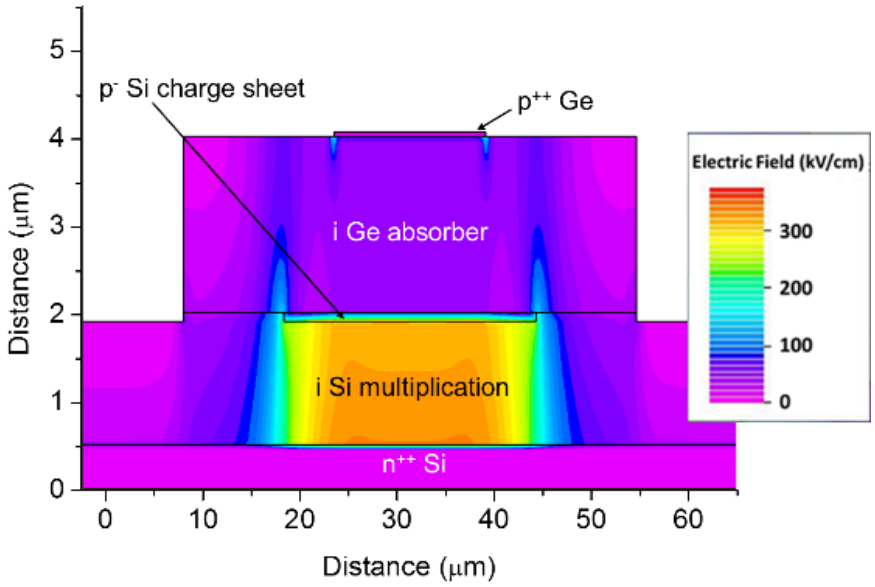

Figure 4.20. The electric field profile at 5% excess bias above the breakdown of a Design 3 25 μm diameter planar Ge-on-Si SPAD. The distance between the charge sheet layer of the device and the trench is 10 μm. The thickness of the absorption layer is 2 μm.

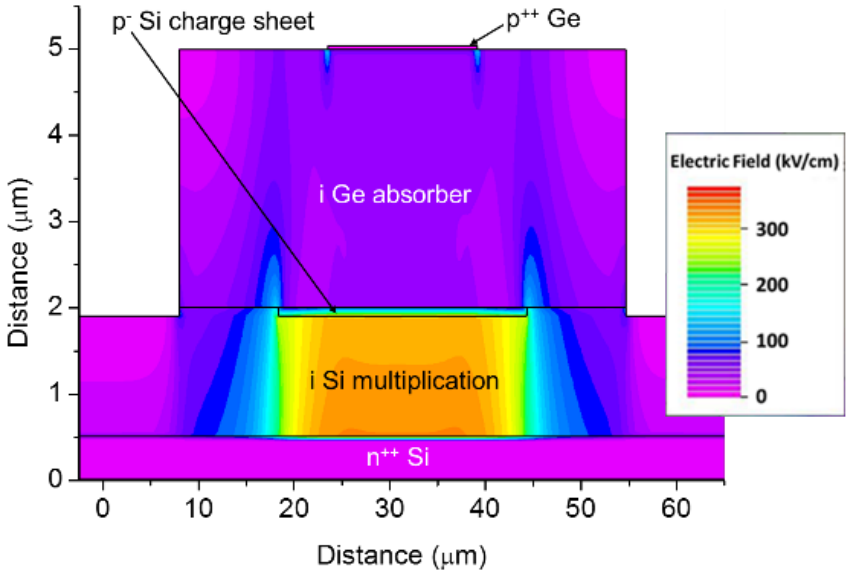

Figure 4.21. The electric field profile at 5% excess bias above the breakdown of a Design 3 25 μm diameter planar Ge-on-Si SPAD. The distance between the charge sheet layer of the device and the trench is 10 μm. The thickness of the absorption layer is 3 μm.

It is clear from the Figures 4.19 – 4.21 that the developed Design 3 would successfully confine the high electric field along the centre of the device and away from the exposed

sidewalls preventing the deleterious contributions to the dark count rate. However, it can be observed that the electric field near the bottom of the sidewall is higher for the detector with a 3 μm absorber compared to the detector with the 1 μm absorption layer. This suggests that the distance between the charge sheet and the trench may have to be increased. Further experimental investigation is required to establish the minimum distance possible to satisfy both parameters, performance of the device and the sufficient fill factor for potential Ge-on-Si SPAD arrays.

From the simulations results we suspected that Design 3 would be the most successful out of all. In addition, since both the charge sheet and the top contact were created by the ion beam implantation we fully expected that those layers might not have the perfectly cylindrical shape modelled in these simulations. In practice, there will not be a sharp delineation between ion-implanted regions and the non-implanted neighbouring region. Hence, further experimental investigation was required.

4.5 Device fabrication

This section describes the planar Ge-on-Si SPAD growth and fabrication process. Five structures with different charge sheets were grown on 150 mm diameter n++-doped Si (001) substrates. Firstly, a 1.5 μm thick Si multiplication region was grown epitaxially by a commercial reduced pressure chemical vapour deposition (RP-CVD) system. Photolithography was used to define the charge sheet regions, which were then implanted with boron acceptors at an energy of 10 keV. Different charge sheet doses were implanted in each of the five wafers to account for fabrication tolerances and ensure that the optimised electric field profile was achieved in at least one of the wafers. After implantation, the boron dopants were activated at 950 ˚C for 30 s using a rapid thermal annealer. After RCA cleaning, a 1 μm thick, nominally undoped Ge absorption layer and a 50 nm p++ Ge top contact layer were grown on top of the selectively implanted Si layer using RP-CVD. An etch through the Ge was created at a lateral distance of 10 μm from the charge sheet, in order to create the superpixel and electrically isolate the SPADs, as shown in Figure 4.3 – 4.6. This electrical isolation was required due to the conductive path formed by the background doping level found in the Ge layer. Metal contacts, GeO_2 passivation, anti-reflection (AR) coatings and bond-pads were subsequently deposited.

As a first step, to determine which of the wafers would be used for the Ge-on-Si SPADs fabrication, our collaborators from University of Glasgow made partially etched SPADs

using the five different charge sheet doping concentration wafers. Initial measurements were performed using the cryogenic micromanipulated probe station (Janis). Figure 4.22 illustrates a schematic diagram of the set-up used for dark current and photocurrent measurements.

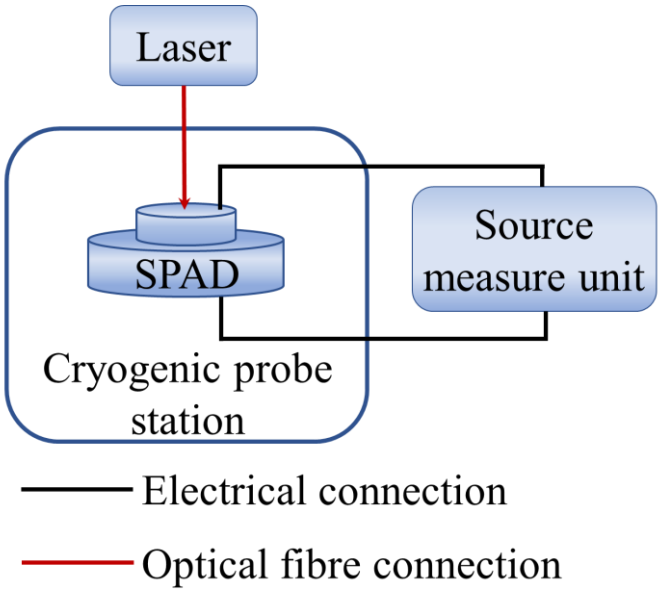

Figure 4.22. A schematic diagram of the set-up used for initial dark current and photocurrent measurements of the Ge-on-Si SPAD detectors.

The probe station has a multimode optical fibre probe that allowed us to flood the active area of the detectors with infrared illumination. Keithley 2450 source measure unit was used to reverse bias the devices and to measure the corresponding current in both dark current and photocurrent measurements. The current-voltage characteristics of 100 µm diameter SPADs made from different charge sheet doping concentration wafers are presented in figures below. Figure 4.23 shows typical dark current of 100 µm diameter SPADs for each of the wafers after analysis of approximately 24 devices from each wafer. Figure 4.24 shows the photocurrent measured for those devices while illuminated with 1310 nm wavelength light and operated at a temperature of 77 K. The supercontinuum laser source (SuperK EXTREME EXW-6, NKT Photonics) was used to provide the infrared radiation.

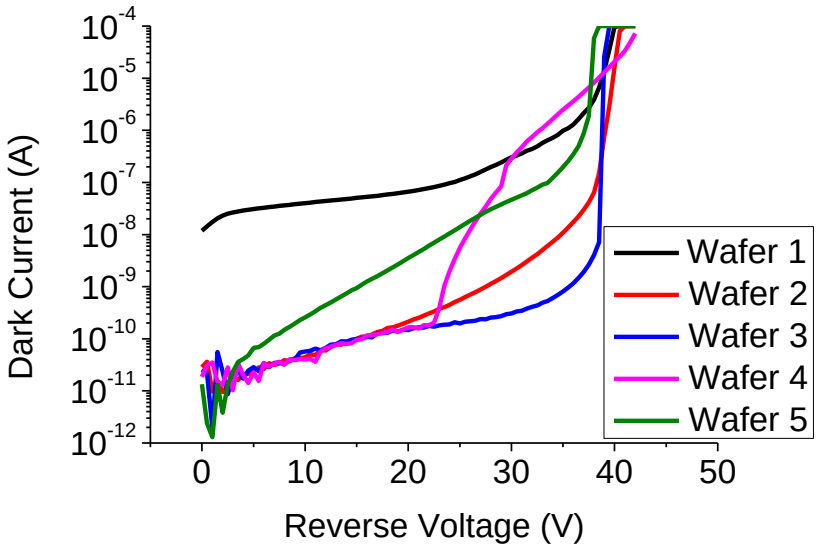

Figure 4.23. Dark current as a function of reverse bias of 100 μm diameter SPADs fabricated from different charge sheet doping concentration wafers: 1×10^{17} cm^{-3} (black), 2×10^{17} cm^{-3} (red), 3×10^{17} cm^{-3} (blue), 4×10^{17} cm^{-3} (magenta), and 5×10^{17} cm^{-3} (green). All the detectors were operated at a temperature of 77 K.

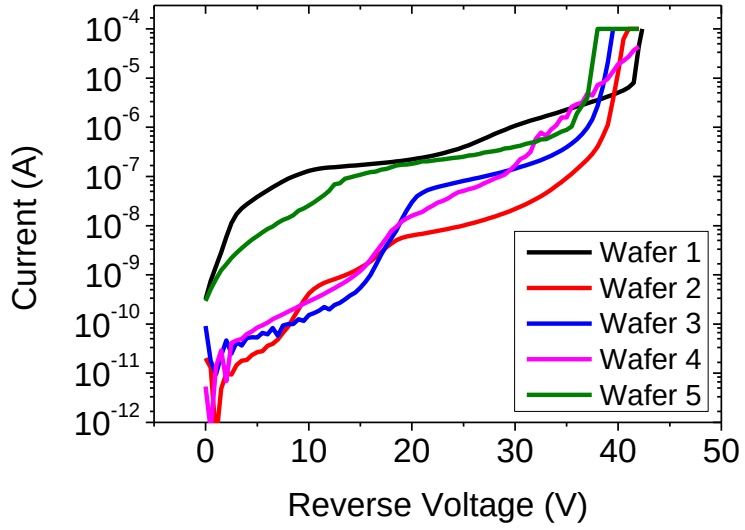

Figure 4.24. The current-voltage characteristics of typical 100 μm diameter Ge-on-Si SPAD detectors made using different charge sheet doping concentration wafers: 1×10^{17} cm^{-3} (black), 2×10^{17} cm^{-3} (red), 3×10^{17} cm^{-3} (blue), 4×10^{17} cm^{-3} (magenta), and 5×10^{17} cm^{-3} (green). All the detectors were operated at a temperature of 77 K and illuminated with 1310 nm wavelength light.

A brief summary of the main findings determined from the current-voltage characterisation is presented in the Table 4.2. The photocurrent measurements were performed to determine the punch-through and the breakdown voltage for typical 100 μm diameter Ge-on-Si SPADs operated at a temperature of 77 K for each wafer. Punch-through occurs when the electric field extends into the absorption region, allowing the photogenerated electrons to drift into the multiplication region. In Figure 4.24, it can be observed for each I-V, as the voltage is increased, a point of inflexion can be seen in the curve as the Ge absorber is depleted. The voltage at which punchthrough occurs will depend strongly on the charge sheet doping and thickness. Over the temperature used in these measurements (i.e. between 77 K and 300 K), the punchthrough voltage will not change as the doping densities will not vary significantly in this range. The avalanche breakdown voltage, on the other hand, will vary significantly with temperature as phonon collisions reduce the kinetic energy of drifting carriers. Hence, the lower temperatures will reduce the likelihood of phonon collisions, reducing the field required for breakdown as the temperature is decreased. In Figure 4.24, the breakdown voltage can be observed as the current rapidly increases by orders of magnitude with a small increase in applied reverse bias. The difference between the punch-through and the breakdown voltage is particularly important when operating the detectors at cryogenic temperatures. If the difference was small at room temperature, then the device might reach breakdown before punch-through has occurred at lower temperature. This would significantly reduce the detection efficiency since photogenerated electrons will not drift into the multiplication region.

Table 4.2. Summary of the measured punch-through and breakdown voltages for the measured wafers. The 100 μm diameter Ge-on-Si SPADs were illuminated with 1310 nm wavelength light while operated at 77 K.

Nominal charge sheet doping concentrations (cm^{-3})	Punch-through voltage (V)	Breakdown voltage (V)
1×10^{17}	~ 12	40.9
2×10^{17}	~ 19	39.9
3×10^{17}	~ 20	38.3
4×10^{17}	~ 20	--
5×10^{17}	~ 14	37.3

Unfortunately, it was impossible to determine the breakdown voltage for the Wafer 4 (charge sheet doping density of 4×10^{17} cm^{-3}) SPADs. The current reached the compliance limit (100 μA) before the breakdown was apparent. The devices fabricated from the Wafer 3 showed the lowest dark current at voltages just before avalanche breakdown, as illustrated in Figure 4.23, making it the most likely candidate design for single-photon detection operation. Wafer 3 had a nominal charge sheet doping concentration of 3×10^{17} cm^{-3} and all the further devices described in this Thesis were fabricated from this wafer.

In the next section, we will describe a performance investigation of the proposed three designs described earlier. A partially etched mesa design with exposed sidewalls, as shown in Figure 4.6, was also fabricated and used as a control sample during characterisation. For these designs, the charge sheet diameters ranged from 26 μm to 200 μm. Unfortunately, the fabrication yield for small devices was very low due to planarization issues affecting the top metal contact. Thus our device characterisation concentrated only on large cross sectional area detectors (100 μm and 200 μm) compared to previous studies of Ge-on-Si SPADs configured in alternative geometries [1, 4]. Future SPADs will be significantly smaller than this, for example with diameters of around 10 μm in order to further reduce the dark count rates.

4.6 Optical characterisation of proposed design devices

4.6.1 Dark IV characteristics for all design devices

All the SPAD structures fabricated from the Wafer 3 were characterised at a temperature of 78 K. Figure 4.25 illustrates the dark current measured for all SPAD structures. The partially etched mesa structure fabricated had a similar microstructure to the planar geometry of Design 3, except that an etch process was used to create a mesa of a diameter equal to the top contact diameter etched to a depth just below the charge sheet and into the multiplication layer.

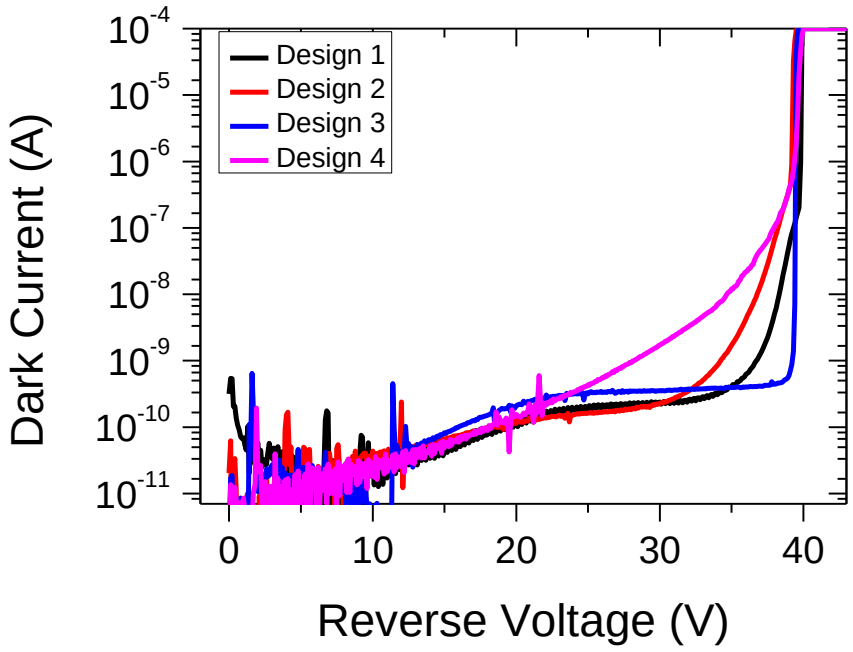

Figure 4.25. Typical dark current of the four different designs 100 μm diameter Ge-on-Si SPADs operated at 78 K as a function of reverse bias.

The Design 3 SPAD has a sharp breakdown indicating a low multiplied dark current, previously found to be a strong indicator of the desired low dark count rate performance [18]. The Design 4 SPAD has a much softer breakdown with a dark current 50 fold times higher than the planar structure immediately before breakdown. This indicates that, as expected, significant surface generation is present and suggests that it will have high dark count rates compared to the planar SPAD. Indeed, it was not possible to characterise the Design 4 SPAD above breakdown due to its prohibitively high DCR. Although the dark I-Vs of Designs 1 and 2 SPADs were sharper than the I-V of Design 4 SPADs, these devices also had significantly high multiplied dark current before the breakdown as shown in Figure 4.25. From here on, Design 4, the partially etched mesa structure will be referred to as the mesa geometry SPAD and Design 3 as the planar geometry SPAD respectively.

4.6.2 Photocurrent measured using a planar Ge-on-Si SPAD operated at 78 K under 1310 nm wavelength illumination

Figure 4.26 demonstrates the dark current and photocurrent of the planar SPAD as a function of reverse bias at 78 K. The dark current before breakdown is less than 1 nA and the SPADs exhibited good uniformity, with less than an order of magnitude variation in dark current between devices.

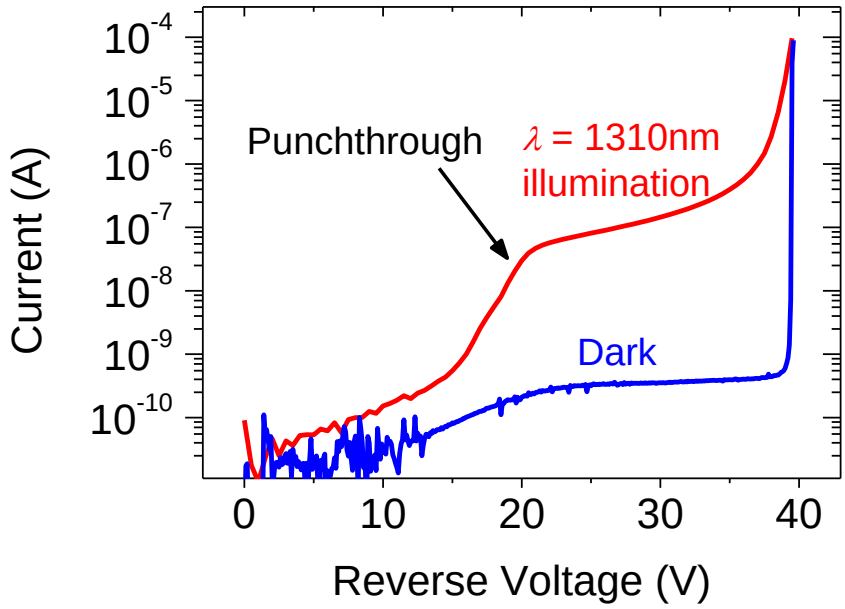

Figure 4.26. The dark current (blue line) and photocurrent (red line) of the planar SPAD as a function of reverse bias at 78 K.

Photocurrent measurements at λ = 1310 nm demonstrate clear punch-through at 20 V. The device yield for this design was over 90%, which at this early stage, is very encouraging for the eventual realisation of Ge-on-Si SPAD focal plane arrays.

4.7 Conclusions

Ge-on-Si SPAD detectors have been designed, simulated, fabricated and characterised. These detectors possess the advantages of compatibility with mature Si technology while expanding the wavelength of operation beyond sensitivity of Si-based SPADs up to 1550 nm. The design was based upon the SACM structure with critical modifications to confine the high electric field away from the exposed sidewalls to eliminate the deleterious contribution of the defects and dislocations to DCR. Firstly, three different planar geometry designs have been developed. The modelling revealed that by reducing the diameter of the implanted Ge p^{++} top contact layer with respect to the implanted Si charge sheet layer the electric field was confined along the centre of the detector. These designs were fabricated using ion beam implantation and regrowth, which added to the complexity of the fabrication process when compared to a mesa geometry process. Initial measurements indicated that there is a conductive path formed by the background doping level found in the Ge layer. Therefore, a "superpixel" was formed around the device in order to provide electrical isolation. The minimum distance between the sidewall and the

charge sheet was found to be 5 μm using Silvaco simulating software. Other methods to improve the device performance were also considered, such as increasing the thickness of the Ge absorption layer. It has been estimated that in the most promising design, the 1um thickness Ge layer absorbs only less than 50% of incident radiation at 1310 nm wavelength. Therefore, structures with 2 μm and 3 μm thick absorption region have been proposed and simulated. The modelling has revealed that the distance between the sidewall and the charge sheet layer would need to increase as well. However, further experimental investigation is required to determine the exact effect this distance has on the device performance. It should noted that this distance would directly affect the fill factor of the future Ge-on-Si SPAD arrays, in a similar manner to the implementation of guard rings in all-Si based planar SPAD structures.

Five different structures with varying the charge sheet doping concentration between 1×10^{17} cm^{-3} and 5×10^{17} cm^{-3} were grown by a commercial supplier IQE. Preliminary measurements of partially etched structures revealed that the wafer with 3×10^{17} cm^{-3} charge sheet doping concentration was identified as having most promising results in terms of the punch-through and breakdown voltage. Hence, all the further detectors have been fabricated from this wafer.

The preliminary optical characterisation of the three proposed designs confirmed that the best performance is achieved using the detector with the reduced diameter compared to the diameter of the charge sheet, as predicted by the simulation. Evidently, SPADs of that design showed the lowest dark current level immediately before the breakdown. Also, those devices demonstrated a clear punch-through at 20 V. Partially etched mesa devices showed 50 times higher dark current under the same conditions. The yield for the smaller devices was very low and all results presented in this Chapter were obtained by characterising 100 μm diameter SPADs. Further improvement of the planarization is required in order to reduce the detector diameter down to 25 μm - 10 μm, which would further improve the device performance.

Results in this Chapter generally showed agreement between simulation and experimental results, in terms of both charge sheet doping and superpixel geometry. Whilst the results on small diameter devices were poor - due to top contact issues - we obtained single-photon detection performance and high yield from the larger area devices. The smaller area devices required considerable development of planarization processes, in order to reach acceptable yield and performance. The larger 100 μm diameter devices exhibited

excellent current-voltage characteristics when compared to previous mesa geometry devices, and indicative of high single-photon detection performance. In the next Chapter, single-photon characterisation is performed on these devices in order to benchmark their performance and inform later device iteration stages.

4.8. Acknowledgments

Fabrication of the Ge-on-Si SPAD detectors described in this Chapter have been performed by our colleagues form the University of Glasgow. The planar geometry Ge-on-Si SPAD detector design (Figure 4.5), electric field diagrams corresponding to the planar geometry design and a partially etched mesa design (Figures 4.9 and 4.10) and photocurrent and dark current of the planar geometry Ge-on-Si SPADs as a function of the reverse bias at a temperature of 78 K (Figure 4.26) presented in this Chapter have been reported in Ref. [14].

4.9 References

1. R.E. Warburton, G. Intermite, M. Myronov, P. Allred, D.R. Leadley, K. Gallacher, D.J. Paul, N.J. Pilgrim, L.J.M. Lever, Z. Ikonic, R.W. Kelsall, E. Huante-Ceron, A.P. Knights, and G.S. Buller, *Ge-on-Si Single-Photon Avalanche Diode Detectors: Design, Modeling, Fabrication, and Characterization at Wavelengths 1310 and 1550 nm.* IEEE Transactions on Electron Devices, 2013. **60**(11): p. 3807-3813.

2. M.S. Carroll, K. Childs, R. Jarecki, T. Bauer and K. Saiz, *Ge–Si separate absorption and multiplication avalanche photodiode for Geiger mode single photon detection.* Applied Physics Letters, 2008. **93**(18): p. 183511.

3. C.T. DeRose, D.C. Trotter, W.A. Zortman, A.L. Starbuck, M. Fisher, M.R. Watts, and P.S. Davids, *Ultra compact 45 GHz CMOS compatible Germanium waveguide photodiode with low dark current.* Optics Express, 2011. **19**(25): p. 24897-24904.

4. Z. Lu, Y. Kang, C. Hu, Q. Zhou, H.-D. Liu, and J.C. Campbell, *Geiger-Mode Operation of Ge-on-Si Avalanche Photodiodes.* IEEE Journal of Quantum Electronics, 2011. **47**(5): p. 731-735.

5. N.J. Martinez, C.T. Derose, R.W. Brock, A.L. Starbuck, A.T. Pomerene, A.L. Lentine, D.C. Trotter, and P.S. Davids, *High performance waveguide-coupled Ge-on-Si linear mode avalanche photodiodes.* Optics Express, 2016. **24**(17): p. 19072-81.

6. M.A. Itzler, R. Ben-Michael, C.-F. Hsu, K. Slomkowski, A. Tosi, S. Cova, F. Zappa, and R. Ispasoiu, *Single photon avalanche diodes (SPADs) for 1.5 μ m photon counting applications.* Journal of Modern Optics, 2007. **54**(2-3): p. 283-304.

7. S.M. Sze and K.K. Ng, *Physics of semiconductor devices*. 2006: John Wiley & Sons.

8. N. DiLello, D. Johnstone and J. Hoyt, *Characterization of dark current in Ge-on-Si photodiodes.* Journal of Applied Physics, 2012. **112**(5): p. 054506.

9. J.C. Campbell, *Recent advances in telecommunications avalanche photodiodes.* Journal of Lightwave Technology, 2007. **25**(1): p. 109-121.

10. S. Cova, M. Ghioni, A. Lotito, I. Rech and F. Zappa, *Evolution and prospects for single-photon avalanche diodes and quenching circuits.* Journal of Modern Optics, 2004. **51**(9-10): p. 1267-1288.

11. R.H. Hadfield, *Single-photon detectors for optical quantum information applications.* Nature Photonics, 2009. **3**(12): p. 696.

12. P. Webb, R. McIntyre, J. Scheibling and M. Holunga. *A planar InGaAs APD fabricated using Si implantation and regrowth techniques*. in *Tech. Dig. Opt. Fiber Conf*. 1988.

13. S. Pellegrini, R.E. Warburton, L.J. Tan, J.S. Ng, A.B. Krysa, K. Groom, J.P. David, S. Cova, M.J. Robertson, and G.S. Buller, *Design and performance of an InGaAs-InP single-photon avalanche diode detector.* IEEE Journal of Quantum Electronics, 2006. **42**(4): p. 397-403.

14. P. Vines, K. Kuzmenko, J. Kirdoda, D.C. Dumas, M.M. Mirza, R.W. Millar, D.J. Paul, and G.S. Buller, *High performance planar germanium-on-silicon single-photon avalanche diode detectors.* Nature Communications, 2019. **10**(1): p. 1086.

15. ATLAS User's Manual, *Device simulation software.* Silvaco Int., Santa Clara, CA, 2008.

16. S. Sze and G. Gibbons, *Effect of junction curvature on breakdown voltage in semiconductors.* Solid-State Electronics, 1966. **9**(9): p. 831-845.

17. W. Dash and R. Newman, *Intrinsic optical absorption in single-crystal germanium and silicon at 77 K and 300 K.* Physical Review, 1955. **99**(4): p. 1151.

18. E.A. Webster and R.K. Henderson, *A TCAD and spectroscopy study of dark count mechanisms in single-photon avalanche diodes.* IEEE Transactions on Electron Devices, 2013. **60**(12): p. 4014-4019.

Chapter 5. Single-photon detection characterisation of the planar Ge-on-Si SPAD detectors

5.1 Introduction

The previous chapter examined the design, fabrication and the preliminary characterisation of the planar geometry Ge-on-Si SPADs. In this Chapter, a characterisation study of these detectors in terms of the key performance parameters: detector dark count rate (DCR); single-photon detection efficiency (SPDE); noise-equivalent power (NEP); and jitter is presented. Such performance data are vital to determine whether a detector satisfies the requirements of different photon counting applications such as quantum communications applications [1-3], ranging measurements and terrestrial mapping for defence applications [4, 5], LIDAR and three-dimensional imaging [6-8] including underwater imaging [9, 10].

Measurements of the SPDE at a detection wavelength of 1310 nm and the DCR as a function of excess bias at temperatures of 78 K, 100 K and 125 K are then presented in this Chapter for 100 µm diameter planar Ge-on-Si SPAD detectors. In these measurements, an electrical gating approach was used to switch the detector to above avalanche breakdown, into the Geiger mode, in synchronisation with the arrival of the attenuated laser pulse. This gated detector approach was used at low frequencies of 10 kHz and 1 kHz at a temperature of 78 K in order to fully quench the avalanche and avoid any effects of afterpulsing (described below). It will be demonstrated that these detectors exhibited considerably lower DCR with reduced device area, as previously reported in all-Si SPADs [11]. The SPDE as a function of the wavelength of incident radiation will be presented for various operating temperatures up to 175 K to investigate the spectral range of operation of this detector.

An afterpulsing study is then presented of the Ge-on-Si SPADs. Firstly, a short discussion of the afterpulsing phenomenon in SPAD detectors will be presented. Then, a description of the methodology and the experimental set-up used to study the afterpulsing in Ge-on-Si SPADs is described. Then, the afterpulsing results are presented and compared against

measurements of a 25 µm diameter commercially available InGaAs/InP SPAD under identical operating conditions.

The most recent results, the SPDE at a detection wavelength of 1310 nm, the DCR, NEP and timing jitter, obtained using 26 µm diameter planar Ge-on-Si SPAD detectors will be presented at the end of this Chapter.

5.2 Experimental set-up and methodology

The schematic of the set-up used for single-photon characterisation is shown in Figure 5.1. SPDE, DCR and jitter measurements were performed using the TCSPC technique. The SPAD detector was mounted inside an Oxford Instruments liquid nitrogen cryostat, which enables measurements between 78 K and 400 K. The cryostat has optical access, which allowed a short working distance of 30.5 mm between the detector and the external optical system. Picosecond pulsed lasers were used to measure the SPDE of the SPAD, with the output attenuated to a level of less than 0.1 photon per pulse in order to reduce the probability of a single pulse containing more than one photon and to demonstrate true single-photon counting. Two lasers were used – a PicoQuant laser diode emitting a wavelength of 1310 nm as well as NKT Supercontinuum laser source tuneable in the SWIR region. The laser outputs were coupled into single mode fibres (SMF-28) and then to a 50:50 fibre splitter. One splitter output was connected to a calibrated power meter to provide in-situ power readings, which were continuously monitored during the measurements. The other splitter output was connected to a calibrated, programmable optical attenuator where it could be attenuated by up to 100 dB. This attenuator output was inserted into a reflective collimator for free space collimation. The collimated beam passed through two pellicle beamsplitters (92:8 splitting ratio), which allowed a broadband illumination channel and an imaging channel to a SWIR camera used to align and focus the laser spot onto the detector.

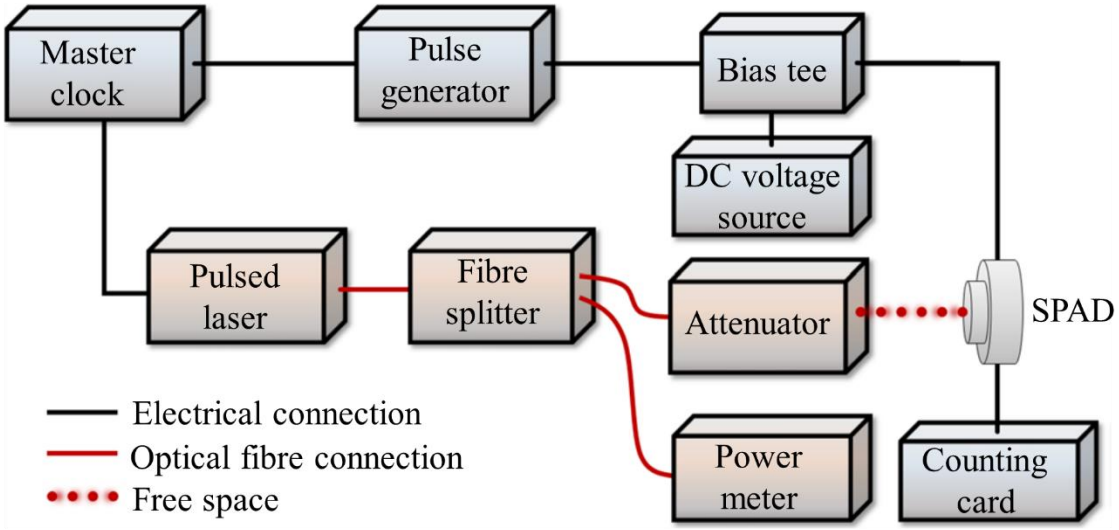

Figure 5.1. Schematic diagram of the experimental set up used for single-photon characterisation. SWIR light attenuated by a programmable optical attenuator was focused onto the planar Ge-on-Si SPAD. The detector was situated inside an Oxford Instruments liquid nitrogen cryostat. A pulse pattern generator provided the gate pulse to bring the SPAD above the breakdown voltage. An Edinburgh Instruments TCC900 photon counting card was used for data acquisition. From Ref. [12].

Prior to each SPDE measurement, the laser power reaching the SPAD was measured using a calibrated optical power meter and compared to the power measured by the in-situ power meter. This ratio was used to calculate the number of photons per pulse incident upon the SPAD for a given power meter reading. The number of photons per pulse N was calculated as:

$$N = P/h\nu F, \tag{5.1}$$

where P is the optical power incident on the device, F is the laser repetition rate, ν is the frequency of the illumination source, and h is Planck's constant. The devices were operated in gated mode with a DC source biasing the SPAD at, typically, 1.3 V below the breakdown voltage. An AC pulse or the detector gate was combined with the DC bias using a Tektronix 5530 Bias Tee, with the output connected to the anode of the detector biasing the detector above the breakdown voltage. A detector gate of 50 ns duration was used in the experiments described in this Chapter. The SPAD output was connected to the Edinburgh Instruments TCC900 photon counting card STOP signal. A master clock

controlled the timing of the laser trigger, the detector gate and the start signal for the photon counting card. The detectors were characterised at different levels of excess biases above breakdown voltage V_{Bd}. The excess bias can be expressed as:

$$Excess\ bias = \frac{(V_{DC}+V_{AC})-V_{Bd}}{V_{bd}} \times 100\%, \quad (5.2)$$

where V_{DC} and V_{AC} are the amplitude of the DC and AC signal applied to the detector. All the measurements were performed in a dark laboratory environment which allowed us to treat the effect of background illumination as being negligible.

5.3 Single-photon detection efficiency and dark count rate of the planar Ge-on-Si SPADs operated at temperatures between 78 K and 125 K

This section presents the experimental results of the single-photon characterisation of the planar geometry Ge-on-Si SPADs operated at cryogenic temperatures between 78 K and 175 K. As discussed in Chapters 2 and 4, there are several mechanisms that generate dark counts, including thermally generated carriers that trigger avalanche events, carriers generated by interband tunnelling, and carriers released from traps populated in a previous avalanche [13, 14]. The DCR is defined as the average number of dark counts per second. In a detector gated configuration, this means that the DCR is normalised to a value corresponding to the detector being activated constantly. In gating mode, the DCR can be calculated from:

$$DCR = N_{dark} / F \cdot t \cdot \tau, \quad (5.3)$$

where N_{dark} is a number of dark counts, F is the laser repetition rate, t is the acquisition time of the measurement, and τ is a time interval within the gate. As illustrated in Figure 5.2, although the detector gate width is 50 ns, only a smaller time interval τ is considered for DCR and SPDE calculations. The AC pulse that is used to bring the SPAD above the breakdown has ~ 10 ns leading and falling edge. Therefore, the detector is fully biased for a shorter time interval of ~ 30 ns. For all the calculations in this Thesis we have considered time intervals within the gate where the detector was evidently fully biased.

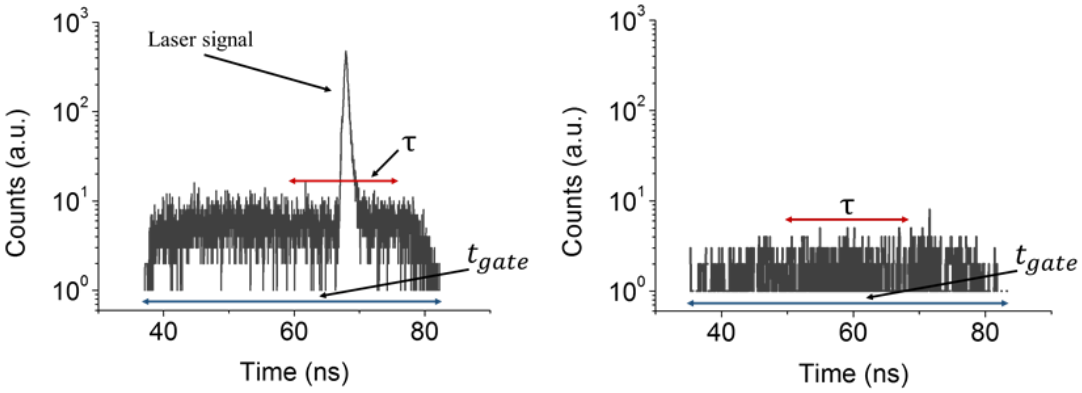

Laser detection measurement Dark count measurement

Figure 5.2. An illustration of the example histograms of the laser detection measurement (left) and the dark count rate measurement (right). The detector gate is 50 ns. However, SPDE and DCR calculations consider a smaller integration time interval τ inside the gate.

As mentioned in Chapter 2, the SPDE in a separate-absorption and multiplication SPAD, such as the Ge-on-Si SPADs described in this Chapter, will depend on three main parameters: the absorption of incident photons within the absorber layer of the semiconductor, the transport of carriers to the multiplication region and the triggering probability of carriers within the multiplication region. The probability of triggering the avalanche is strongly dependent on the excess bias, the carrier impact ionisation coefficients and the absorption depth of an incident photon. The SPDE characterisation presented in this Thesis have been determined experimentally using the following equation:

$$SPDE = (N_{total} - N_{dark})/N_{ph} \cdot t \cdot F \tag{5.4}$$

where N_{total} is the total number of counts in the histogram peak, N_{ph} is the number of incident photons. Figures 5.3, 5.4 and 5.5 show the DCR and SPDE as a function of excess bias of the 100 μm planar Ge-on-Si SPADs operated at 78 K, 100 K and 125 K, respectively.

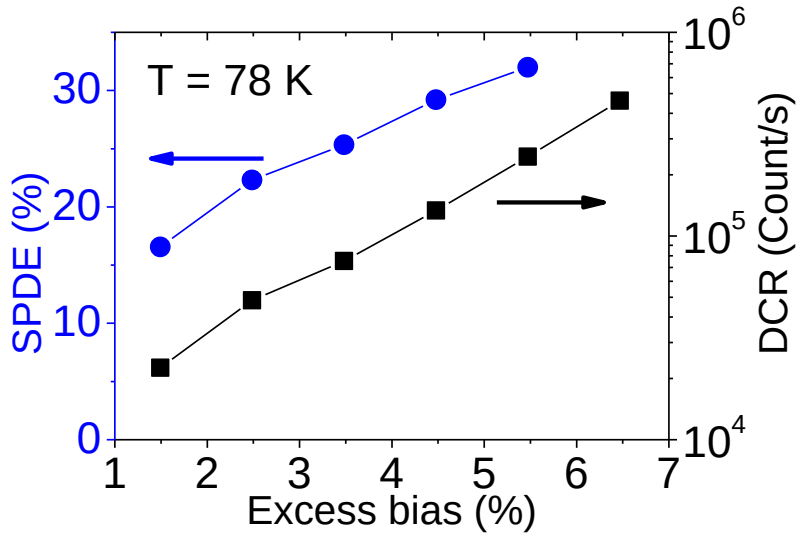

Figure 5.3. SPDE and DCR of the 100 μm diameter planar Ge-on-Si SPADs operated at a temperature of 78 K as a function of the excess bias.

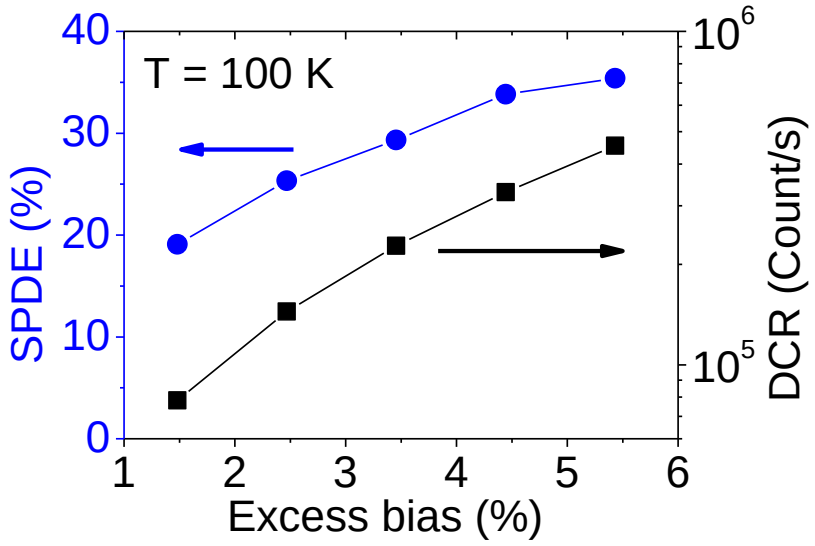

Figure 5.4. SPDE and DCR of the 100 μm diameter planar Ge-on-Si SPADs operated at a temperature of 100 K as a function of the excess bias.

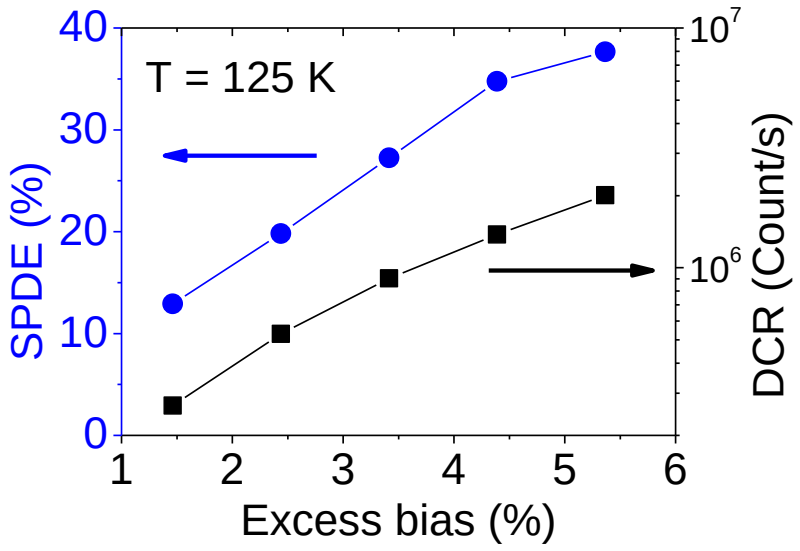

Figure 5.5. SPDE and DCR of the 100 μm diameter planar Ge-on-Si SPADs operated at a temperature of 125 K as a function of the excess bias.

We have measured a maximum SPDE of 38% at a temperature of 125 K and excess bias of 5.5% whilst the detector exhibited DCR of 2 Mcount s^{-1}. The lowest DCR measured was 22.5 kcount s^{-1} with corresponding SPDE of 16.5% at an operating temperature of 78 K and excess bias of 1.5%. It is evident from the Figures 5.3 – 5.5 that SPDE and DCR increase with the excess bias and the temperature. The measured DCR demonstrates a vast improvement when compared to previous Ge-on-Si SPAD work. For example, a mesa geometry Ge-on-Si SPAD developed previously by our group was reported to exhibit a DCR of 5.5 M count s^{-1} for a 25 µm diameter SPAD at a temperature of 100 K [15]. This corresponded to 11.2 k count $s^{-1}µm^{-2}$, which is approximately three orders of magnitude higher than the 18.3 count $s^{-1}µm^{-2}$ reported here. It should also be noted that, under these conditions, the SPDE reported for the mesa device in [15] was 4%, compared to 26% for the SPADs presented here. There is a similar relationship when our results are compared to results from a waveguide-coupled device reported by *Martinez et al* [16] in which the reported DCR was 500 kcount s^{-1} for a 1 µm × 15.9 µm rectangular waveguide SPAD at a temperature of 80 K. This corresponds to 31.4 kcount $s^{-1}µm^{-2}$, which is over three orders of magnitude higher than 6.37 count $s^{-1}µm^{-2}$ for the SPADs presented here. *Martinez et al* [18] reported an SPDE of 5% while the SPADs presented here have an SPDE of 22%. This considerable reduction in DCR has resulted from the carefully designed electric field profile of these planar geometry detectors, which means that the high electric field is confined within the SPAD, preventing surface states

contributing significantly to the DCR as described in Chapter 4. Most dark counts in these SPADs are now likely to originate from dislocations arising at the Si/Ge interface and from thermal excitation throughout the volume of the device.

Figure 5.5 demonstrates that the SPDE increases with excess bias to a maximum of 38% at 125 K, significantly higher than previous SPDEs reported for Ge and Ge-on-Si SPADs [15-18] and comparable to the highest values recorded for InGaAs/InP SPADs at 225 K [19-21]. This is due in part to the higher excess biases applied across the SPAD, attainable due to the low DCR compared with previous Ge-on-Si devices, increasing the breakdown probability in the multiplication region. In addition, the relatively thick 1.5 µm Si multiplication region further increases the breakdown probability, the likelihood of a self-sustaining avalanche on arrival of the primary electron. The uniform electric field in the multiplication region, as demonstrated in Chapter 4, caused by minimal residual doping in the lower part of the Si multiplication layer, results in a uniform impact ionisation rate throughout, increasing the breakdown probability still further. The optimised electric field also ensures the efficient transit of photo-excited electrons into the multiplication region. Significantly, there is no conduction band energy barrier between the Ge absorption region and the Si charge sheet, which ensures photo-excited electrons, can easily pass between the two regions. Indeed the Si Δ-valley of the conduction band edge is 235 meV below the Ge L-valley conduction band edge in the absorber as calculated by our collaborators using the deformation potentials [22]. This is an advantage over InGaAs/InP SPADs which possess an energy barrier step in the valance band that photoexcited holes must overcome to reach the InP multiplication region. InGaAs/InP SPADs require an InGaAsP grading layer between the InGaAs and InP regions to reduce carrier accumulation at the absorber-charge sheet interface [23]. For Ge-on-Si SPADs, the absence of a conduction band offset creating a barrier at the Ge/Si hetero-interface should ensure that the SPDE remains high at temperatures in future design iterations. Finally, the anti-reflective coating that have been used for Ge-on-Si SPADs reduced reflection from the top surface of the SPAD to less than 1% of the incident radiation. With these device samples, measurements at higher temperatures were limited by the increasing DCR due to increasing thermal generation rates. However, a further reduction in DCR of the future detectors is likely to allow a significantly higher operating temperature.

The high SPDE has been achieved despite the use of a relatively thin Ge absorption region. As mentioned in Chapter 4, less than 50% of the 1310 nm wavelength radiation is absorbed in 1 µm thick Ge absorber throughout the operational temperature range. According to this calculation, a 2 µm thick Ge absorber will increase the absorption to ~70%, which should lead to an SPDE of greater than 55% at 125 K. This figure is significantly higher than reported SPDEs for InGaAs/InP SPADs [19-21]. Even thicker Ge layers should provide higher absorption still and future examination of 2 µm and 3 µm Ge absorbers is planned for future work.

5.4 Noise equivalent power

Noise equivalent power (NEP) is a figure of merit for SPADs calculated from the SPDE and DCR of the detector using the following equation:

$$NEP = \frac{h\nu}{SPDE}\sqrt{2DCR} \tag{5.5}$$

where h is Planck's constant and ν is the frequency of the incident radiation. It represents the lowest measurable optical power within 1 s acquisition time. This can be used to compare detectors, with lower values indicating improved performance. At 78 K we have calculated a record low NEP for a Ge-on-Si SPAD of 1.9×10^{-16} W $Hz^{-1/2}$, a fifty-fold improvement, when compared to the best previously reported NEP of the Ge-on-Si SPAD [15]. NEP values of 3×10^{-16} $WHz^{-1/2}$ and 7×10^{-16} $WHz^{-1/2}$ were calculated for temperatures of 100 K and 125 K.

5.5 Timing jitter

Figure 5.6 shows a timing histogram taken using the planar Ge-on-Si SPADs at an excess bias of 5.5% operated at a temperature of 78 K and illuminated with 1310 nm wavelength light. Timing histograms with a timing bin width of 19.5 ps recorded by the photon counting card were used to calculate the device jitter. The jitter is defined as the full-width-at-half maximum (FWHM) of the histogram and was found to be 310 ps. This value is reasonable considering the device diameter and the width of the multiplication layer. It is expected that smaller active area devices will demonstrate significantly reduced jitter [23, 24]. Wider multiplication regions generally improve the SPDE but the increased variance in the avalanche build-up time increases the jitter. [23, 25].

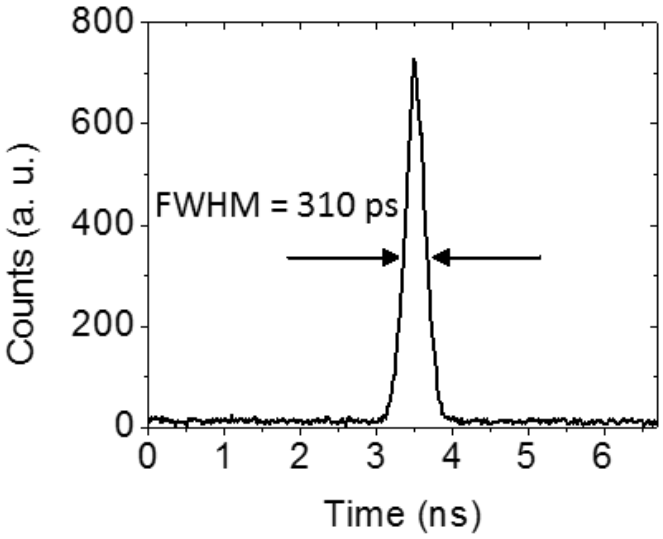

Figure 5.6. Timing histograms measured using the 100 µm diameter planar Ge-on-Si SPAD at an excess bias of 5.5% operated at a temperature of 78 K and illuminated with 1310 nm wavelength radiation. The FWHM jitter is 310 ps. From Ref. [12].

It is expected that the jitter will reduce as the device diameter is decreased, as found previously in Si SPADs [24], and by improving the electronic packaging of the cooled device.

5.6 Wavelength dependence of the Ge-on-Si SPAD detector efficiency

This section presents an experimental investigation of the wavelength dependence of the planar Ge-on-Si SPAD detector efficiency varying the temperature of operation. It is expected that SPDE at longer wavelengths of operation will vary with temperature as the Ge band-gap changes with temperature. However, it has been demonstrated in the past that absorption wavelength of Ge-on-Si photodetectors is greater than that of bulk Ge due to strain introduced by the lattice mismatch between Ge and Si [26]. Therefore, experimental investigation was required to establish the limitations of our Ge-on-Si SPAD detectors.

Figure 5.7 demonstrates the wavelength dependence of the SPDE as a function of temperature. The high efficiency SPDE region is related to direct bandgap absorption between the conduction band and the valence bands at the Γ-point as mentioned in Chapter 3. Absorption at longer wavelengths is related to significantly weaker indirect

absorption into the L-valleys and the valence bands. At room temperature the direct bandgap of Ge is 0.80 eV which corresponds to 1550 nm wavelength [22] but this increases to 0.88 eV at 78 K, reducing the detection cut-off wavelength to 1410 nm [22]. Using the NKT Supercontinuum tunable laser source described previously, we were able to vary the wavelength of the radiation incident on the SPAD from 1310 nm to 1550 nm to obtain accurate cut-off wavelengths at various temperatures. We define the cut-off wavelength, λ_c, as the wavelength at which the detector's SPDE is 50% of the 1450 nm wavelength value. It can be extracted from Figure 5.7 that λ_c increases from 1468 nm at 125 K to 1495 nm at 175 K, increasing at a rate of approximately 0.54 nm/K.

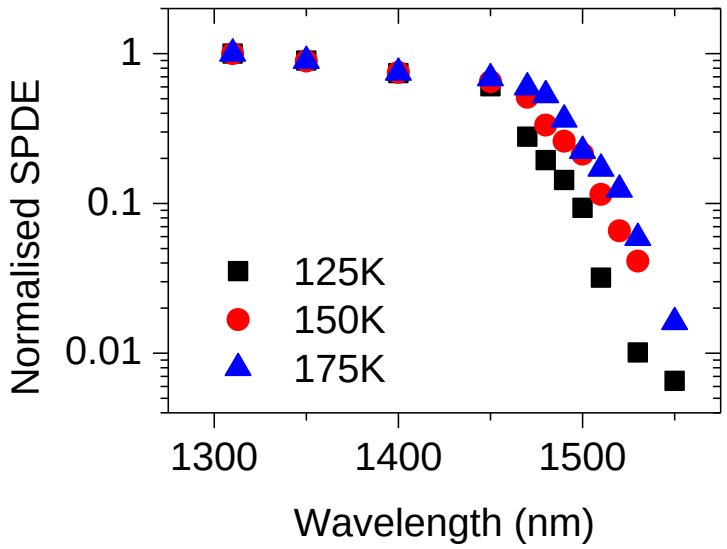

Figure 5.7. Normalised SPDE as a function of incident wavelength for a 100 µm diameter SPAD at temperatures of 125 K (black squares), 150 K (red circles) and 175 K (blue triangles). From Ref. [12].

Indeed, we have found that experimentally established cut-off wavelength was approximately 42 nm greater than theoretically calculated using the temperature dependence of semiconductor band gaps according to Varshni [27]. Equation 5.6 describes the temperature dependant bandgap relation.

$$E_g(T) = E_0 - \alpha T^2/(T + \beta), \tag{5.6}$$

where T is the temperature; E_g is the temperature dependent energy bandgap; E_0 is the Ge energy bandgap at T = 0 K; α = 5.82 × 10^{-4} (eV/K), β =296 K are the model parameters for Ge direct bandgap [27]. After adjusting the model according to the

experimental results, we have estimated that efficient operation at 1550 nm wavelength could be achieved at 245 K using the Ge-on-Si with 1 μm thick absorber. It is expected that this can be achieved at even lower temperatures when a device with 2 μm absorber is used.

5.7 Afterpulsing in the planar Ge-on-Si SPADs

One critical difference between the Ge-on-Si SPADs and the InGaAs/InP SPAD alternative is a realistic potential of a significant reduction in the deleterious effects of detector afterpulsing. This phenomenon occurs when carriers are trapped after an avalanche event and then released later, resulting in an increased background level. Afterpulsing can be mitigated by using a long hold-off time (typically > 10 μs) after each event so that trapped carriers can be released prior to the detector being re-activated. This approach, however, increases the dead-time and restricts the maximum count rate possible. Afterpulsing is recognised as one of the main limitations of InGaAs/InP SPADs, severely affecting their performance, even at modest count rates. Afterpulsing in InGaAs/InP detectors originates mainly in the InP multiplication layer from deep level trap states [28-30], and the expectation with Ge-on-Si SPAD detectors is that the high-quality Si multiplication layer will have a lower density of such states. Here in this section, we will discuss the main findings of the afterpulsing study in planar geometry Ge-on-Si SPADs and show a comparison of afterpulsing in a commercially available InGaAs/InP SPAD with a planar Ge-on-Si SPAD under identical operating conditions. The latter exhibited 20% less afterpulsing at aforementioned 10 μs hold-off time.

5.7.1 Experimental set-up and methodology

Afterpulsing measurements have been performed on a 100 μm diameter planar Ge-on-Si SPAD operated at temperatures between 78 K and 175 K using the time-correlated carrier counting method [31]. This method is performed by creating a condition such that the SPAD undergoes an intentional avalanche. The device is then immediately quenched and then activated via an electrical gate for a second time shortly afterwards. By varying the time between the two detector gates, the probability of an avalanche in the second gate is examined, thus giving the afterpulsing probability as a function of time after the initial avalanche. The results obtained have been compared to a commercial state-of-the-art

InGaAs/InP SPAD operating at identical temperatures and applying specific excess biases to each detector in order to obtain an identical SPDE for both detectors.

5.7.2 Measured afterpulsing in Ge-on-Si planar SPADs

Figure 5.8 shows an example of the afterpulsing probability as a function of the time delay for the 100 μm diameter Ge-on-Si SPAD at 1.5% excess bias measured at different temperatures between 100 K and 175 K. It can be observed that the afterpulsing probability reduces as the temperature of operation is increased.

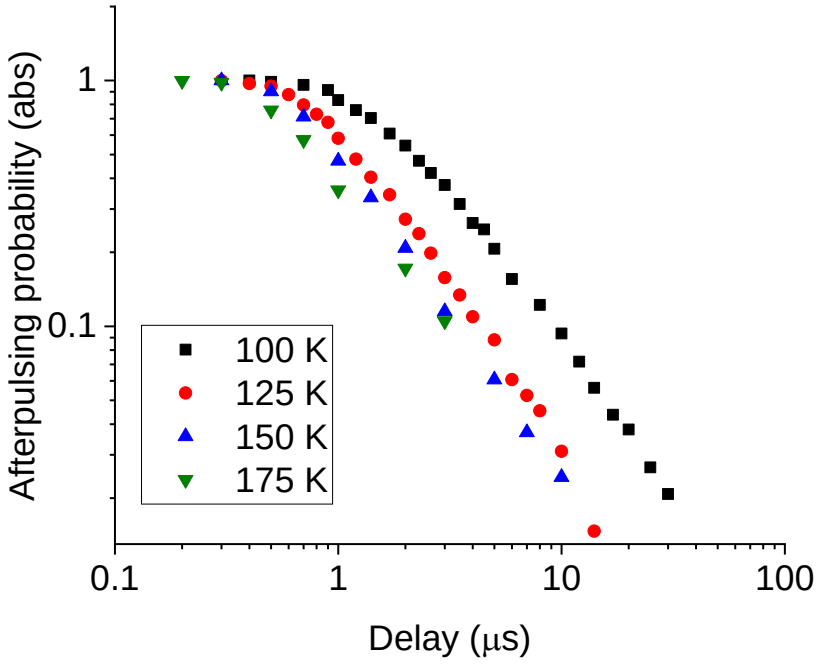

Figure 5.8. Example of an afterpulsing probability distribution measured using the 100 μm diameter Ge-on-Si SPAD at 1.5% excess bias operated at temperatures of 100 K (black squares), 125 K (red circles), 150 K (blue upwards triangles) and 175 K (green downwards triangles) as a function of the delay between two operating gates.

To investigate the afterpulsing mechanism in Ge-on-Si SPADs, we examined the afterpulse lifetime across a range of excess bias levels as a function of temperature between 78 K to 175 K, and fitted exponential decays. Figure 5.9 shows the Arrhenius plots of time constants extracted from the afterpulsing probability measurements for a range of excess biases. The emission rate of the trapped carriers can be expressed as:

$$\frac{1}{\sigma} \propto \exp\left(-\frac{E_a}{kT}\right), \tag{5.6}$$

where σ is the emission rate; E_a is the activation energy; T is the temperature; and k is Boltzmann's constant. Therefore, the gradient of the emission rate curve form the Figure 5.9 multiplied by $\ln(10)$ gives the activation energy E_a.

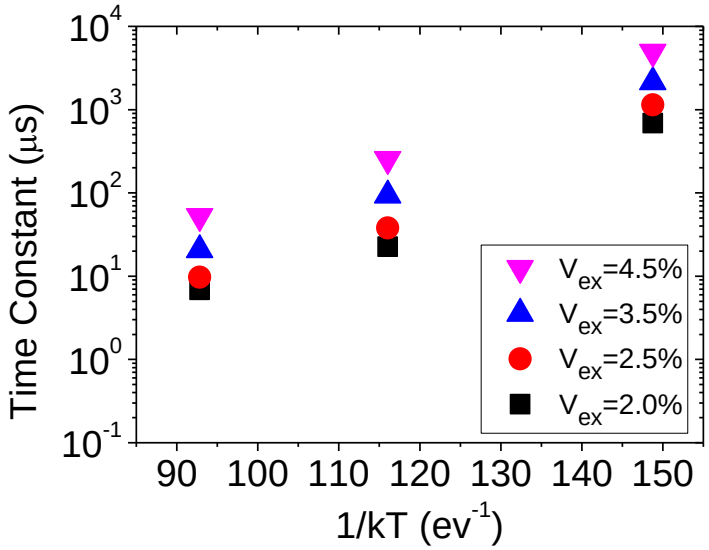

Figure 5.9. Time constants extracted from the Ge-on-Si SPAD afterpulsing probability as a function of $1/kT$ for excess biases of 2.0% (black squares), 2.5% (red circles), 3.5% (blue upwards triangles) and 4.5% (pink downwards triangles). From Ref. [12].

By fitting the Arrhenius plots, we have deduced the activation energies in the region of 80-90 meV across the range of excess bias levels to attempt to ascertain the origin of the traps. Figure 5.10 shows the activation energies for a range of excess biases between 2% and 4.5% extracted from the afterpulsing measurements data.

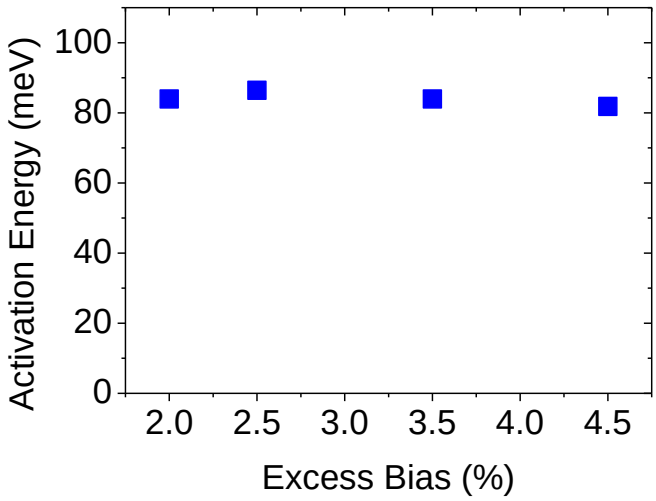

Figure 5.10. Activation energies for the planar Ge-on-Si SPAD as a function of excess bias from afterpulsing data. From Ref. [12].

Native Si surfaces, native Ge surfaces and GeO_x at Ge surfaces have been shown to have trap states close to 420 meV [32], 130 meV [32] and from 200 meV to 300 meV [33] respectively. This provides further evidence that the planar geometry reduced the effects of traps and other impurities at the exposed surfaces. Hence, the afterpulsing is unlikely to be related to surface states on the passivated Ge or any exposed Si surfaces.

5.7.3 Afterpulsing comparison between Ge-on-Si and commercial Princeton Lightwave InGaAs/InP SPAD

Figure 5.11 shows the variation in afterpulsing probability of the two SPADs at a temperature of 125 K and 150 K when applying excess biases corresponding to an SPDE of 17% in both detectors. It can be observed that for a specific hold-off time, the afterpulsing probability was significantly reduced for the Ge-on-Si SPAD. For instance, using a hold off time of 10 µs, the Ge-on-Si SPAD exhibited 20% of the afterpulsing probability of the InGaAs/InP SPAD detector. A similar trend was demonstrated at 150 K.

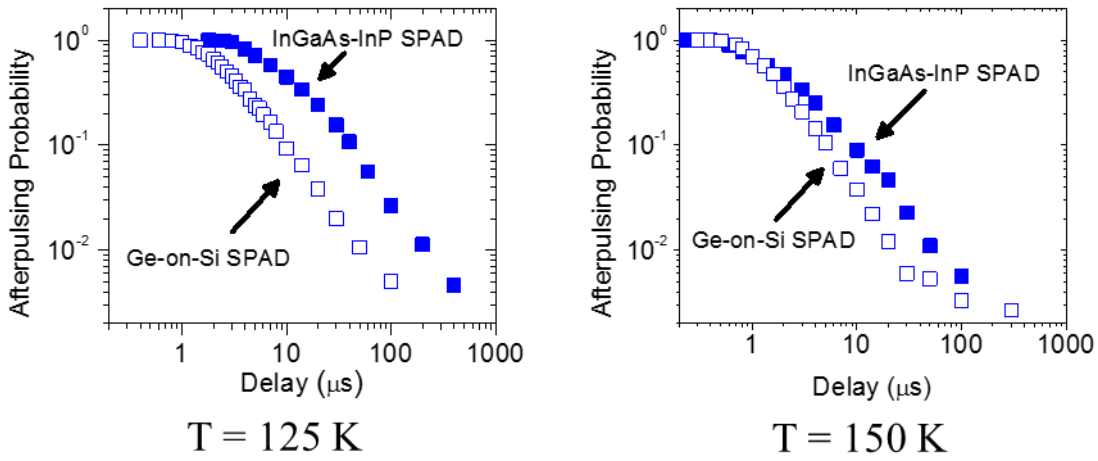

Figure 5.11. Afterpulsing probability of the 100 μm diameter planar Ge-on-Si SPAD (empty squares) and the 25 μm diameter state-of-the-art InGaAs/InP SPAD (solid squares) operated at a temperature of 125 K (left) and 150 K (right). Both detectors appropriately biased to achieve an SPDE of 17%.

It should be noted that although the absolute afterpulsing probabilities will be affected by the operating conditions, for example the gate duration, these results serve to provide a comparison between the two detector types under nominally identical operating conditions. These initial results demonstrate considerable promise for further afterpulsing improvement as the Si epilayer material quality, in particular, is improved.

5.8 Single-photon characterisation of 26 μm diameter planar Ge-on-Si SPADs

After improving the planarization process by introducing trenches for electrical isolation instead of super-pixel design approach, which was employed for the previous generation devices, our colleagues were able to fabricate smaller area detectors. Figure 5.12 illustrates the final design of the trench. The trench width is ~ 3 – 4 μm. It can be observed from Figure 5.12 that the sample is coated with a 165 nm thick layer of Si_3N_4, which acts as an ARC as well as passivation. In addition, a layer of HSQ is used to fill the trench before the metal contact deposition.

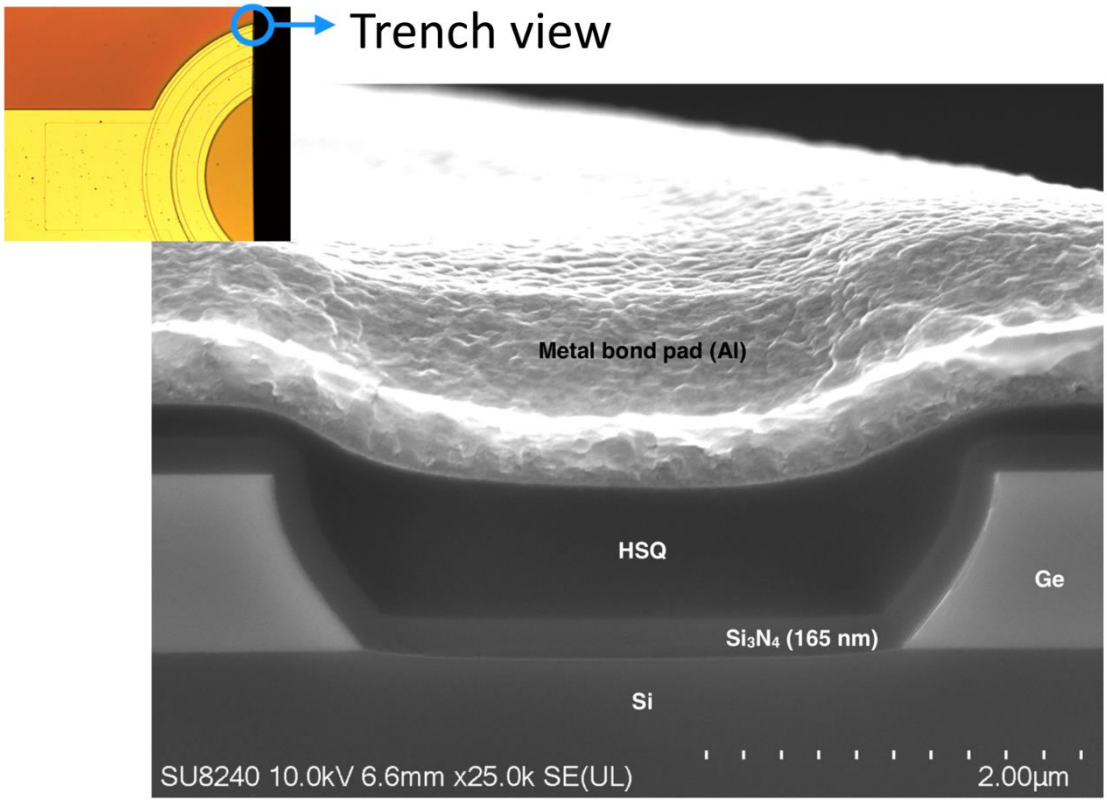

Figure 5.12. An SEM image of the trench introduced to provide electrical isolation.

Single-photon characterisation of the 26 µm diameter planar Ge-on-Si SPADs, which employed trenches for the electrical isolation was performed at the end of 2018 and will be presented in this section. Figures 5.13 – 5.15 demonstrate SPDE and DCR of these devices measured at 78 K, 100 K and 125 K respectively. It can be observed that the lowest DCR of 460 counts^{-1} was measured at a temperature of 100 K and an excess bias of 1.5%. This value is an order of magnitude lower than the value for the 100 µm diameter SPADs operated under identical conditions with the corresponding 0.94 count $s^{-1}µm^{-2}$ and 9.95 count $s^{-1}µm^{-2}$ respectively. However, SPDE of the 26 µm diameter detectors at 1.5% excess bias was 10%, which is lower than the 19% measured using the 100 µm diameter device.

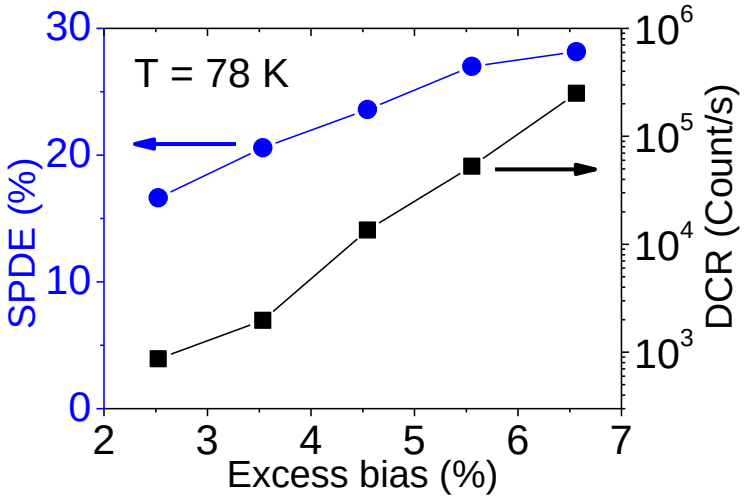

Figure 5.13. SPDE and DCR of the 26 μm diameter planar Ge-on-Si SPAD operated at a temperature of 78 K as a function of the excess bias.

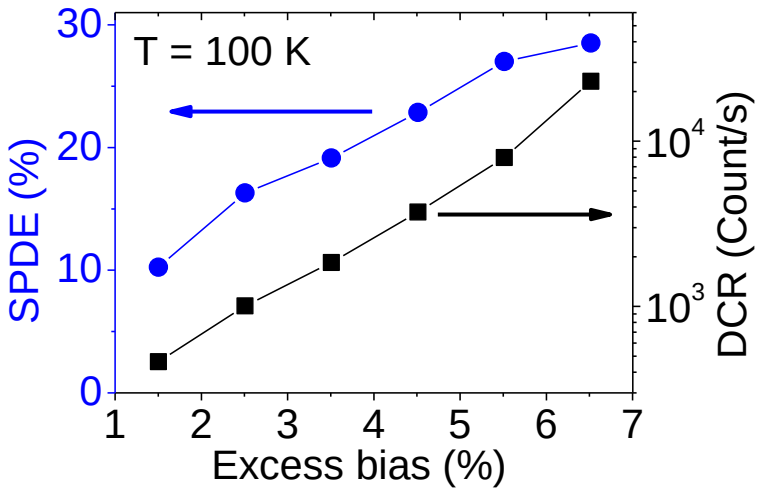

Figure 5.14. SPDE and DCR of the 26 μm diameter planar Ge-on-Si SPAD operated at a temperature of 100 K as a function of the excess bias.

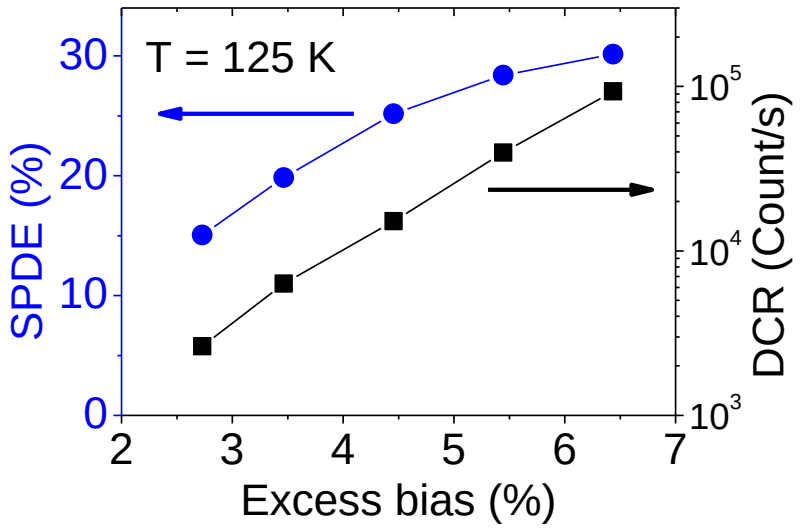

Figure 5.15. SPDE and DCR of the 26 μm diameter planar Ge-on-Si SPAD operated at a temperature of 125 K as a function of the excess bias.

A maximum SPDE of 30% was measured using the 26 μm diameter detector at a temperature of 125 K and excess bias of 6.5% is lower compared to SPDE of 38% measured using the 100 μm diameter detector biased at 5.5% excess bias at the same temperature. These detectors exhibited DCR of 94 kcount s^{-1} and 2 Mcount s^{-1} respectively. It was expected that SPDE for the smaller detector would be lower due to the smaller active area of the device. The beam diameter used in the SPDE measurements was similar to the diameter of the device active area. Therefore, due to the Gaussian profile of the laser pulse a fraction of light was lost at the edge of the detector due to its non-uniform sensitivity profile. The results measured at a temperature of 100 K demonstrate a five times improvement compared to the 100 μm diameter SPADs and four orders of magnitude difference when compared to a mesa geometry Ge-on-Si SPAD developed previously by our group. A 25 μm diameter mesa SPAD exhibited a DCR of 5.5 Mcount s^{-1} at a temperature of 100 K [15]. This corresponds to 11.2 kcount $s^{-1}μm^{-2}$, which is four orders of magnitude higher than 3.5 count $s^{-1}μm^{-2}$ measured using the 26 μm diameter Ge-on-Si SPAD reported here and five times lower than the value for 100 μm diameter device. It should also be noted that, under these conditions, the SPDE reported in [15] is 4%, compared to 19% (26 μm diameter) and 26% (100 μm diameter) for the SPADs presented here. There is a similar relationship when our results are compared to results from [16] in which the reported DCR is 500 kcount s^{-1} for a 1 μm × 15.9 μm rectangular waveguide SPAD at a temperature of 80 K. This corresponds to

31.4 kcount $s^{-1}\mu m^{-2}$, which is five orders of magnitude higher than 1.7 count $s^{-1}\mu m^{-2}$ measured using 26 µm diameter SPAD and four times lower than 6.37 count $s^{-1}\mu m^{-2}$ measured using 100 µm diameter SPAD presented in this Chapter. They report an SPDE of 5% while the SPADs presented here have SPDE of 17% and 22% respectively.

At 78 K we have calculated a record low NEP for a Ge-on-Si SPAD of 4×10^{-17} $WHz^{-1/2}$. It is almost five times lower than the lowest NEP of 1.9×10^{-16} $WHz^{-1/2}$ measured for 100 µm diameter detectors and a more than two hundred-fold improvement, respectively, when compared to the previously reported NEP of the mesa geometry Ge-on-Si SPADs [15]. NEP values of 4×10^{-17} $WHz^{-1/2}$ and 7×10^{-17} $WHz^{-1/2}$ were calculated for temperatures of 100 K and 125 K respectively.

Figure 5.16 shows a timing histogram taken using the 26 µm diameter planar Ge-on-Si SPAD at an excess bias of 6.5% operated at a temperature of 78 K and illuminated with 1310 nm wavelength light. Timing histograms with a bin width of 19.5 ps recorded by the photon counting card were used to calculate the device jitter. The jitter is defined as the full-width-at-half maximum (FWHM) of the histogram and was found to be 150 ps.

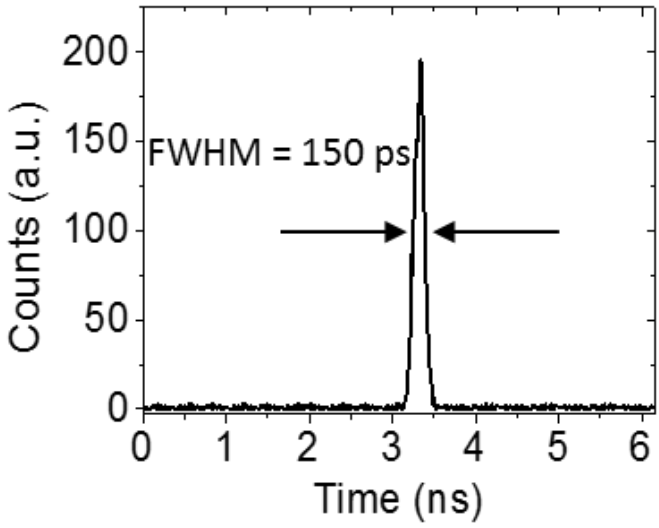

Figure 5.16. A timing histogram recorded using the 26 µm diameter planar Ge-on-Si SPAD at an excess bias of 6.5% operated at a temperature of 78 K and illuminated with 1310 nm wavelength radiation. The FWHM jitter is 150 ps.

This value is comparable to commercially available InGaAs/InP SPADs from Micro Photon Devices, for example.

5.9 Conclusions

In this Chapter, high performance Ge-on-Si SPADs, designed using an innovative planar geometry that utilised implantation and regrowth fabrication techniques have been presented. These SPADs have demonstrated an SPDE of up to 38% at 125 K at a detection wavelength of 1310 nm. This is a significant step change improvement in the performance levels from all previous reports of Ge-on-Si SPADs, and now allowing a more favourable comparison with commercial InGaAs/InP SPADs. The NEP of 4×10^{-17} $WHz^{-1/2}$ at a temperature of 100 K is a more than two hundred-fold improvement on all previously reported Ge-on-Si SPADs [15, 16, 18]. A study of the SPDE dependence as a function of the operating wavelength has revealed that successful operation at 1550 nm wavelength will be possible at 245 K, compatible with Peltier cooling. Afterpulsing performance has been analysed using the time-correlated carrier counting method and compared to a commercial InGaAs/InP SPAD. With little device optimisation having taken place, this initial Ge-on-Si SPAD detector can already operate with between a 50% and 75% reduction in dead-time compared to commercial InGaAs/InP SPADs under the same operating conditions, potentially leading to much higher maximum count rates. These results point to a clear route to smaller volume detectors incorporating thicker Ge absorbers being capable of operation at, or near, room temperature, at low dark count rates, low afterpulsing and high count rate operation. The increased temperature will also allow these detectors to operate with high-efficiency at 1550 nm wavelength. The use of a Si platform provides a low-cost route for single-photon 3D imaging and sensing in the eye-safe short-wave infrared region. This could have significance for a range of commonplace applications such as automotive and autonomous vehicle LIDAR, security and environmental LIDAR monitoring in addition to be enabling for a range of quantum technology applications that use the important telecommunications wavelengths.

In the next Chapter, a LIDAR system incorporating an individual Ge-on-Si SPAD will be presented. In addition, the results of three-dimensional LIDAR imaging using 1450 nm wavelength radiation and estimations of the laser power required for successful imaging at longer distances of up to 10 km will be presented as well.

5.10 Acknowledgements

All the devices described in this Chapter were fabricated by our colleagues at University of Glasgow. Single-photon characterisation results of planar 100 µm diameter Ge-on-Si SPAD detectors presented in Figures 5.3 – 5.7, 5.9, 5.10 and 5.11 (left) have been reported in Ref. [12].

5.11 References

1. R.H. Hadfield, *Single-photon detectors for optical quantum information applications.* Nature Photonics, 2009. **3**(12): p. 696.

2. A. Boaron, B. Korzh, R. Houlmann, G. Boso, D. Rusca, S. Gray, M.-J. Li, D. Nolan, A. Martin, and H. Zbinden, *Simple 2.5 GHz time-bin quantum key distribution.* Applied Physics Letters, 2018. **112**(17): p. 171108.

3. P.J. Clarke, R.J. Collins, P.A. Hiskett, M.-J. García-Martínez, N.J. Krichel, A. McCarthy, M.G. Tanner, J.A. O'Connor, C.M. Natarajan, S. Miki, M. Sasaki, Z. Wang, M. Fujiwara, I. Rech, M. Ghioni, A. Gulinatti, R.H. Hadfield, P.D. Townsend, and G.S. Buller, *Analysis of detector performance in a gigahertz clock rate quantum key distribution system.* New Journal of Physics, 2011. **13**(7): p. 075008.

4. B. Schwarz, *LIDAR: Mapping the world in 3D.* Nature Photonics, 2010. **4**(7): p. 429.

5. A.M. Pawlikowska, A. Halimi, R.A. Lamb and G.S. Buller, *Single-photon three-dimensional imaging at up to 10 kilometers range.* Optics Express, 2017. **25**(10): p. 11919-11931.

6. A. McCarthy, X. Ren, A. Della Frera, N.R. Gemmell, N.J. Krichel, C. Scarcella, A. Ruggeri, A. Tosi, and G.S. Buller, *Kilometer-range depth imaging at 1550 nm wavelength using an InGaAs/InP single-photon avalanche diode detector.* Optics Express, 2013. **21**(19): p. 22098-22113.

7. R. Tobin, A. Halimi, A. McCarthy, X. Ren, K.J. McEwan, S. McLaughlin, and G.S. Buller, *Long-range depth profiling of camouflaged targets using single-photon detection.* Optical Engineering, 2017. **57**(3): p. 031303.

8. R. Tobin, A. Halimi, A. McCarthy, M. Laurenzis, F. Christnacher, and G.S. Buller, *Three-dimensional single-photon imaging through obscurants.* Optics Express, 2019. **27**(4): p. 4590-4611.

9. A. Maccarone, A. McCarthy, X. Ren, R.E. Warburton, A.M. Wallace, J. Moffat, Y. Petillot, and G.S. Buller, *Underwater depth imaging using time-correlated single-photon counting.* Optics Express, 2015. **23**(26): p. 33911-33926.

10. A. Halimi, A. Maccarone, A. McCarthy, S. McLaughlin and G.S. Buller, *Object depth profile and reflectivity restoration from sparse single-photon data acquired in underwater environments.* IEEE Transactions on Computational Imaging, 2017. **3**(3): p. 472-484.

11. E. Sciacca, A.C. Giudice, D. Sanfilippo, F. Zappa, S. Lombardo, R. Consentino, C. Di Franco, M. Ghioni, G. Fallica, and G. Bonanno, *Silicon planar technology for single-photon optical detectors.* IEEE Transactions on Electron Devices, 2003. **50**(4): p. 918-925.

12. P. Vines, K. Kuzmenko, J. Kirdoda, D.C. Dumas, M.M. Mirza, R.W. Millar, D.J. Paul, and G.S. Buller, *High performance planar germanium-on-silicon single-photon avalanche diode detectors.* Nature Communications, 2019. **10**(1): p. 1086.

13. A. Lacaita, P. Francese, F. Zappa and S. Cova, *Single-photon detection beyond 1 μm: performance of commercially available germanium photodiodes.* Applied Optics, 1994. **33**(30): p. 6902-6918.

14. P.A. Hiskett, G.S. Buller, A.Y. Loudon, J.M. Smith, I. Gontijo, A.C. Walker, P.D. Townsend, and M.J. Robertson, *Performance and design of InGaAs/InP photodiodes for single-photon counting at 1.55 μm.* Applied Optics, 2000. **39**(36): p. 6818-6829.

15. R.E. Warburton, G. Intermite, M. Myronov, P. Allred, D.R. Leadley, K. Gallacher, D.J. Paul, N.J. Pilgrim, L.J.M. Lever, Z. Ikonic, R.W. Kelsall, E. Huante-Ceron, A.P. Knights, and G.S. Buller, *Ge-on-Si Single-Photon Avalanche Diode Detectors: Design, Modeling, Fabrication, and Characterization at Wavelengths 1310 and 1550 nm.* IEEE Transactions on Electron Devices, 2013. **60**(11): p. 3807-3813.

16. N.J. Martinez, M. Gehl, C.T. Derose, A.L. Starbuck, A.T. Pomerene, A.L. Lentine, D.C. Trotter, and P.S. Davids, *Single photon detection in a waveguide-coupled Ge-on-Si lateral avalanche photodiode.* Optics Express, 2017. **25**(14): p. 16130-16139.

17. G. Buller, S. Fancey, J. Massa, A. Walker, S. Cova, and A. Lacaita, *Time-resolved photoluminescence measurements of InGaAs/InP multiple-quantum-well structures at 1.3-μm wavelengths by use of germanium single-photon avalanche photodiodes.* Applied Optics, 1996. **35**(6): p. 916-921.

18. Z. Lu, Y. Kang, C. Hu, Q. Zhou, H.-D. Liu, and J.C. Campbell, *Geiger-Mode Operation of Ge-on-Si Avalanche Photodiodes.* IEEE Journal of Quantum Electronics, 2011. **47**(5): p. 731-735.

19. J. Zhang, M.A. Itzler, H. Zbinden and J.-W. Pan, *Advances in InGaAs/InP single-photon detector systems for quantum communication.* Light: Science & Applications, 2015. **4**(5): p. e286.

20. A. Tosi, N. Calandri, M. Sanzaro and F. Acerbi, *Low-noise, low-jitter, high detection efficiency InGaAs/InP single-photon avalanche diode.* IEEE Journal of Selected Topics in Quantum Electronics, 2014. **20**(6): p. 192-197.

21. E. Amri, G. Boso, B. Korzh and H. Zbinden, *Temporal jitter in free-running InGaAs/InP single-photon avalanche detectors.* Optics Letters, 2016. **41**(24): p. 5728-5731.

22. D.J. Paul, *8-band k. p modeling of the quantum confined Stark effect in Ge quantum wells on Si substrates.* Physical Review B, 2008. **77**(15): p. 155323.

23. M.A. Itzler, R. Ben-Michael, C.-F. Hsu, K. Slomkowski, A. Tosi, S. Cova, F. Zappa, and R. Ispasoiu, *Single photon avalanche diodes (SPADs) for 1.5 μ m photon counting applications.* Journal of Modern Optics, 2007. **54**(2-3): p. 283-304.

24. A. Lacaita and M. Mastrapasqua, *Strong dependence of time resolution on detector diameter in single photon avalanche diodes.* Electronics Letters, 1990. **26**(24): p. 2053-2054.

25. S. Wang, F. Ma, X. Li, G. Karve, X. Zheng, and J.C. Campbell, *Analysis of breakdown probabilities in avalanche photodiodes using a history-dependent analytical model.* Applied Physics Letters, 2003. **82**(12): p. 1971-1973.

26. Y. Ishikawa, K. Wada, D.D. Cannon, J. Liu, H.-C. Luan, and L.C. Kimerling, *Strain-induced band gap shrinkage in Ge grown on Si substrate.* Applied Physics Letters, 2003. **82**(13): p. 2044-2046.

27. Y.P. Varshni, *Temperature dependence of the energy gap in semiconductors.* Physica, 1967. **34**(1): p. 149-154.

28. G.S. Buller, S. Pellegrini, R.E. Warburton, J.S. Ng, L.J. Tan, A. Krysa, J.P. David, and S. Cova, *Semiconductor avalanche diode detectors for quantum cryptography.* IEEE–LEOS Newsletter, 2006. **20**: p. 20-24.

29. X. Jiang, M.A. Itzler, R. Ben-Michael and K. Slomkowski, *InGaAsP–InP avalanche photodiodes for single photon detection.* IEEE Journal of Selected Topics in Quantum Electronics, 2007. **13**(4): p. 895-905.

30. B. Korzh, T. Lunghi, K. Kuzmenko, G. Boso and H. Zbinden, *Afterpulsing studies of low-noise InGaAs/InP single-photon negative-feedback avalanche diodes.* Journal of Modern Optics, 2015. **62**(14): p. 1151-1157.

31. A. Tosi, A.D. Mora, F. Zappa and S. Cova, *Single-photon avalanche diodes for the near-infrared range: detector and circuit issues.* Journal of Modern Optics, 2009. **56**(2-3): p. 299-308.

32. H. Statz, L. Davis Jr and A. Adams Jr, *Surface states on silicon and germanium surfaces.* Physical Review, 1957. **106**(3): p. 455.

33. R. Zhang, T. Iwasaki, N. Taoka, M. Takenaka and S. Takagi, *Al 2 O 3/GeO x/Ge gate stacks with low interface trap density fabricated by electron cyclotron resonance plasma postoxidation.* Applied Physics Letters, 2011. **98**(11): p. 112902.

Chapter 6. Three-dimensional imaging using planar Ge-on-Si SPAD detectors

6.1 Introduction

Following the single-photon characterisation of the planar geometry Ge-on-Si SPAD detectors discussed in the previous Chapter, we use these detectors in Light Detection and Ranging (LIDAR) measurements to ascertain the potential of these detectors in this application. In this Chapter, a brief overview of the LIDAR technique will be given along with the motivation for operation in the short-wavelength infrared (SWIR) region. This will be followed by a description of the LIDAR three-dimensional (3D) imaging experiment. Finally, based on a parametric model calibrated using these experimental results, predictions of the average laser power levels required for imaging at longer distances and in attenuating media are given. The estimations will be presented along with a discussion of the system performance and maximum distance range achievable while operating at eye-safe optical power levels.

LIDAR is the technique of choice commonly used for the investigation of solid or gaseous targets. This technique has been employed in a variety of remote sensing applications, such as environmental monitoring [1], defence [2], and terrain mapping [3]. The basic LIDAR set-up consists of three parts: the transmitter, the receiver and the detection unit. Figure 6.1 illustrates schematically the basic LIDAR system [4]. The transmitter consists of a pulsed laser source and a beam expander, which is used to control the divergence of the beam before it is directed towards a target. The receiver collects the backscattered light, which is then directed onto an optical analysing system. This system, depending on the application, processes the light so only specific polarisation states or wavelengths out of all the collected light reach the detection unit (an individual detector or a detector array). This detector converts the received optical signal into an electrical one. The collected data is further analysed using various methods to extract the distance information. Two examples of such methods will be discussed in section 6.3.

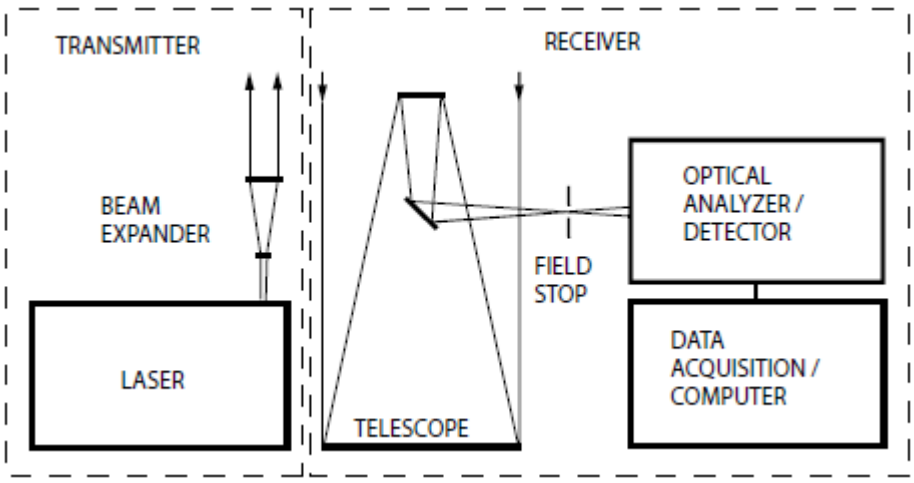

Figure 6.1. A schematic diagram of a LIDAR system. From Ref. [4]. The laser inside the transmitter generates optical pulses and the beam expander reduces the divergence of the light beam. The receiver collects the backscattered photons and directs it towards a detection unit. The computer then processes the collected data.

As the name suggests, in the LIDAR technique the reflected light is used to determine the distance to an object from the time-of-flight (ToF) of the returned light pulses [2]. The time that an energy pulse takes to reach the target and return is measured. The distance to the target is then calculated by multiplying half of the measured time by the speed of light. The accuracy of the system depends on the number of pulses measured, hence, on the acquisition time. The resolution of the system increases with the amount of the distance data collected. In LIDAR, the time-correlated single-photon counting (TCSPC) technique, as described in Chapter 5, has proven to have higher sensitivity and better surface-to-surface resolution when compared to the conventional ToF technique [5, 6]. It can be used in various weather conditions including fog and haze in addition to highly attenuated media such as water. It is particularly suitable for ToF ranging and imaging where a picosecond time resolution is prefered and a low number of return photons are expected such as multispectral depth imaging [7] and underwater depth imaging [8, 9]. In addition, due to its single-photon sensitivity, TCSPC LIDAR can employ eye-safe laser powers for long-range depth imaging [10-12].

In LIDAR systems, utilising short-wavelength infrared (SWIR) light, with wavelengths between 1.4 and 3 μm, has several advantages when compared to near-infrared (NIR)

light. First, higher laser power levels remain eye-safe when operated at longer wavelengths [13]. For instance, at 1.4 – 1.7 μm wavelengths of operation, the laser power level considered to be eye-safe for continuous wave radiation is 10 mW, in a small spot diameter, which is approximately 20 times greater than at wavelengths around 850 nm [13]. Secondly, significant attenuation of NIR radiation occurs due to absorption caused by water vapour, CO_2, CH_4 and other gases in the atmosphere, while the SWIR spectrum has almost 100% transmission in the atmosphere [14, 15]. In imaging through obscurants, the use of 1550 nm wavelength radiation shows better performance when compared to visible wavelengths [16]. In addition, attenuation due to fog is ~18% less for 1550 nm wavelength radiation when compared to that of 830 nm at a distance of 100 m [17]. Thirdly, solar radiation contains a greater fraction of visible and NIR light that contributes to undesirable background noise in LIDAR that operate in these wavelength regions [18, 19].

A variety of photodetectors have been used in the past for 3D imaging using NIR light. Individual Si SPAD detectors [20-23] and CMOS Si SPAD arrays [24-26] have been employed in single-photon LIDAR systems using NIR light of less than 1 μm wavelengths. However, development of a highly efficient compact semiconductor single-photon detector for SWIR wavelength region remains a great challenge. At present, InGaAs/InP SPAD arrays are commonly used in experiments involving single-photon detection of up to 1.8 μm wavelengths [10, 16, 27, 28]. However, arrays of InGaAs/InP detectors are incompatible with Si CMOS and are typically prohibitively expensive for mass market applications. They also have limited maximum count rates due to afterpulsing effects [29]. As discussed in Chapter 2, another alternative for single-photon detection in the SWIR region is superconducting nanowire single-photon detectors (SNSPDs) [30, 31]. There are reports that these detectors have been successfully used in LIDAR experiments [32, 33]. However, SNSPDs operate at cryogenic temperatures, typically below 4 K [31, 34]. Such temperatures of operation require additional vacuum and cooling equipment, which presents a major disadvantage for using these detectors in imaging applications.

Over the past decade, research has been carried out towards developing alternative SPAD detectors that use Ge as an absorber and Si for carrier multiplication. Those detectors could be CMOS compatible and have potential for development of inexpensive and

highly efficient SPAD arrays. Ge-on-Si SPAD design structures such as normal incidence mesa [35, 36] and waveguide geometries [37] have been demonstrated so far. Those detectors have shown potential for single-photon detection in the SWIR region with single-photon detection efficiencies (SPDEs) up to 5.27% for 1310 nm wavelength illumination while operated at 100 K (mesa Ge-on-Si SPAD [35]) and 80 K (waveguide SPAD [37]). However, they exhibited prohibitively high dark count rates (DCRs) of up to 31.4 kcount $s^{-1}\mu m^{-2}$, making them unsuitable for existing applications. In Chapter 4, we have discussed the design of innovative planar Ge-on-Si SPAD detectors and the advantages of the planar geometry. In Chapter 5, single-photon characterisation of these detectors and their limitations were presented. The planar Ge-on-Si SPADs exhibited less afterpulsing compared to InGaAs/InP, which increases the maximum count rate possible. Therefore, our planar Ge-on-Si SPADs show the potential for developing of the efficient Ge-on-Si SPAD arrays as a competing alternative to InGaAs/InP SPADs cameras.

In this Chapter, a successful demonstration of 3D LIDAR imaging using SWIR illumination of 1450 nm wavelength in laboratory conditions will be presented along with the obtained depth and intensity profiles of the chosen targets. First, we will describe the single-photon LIDAR imaging system used in the experiments. This will be followed by an explanation of the pixel-wise cross-correlation approach to reconstructing the images and examples of reconstructed depth and intensity profiles of selected targets for a range of per pixel acquisition times from 30 ms to 0.5 ms. After discussing those results, we will discuss the potential of the Restoration of Depth and Intensity using Total Variation [38] (RDI-TV) algorithm for image reconstruction. This algorithm facilitates further reduction of the total acquisition time by reconstructing the image from as little information as 25% of the scene randomly scanned. Finally, estimations of the laser powers required for imaging at longer distances of up to 10 km using SWIR radiation of 1310 and 1450 nm wavelength will be given. In addition, estimations of the laser powers required for imaging at 300 metres in various attenuating media will be presented.

6.2 Single-photon depth imaging system

In order to demonstrate the potential of Ge-on-Si SPADs in LIDAR and depth imaging applications, the experimental set-up shown in Figure 6.2 was used. The TCSPC technique was used to acquire the ToF data. The stand-alone TCSPC module (PicoHarp

300, PicoQuant) was synchronised with the supercontinuum laser source (SuperK EXTREME EXW-6, NKT Photonics) and recorded the time elapsed between the laser pulse emission and the triggering of the SPAD by an incident photon using 4 ps timing bins. The detector was operated in a gated mode in which it was biased above breakdown for 50 ns around the expected time of a photon arrival. This time-tagged detection event information was transferred to a computer via a USB connection. The time that it takes a photon to travel to the target and back to the detector reveals the depth information of the target. ToF data for each pixel was collected over thousands of laser pulses. The target was illuminated with 1450 nm wavelength light via a reflective collimator, RC, Si beam splitter, BS (31/69) and an objective lens, L_1, with an aperture of 25.4 mm and an effective focal length of 400 mm. The wavelength of 1450 nm was chosen for its increased laser-safety threshold in addition to the relatively high SPDE at this wavelength demonstrated by the detector. As shown in Figure 6.2, a parallax-free monostatic optical system with the objective lens L_1 was used to focus the light on the target and to collect the back-scattered photons. The effective laser repetition rate used in these measurements was 104 kHz. The minimum repetition rate of the laser source is 312 kHz; however, it was impossible to operate the SPAD at such count rates due to a prohibitively high DCR. Therefore, the count rate of the detector was down converted using a pulse pattern generator to 104 kHz, which means that the detector was sensitive to only one third of the laser pulses. Operation at high count rates above 100 kHz allows for faster data acquisition. A JGR Optics AO5 optical attenuator allowed for control over the output laser power. The maximum average laser power used for the measurements was 912 pW. Return light reflected from the beam splitter BS was focused on a 100 μm diameter planar Ge-on-Si SPAD via lens L_2. The detector was situated inside an Oxford Instruments cryostat and was operated at a temperature of 100 K. This SPAD exhibited a DCR of 4.7 Mcounts/s and a SPDE of 10% at an excess bias of 1.5% at this temperature, which were determined using the TCSPC technique as described in Chapter 5. All measurements were performed at a stand-off distance of 0.4 m and in a dark laboratory environment. Hence, no solar background was considered in these measurements or subsequent modelling. The target was mounted on motorised translation stages to allow an X - Y raster scan.

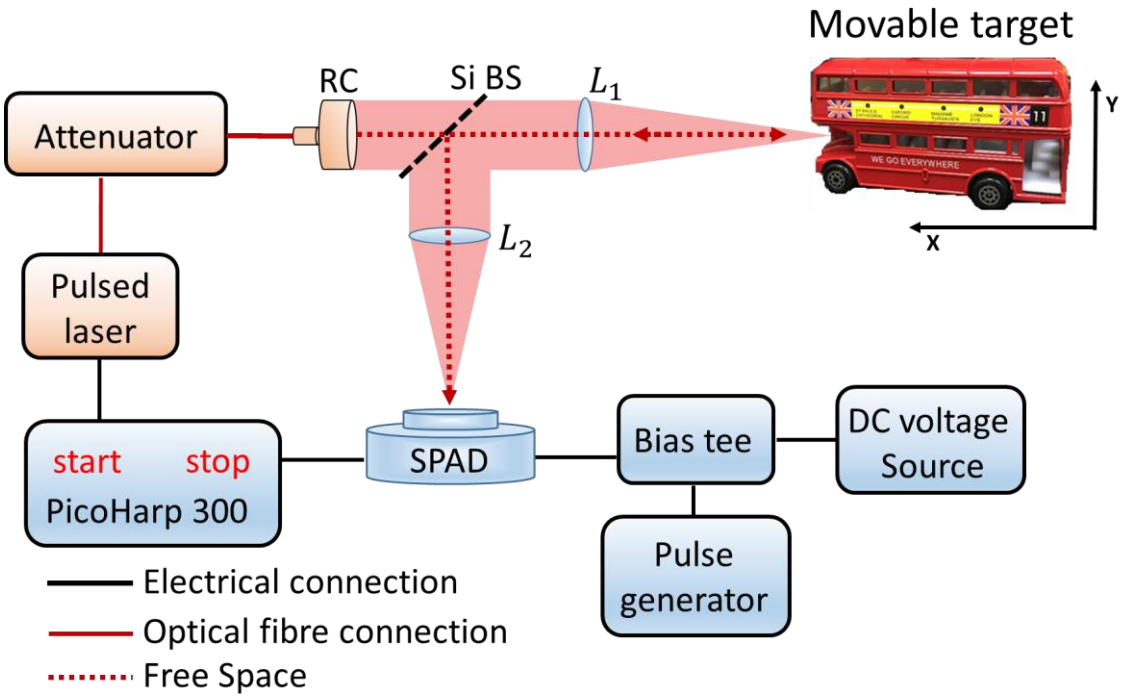

Figure 6.2. The experimental set-up. The target was mounted on motorised translation stages, which allowed for raster scanning. The reflective collimator, RC, and objective lens, L_1, focused 1450 nm wavelength light on the target. Light reflected from the Si 69/31 beam splitter was then focused via lens L_2 onto the 100 μm diameter planar Ge-on-Si SPAD. The stand-alone TCSPC module PicoHarp 300, synchronised with the laser, collected the data.

6.3 Image reconstruction algorithms

LIDAR and other sensors for automotive applications typically require rapid measurement and analysis on the timescale of $<$ 10 ms to allow the driver to decide and take appropriate action. In the case of scanning LIDAR, this could mean per-pixel acquisition times on the scale of $\ll$ 1 μs. Such a short acquisition time inevitably leads to the reduction of the number of recorded photon events. Increasing the laser power or the repetition rate of the source would allow maintaining similar levels of the return photons. However, most applications are restricted by laser safety protocols, which means that the average laser power has to remain below 10 mW for most of the SWIR wavelength region [13]. Therefore, the preferred approach to reducing the total acquisition time involves image processing algorithms designed to work in the sparse photon regime. Several bespoke image reconstruction algorithms have been demonstrated for depth and intensity

image restoration from sparse single-photon data [39-41] including data from long-range imaging [11] and underwater imaging [9]. In this section, a brief description of two reconstruction algorithms: pixel-wise cross-correlation and the restoration of depth and intensity using total variation (RDI-TV) algorithm will be given. Statistical image processing techniques such as RDI-TV generally allow improved image reconstruction when only partial information of the scene is available.

6.3.1 Pixel-wise cross-correlation

For all the measurements, timing histograms containing ToF information were acquired for each pixel. Depth and intensity image profiles were reconstructed from these histograms using the cross-correlation method, previously described in references [8, 10, 32, 42]. For each pixel location, a cross-correlation, $\boldsymbol{c}$, between the measured timing histogram, $\boldsymbol{h}$, and an instrumental response, **g**, was performed:

$$c_\tau = \sum_{j=1}^{N} h_{\tau+j} \cdot g_j, \tag{1}$$

where N is the number of timing bins in the instrumental response and the histogram, j represents the indexing of the time bins, and τ represents the lag time. The ToF is then defined as the lag time for which the cross-correlation is maximised. From this ToF, the depth information of the target can be determined. This operation is repeated for each pixel leading to a three-dimensional image, composed of X and Y positions of the pixels and Z depth information of the target. Additionally, we have built the intensity maps from the acquired histograms. The total number of photon arrival events summed for all the time bins of the histogram peak represents the return signal intensity. The instrument response function, **g**, was obtained from a histogram of a 60 s long measurement of a single pixel in the plane of the target.

6.3.2 The restoration of depth and intensity using total variation algorithm

The Restoration of Depth and Intensity using Total Variation (RDI-TV) algorithm was developed by *Halimi et. al.* [38] with the aim of restoring corrupted or incomplete images. This algorithm accounts for the data statistics and the spatial correlations between the neighbouring pixels to reconstruct depth and intensity images. To reduce the computational cost, RDI-TV considers some assumptions that are easily satisfied by the data used in this work, namely that: the background counts are negligible due to

measurement in dark conditions; the object's depths are always inside the observation window; and the system impulse response is narrower than the observation window. Given these assumptions, the algorithm aims to minimize the cost function $C(\boldsymbol{d}, \boldsymbol{i})$ given by [38]:

$$C(\boldsymbol{d}, \boldsymbol{i}) = L(\boldsymbol{K}\boldsymbol{d}, \boldsymbol{K}\boldsymbol{i}) + \varphi(\boldsymbol{d}, \boldsymbol{i}), \tag{2}$$

where both $\boldsymbol{d}$ and $\boldsymbol{i}$ represent N × 1 vectors the depth and intensity obtained for each pixel, L is the negative log-likelihood function that depends on the data statistics, $\boldsymbol{K}$ is an M × N binary sampling mask that selects some pixels to model the loss of image pixels. This matrix contains a single non-zero value in each line. M is the number of pixels containing information. $\varphi(\boldsymbol{d}, \boldsymbol{i})$ is the regularization term derived from the available prior knowledge about $\boldsymbol{d}$ and $\boldsymbol{i}$ [38]. In this Chapter, we consider the total-variation regularisation term by imposing spatial correlation between a pixel and its 4 neighbours as shown in Figure 6.3.

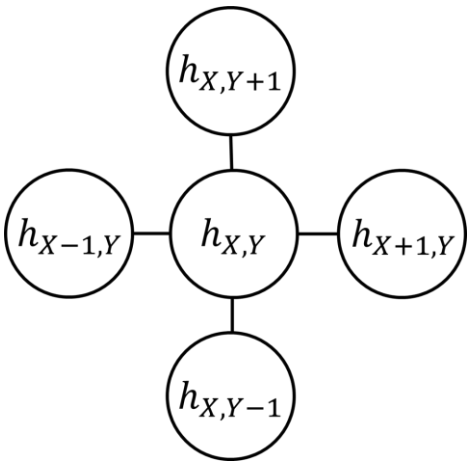

Figure 6.3. The total variation neighbourhood structure. $h_{X,Y}$ represents information extracted from the histogram of the pixel at (X, Y) in terms of depth and intensity.

Based on the above, the cost function can now be presented as:

$$C_{TV}(\boldsymbol{d}, \boldsymbol{i}) = L(\boldsymbol{K}\boldsymbol{d}, \boldsymbol{K}\boldsymbol{i}) + \tau_1 TV(\boldsymbol{d}) + \tau_2 TV(\boldsymbol{i}), \tag{3}$$

where $TV(\boldsymbol{v}) = \sum_{n=1}^{N} \sqrt{(\Delta v_{n,X})^2 + (\Delta v_{n,Y})^2}$, $\Delta v_{n,X}$ and $\Delta v_{n,Y}$ are the first order differences of the quantity v at the n-th pixel in the horizontal and vertical directions, respectively. This is a convex function that can be minimized using several convex

optimization tools, including the Alternating Direction Method of Multipliers (ADMM) algorithm used in [38] for its good convergence properties.

6.4 Reconstructed images

6.4.1 Images reconstructed using the cross-correlation technique

This section presents the results of the depth and intensity estimations reconstructed using the pixel-wise cross-correlation algorithm. The measurements were performed in a dark laboratory with a target positioned at a stand-off distance of 0.4 m. Figure 6.4 presents the reconstructed images using the cross-correlation method. The first two images, Figure 6.4.(a), (b) show photographs of the targets taken with a visible camera. The remaining images are of the reconstructed intensity, Figure 6.4.(a1), (b1), and depth, Figure 6.4.(a2), (b2), profiles of the targets. A model of a double decker bus and a model of a Mini Cooper car were chosen for the experiment to demonstrate the surface-to-surface resolution on multiple features of the vehicle, such as seats, stairs, wheels and windows. Even such small features as the bonnet feature of the car model, are recognisable as can be observed from the Figure 6.4 (b1). For each of the depth and intensity profiles, the inter-pixel spacing was 1 mm with a pixel layout of 123×72 ($X \times Y$) for the bus scan and 100×70 for the car. The model dimensions were $11 \times 3.8 \times 6$ cm and $9.5 \times 6 \times 4.5$ cm ($L \times W \times H$) for the bus and the car, respectively. The measurements were performed using a 300 ms per pixel acquisition time, which resulted in 44.28 minutes total acquisition time for the bus and 35 minutes for the car. The maximum average laser powers directed at the targets were 813 pW and 912 pW for the bus and the car models, respectively. In the next section, we will demonstrate the reconstructed images of these targets recorded using smaller acquisition times per pixel from 30 ms down to 0.5 ms.

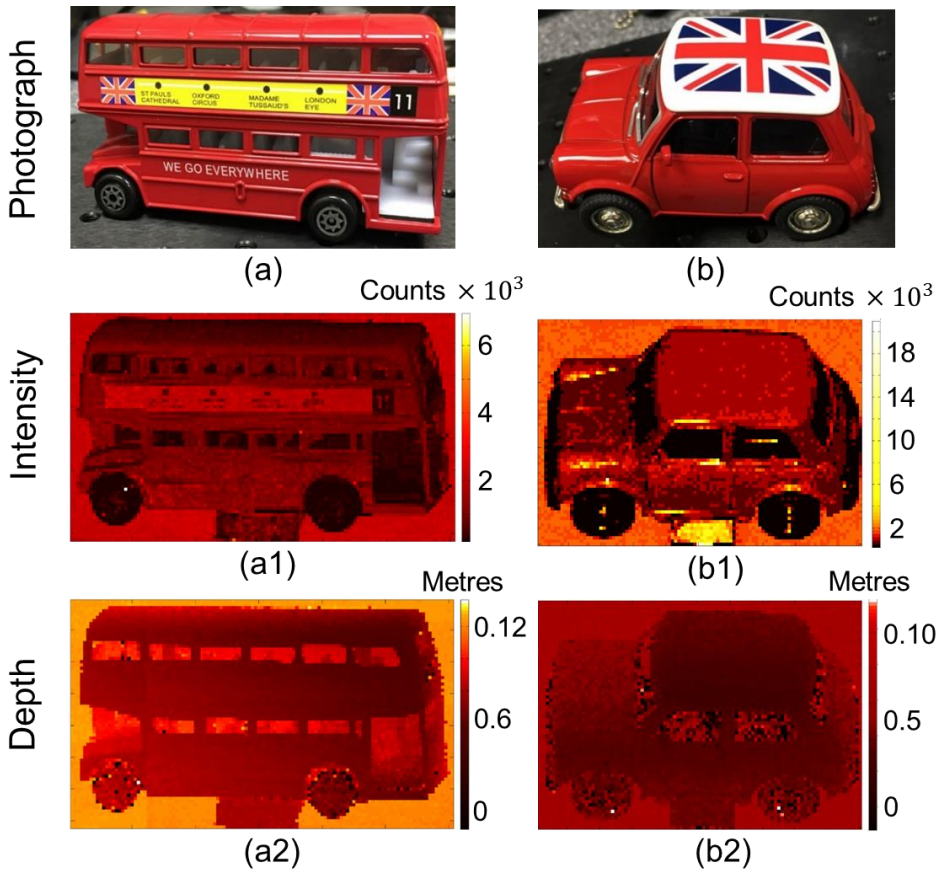

Figure 6.4. Depth and intensity profile measurements of a double decker bus and a Mini Cooper car models acquired in a dark laboratory environment at a stand-off distance of 0.4 m. The images (a) and (b) are close-up photographs of the target models. The scanned scenes consisted of the given target mounted in front of a white cardboard backplane with a maximum front-to-back separation of approximately 100 mm. The area scanned was approximately 123 × 72 mm for the bus and 100 × 70 mm for the car using 123 × 72 and 100 × 70 pixels, respectively, resulting in a pixel-to-pixel spacing of 1 mm in both X and Y. Intensity and depth profiles obtained using 300 ms per-pixel acquisition time are shown in (a1) and (b1), and (a2) and (b2), respectively. An acquisition time of 300 ms per-pixel equates to a total scan time of 44.28 minutes and 35 minutes for the scene of the bus and the car, respectively.

6.4.2 Reconstructed images using reduced acquisition time

Figure 6.5 illustrates the depth and intensity profiles reconstructed from the data acquired at different per-pixel acquisition times of 0.5, 1, 3, 10, and 30 ms. The depth and intensity reconstructions for five different per-pixel acquisition times were constructed using the

cross-correlation technique. An average of less than 8 photons were recorded during the first 0.5 ms of the measurement for each pixel. Such an illustration shows that longer acquisition time provides better quality images. One can see that with a 0.5 ms per pixel acquisition time the system collects enough data such that the target is readily recognisable from a reconstructed image. However, a per pixel acquisition time of 10 ms provides an excellent surface-to-surface resolution allowing surface features of the car bonnet to be distinguished.

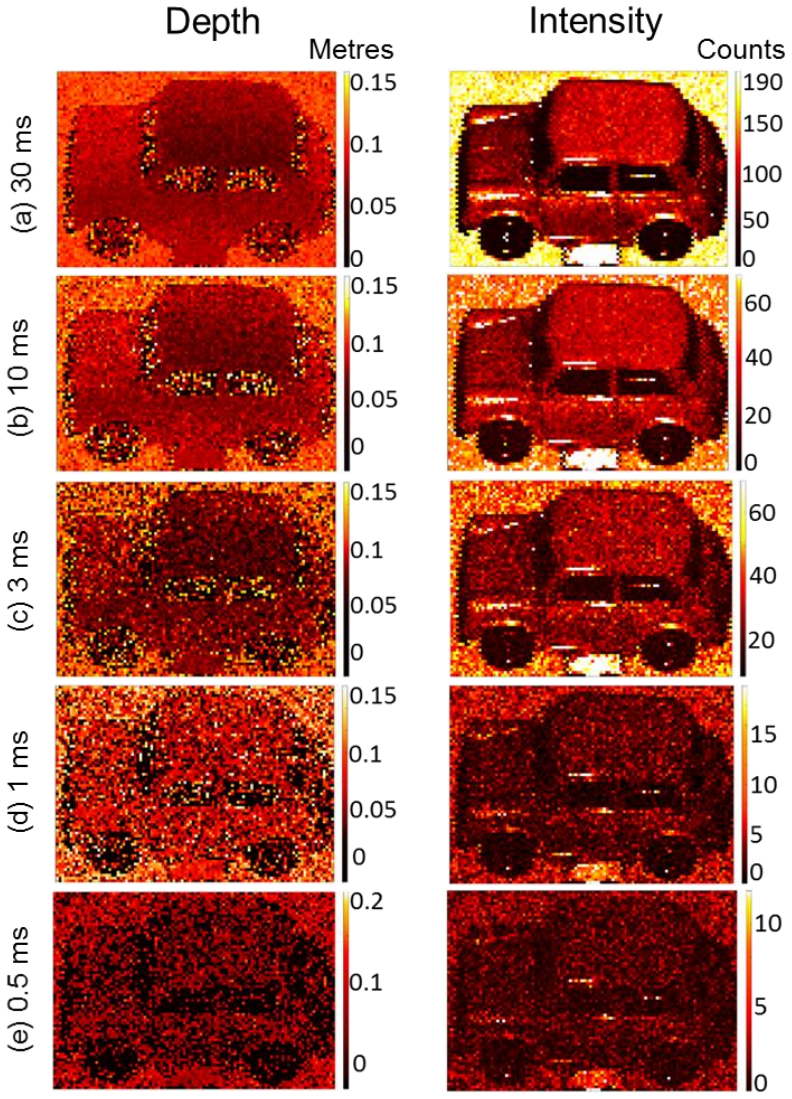

Figure 6.5. The depth and intensity profiles reconstructed from the data acquired at different per-pixel acquisition times: 30ms (a), 10 ms (b), 3 ms (c), 1 ms (d) and 0.5 ms (e). The scene was scanned at a range of 0.4 m in dark laboratory conditions. Reconstructed depth and intensity profiles of the target were built using the cross-correlation technique. In each case, the total acquisition time was: 210 s (a), 70 s (b), 21 s (c), 7 s (d), 3.5 s (e)

In the next section, we will demonstrate that the total acquisition time can be further recuced in a scenario when as few as 25 % of pixels are measured for a given target and additional image reconstructing algorithms are employed.

6.4.3 Reconstructed images with missing pixels

To highlight the benefit of the RDI-TV in reducing the acquisition time, we consider a scenario where only partial information is acquired. This is obtained by scanning a random number of pixels ranging from 75% to 25% of the total number of pixels. Figures 6.6-6.8 present a comparison of the depth and intensity profiles restored using the cross-correlation technique and the RDI-TV algorithm with 75%, 50% and 25% of the scene randomly scanned. The target was scanned with a 10 ms per-pixel acquisition time and 100 × 70 pixels. Figure 6.6 demonstrates that in a scenario when only 25% of data is missing both techniques work well. However, RDI-TV can smooth the image by filling in the missing pixels.

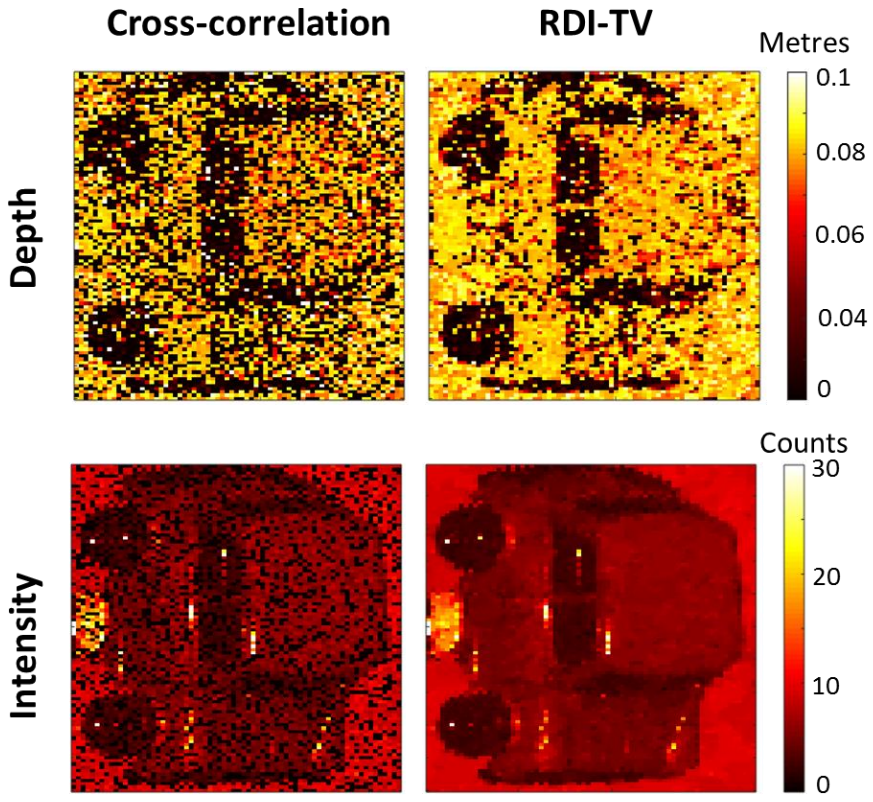

Figure 6.6. Depth and intensity profiles for the 100 × 70 pixels with 10 ms per pixel acquisition time reconstructed using the cross-correlation technique (left) and RDI-TV algorithm (right) with 25% of the pixels removed. The total acquisition time is 52.5 s.

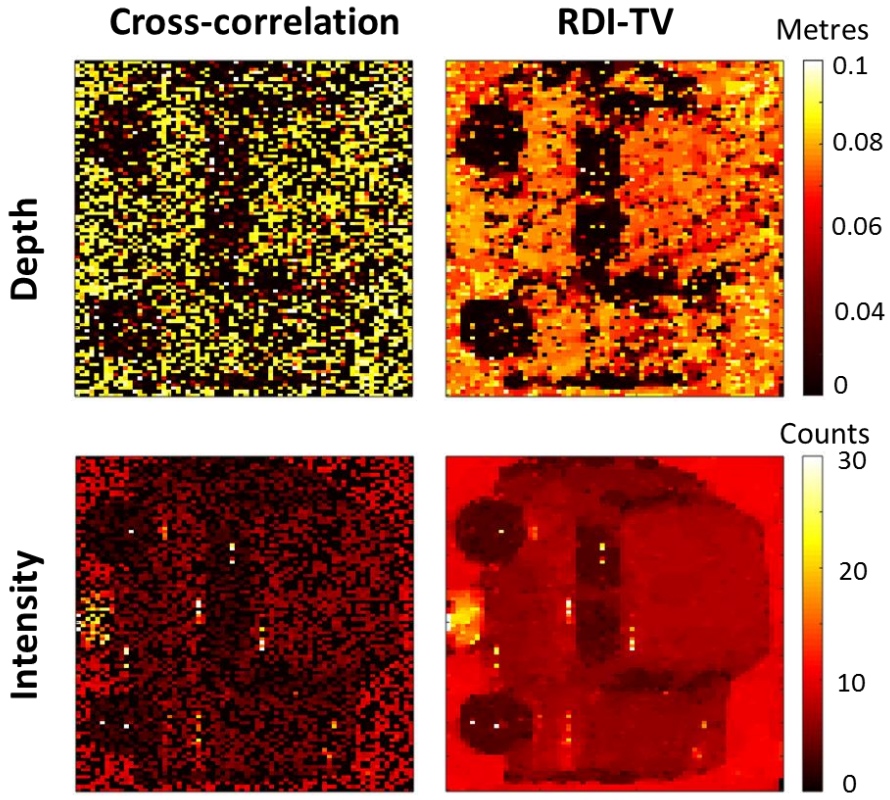

Figure 6.7. Depth and intensity profiles for the 100 × 70 pixels with 10 ms per pixel acquisition time reconstructed using the cross-correlation technique (left) and RDI-TV algorithm (right) with 50% of the pixels removed. The total acquisition time is 35 s.

As demonstrated in Figure 6.7, detail identification using the cross-correlation approach significantly degrades starting from 50% of data missing. The RDI-TV algorithm restores missing pixels by finding depth relationships between neighbouring pixels and allows the identification of important details. Figure 6.8 shows that when missing as much as 75% of the data RDI-TV still provides a good quality reconstructed image in which the target and important details such as wheels and windows can be easily identified. The total acquisition time to acquire the image from Figure 6.8, excluding computational time, is 17.5 s in a scenario where the system uses 10 ms per pixel acquisition time and only 25% of the scene is randomly scanned.

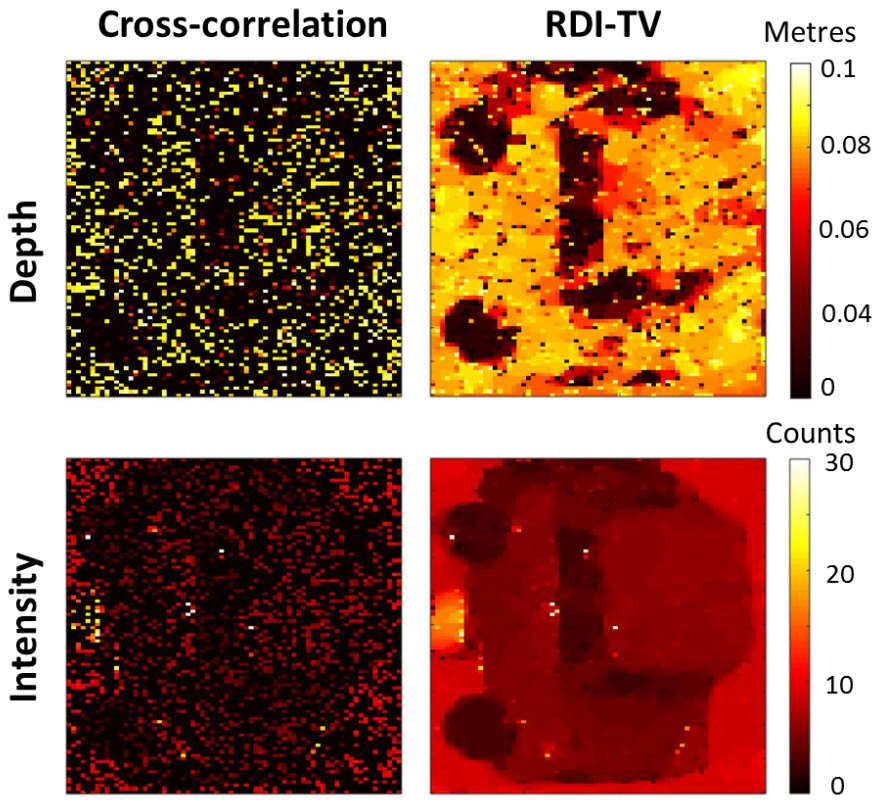

Figure 6.8. Depth and intensity profiles for the 100 × 70 pixels with 10 ms per pixel acquisition time reconstructed using the cross-correlation technique (left) and RDI-TV algorithm (right) with 75% of the pixels removed. The total acquisition time is 17.5 s.

6.5 LIDAR calculations for a system incorporating a 26 µm diameter planar Ge-on-Si SPAD operated at 125 K

Although the results presented in the previous sections demonstrate successful LIDAR imaging using the planar Ge-on-Si SPAD detector, further theoretical estimations of the laser power required for imaging at longer distances was required to fully assess the possibility of using these detectors in autonomous and automotive LIDAR applications. In this section, we will describe the model and present the results of the laser power estimations for imaging at longer distances or in an attenuating medium.

6.5.1 LIDAR formula

The laser power required for successful imaging at longer distances can be estimated using a LIDAR model developed based on the photon-counting version of the LIDAR range equation [43]. This model considers a range of intrinsic and extrinsic parameters such as the attenuation of the optical system, detector performance and reflectance of the target. Assuming that the target scatters the light isotropically, the system would collect only a fraction of the reflected light [4].

$$\frac{I_c}{I_s} = \frac{A_{lens}}{4\pi R^2}, \tag{4}$$

where I_s is the light intensity in the solid angle 4π scattered by a target at a stand-off distance *R*, and I_c is the fraction of reflected light collected by an objective lens of area A_{lens}. Since the detector can detect only back scattered light, our model considers only half of the solid angle. In addition, we assume that the diameter of the detection window is larger than the diameter of the illuminating laser spot. Both the average number of background counts per histogram bin, n_b, and the number of counts in the highest bin, n_p, are essential for the signal-to-noise ratio (SNR) estimation [42]:

$$SNR = \frac{n_p}{\sqrt{n_p + n_b}}. \tag{5}$$

The empirically established minimum signal to noise ratio (SNR) required to obtain a reliable depth estimate for a single pixel measurement is 1.4 [8]. In order to make a prediction of the device performance at higher temperatures of operation in a LIDAR application, we used the data available from Chapter 5. The average background counts per bin, n_b, was estimated as:

$$n_b = DCR \times t \times F \times \tau_b, \tag{6}$$

where DCR is the dark count rate of the detector at a given temperature of operation, *t* is the acquisition time, *F* is the laser repetition rate and τ_b is the bin width. The number of counts in the highest peak of the histogram, n_p, was obtained from Equation 5 using a SNR of 1.4. The laser power levels, when directed at the target, required for successful imaging at much longer distances were estimated as:

$$P_{out} = \frac{hc}{\lambda} \frac{n_p 2\pi R^2}{A_{lens} \rho t C_{in} C_{det} \eta}, \tag{7}$$

where P_{out} is the laser power directed at the target; λ is the operating wavelength; t is the acquisition time; C_{det} is the temporal response of the detector which is the ratio between the number of counts in the highest bin of the histogram to the total number of counts; η is the detection efficiency; A_{lens} is the area of the collecting lens (L_1 in the Figure 6.2); ρ is the reflectivity of the target ; C_{in} is the internal loss of the system due to coupling losses or possible misalignment of individual optical components; R is the distance to the target; h is Planck's constant; and c is the speed of light in vacuum. For the LIDAR calculations, the reflectivity of the target is considered to be, on average, 10% and the internal loss of the system was considered to be as high as 10 dB. Such high values were chosen to account for the presence of background noise and transmission losses in a daylight outdoors environment.

6.5.2 Laser power estimations for imaging at longer distance ranges

A LIDAR system incorporating a 26 μm diameter planar Ge-on-Si SPAD, operated at a temperature of 125 K and an excess bias of 2.5% above breakdown was assumed for all the calculations. The repetition rate of the illuminating light was 100 kHz. Figure 6.9 presents estimations of the average laser power required for imaging in air at distances of up to 10 km. We considered different acquisition times of 1, 3, 10 and 30 ms and two illuminating wavelengths of 1310 and 1450 nm. As expected, it is clear from the graphs that imaging at longer distances can be achieved using lower optical powers when longer acquisition times are employed. For rapid imaging applications, higher optical powers and shorter acquisition times would be required. We predict that a LIDAR system incorporating such a device would be able to image an object at 1 km while remaining eye-safe using per pixel acquisition times as short as 3 ms and 1 ms for wavelengths of 1450 nm and 1310 nm, respectively.

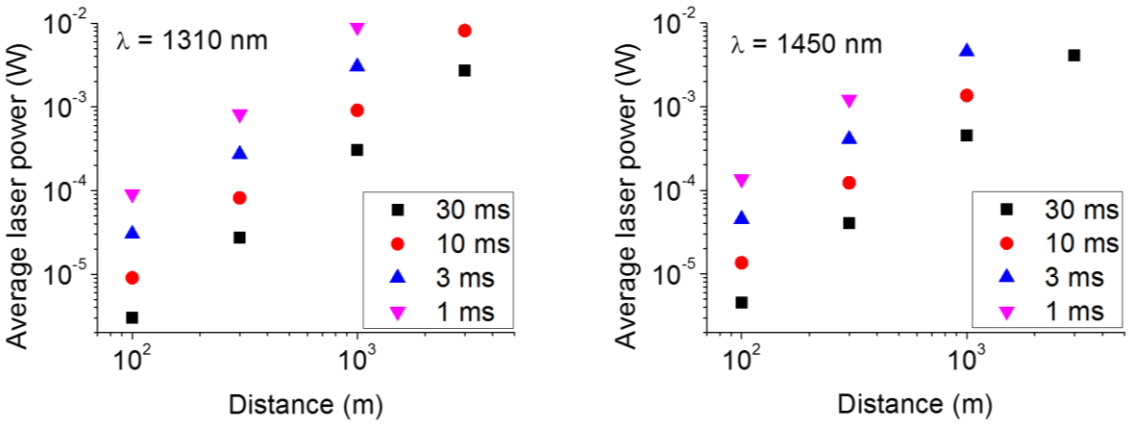

Figure 6.9. Laser power required to image a target at different stand-off distances from 100 m to 10 km using 1310 nm (left) and 1450 nm (right) wavelength illuminations. The estimation considers different acquisition times per pixel: 1 ms (pink triangles), 3 ms (blue triangles), 10 ms (red circles) and 30 ms (black squares). The estimation is based on a collecting lens of a 25.4 mm diameter and a 26 μm diameter planar Ge-on-Si SPAD considered to be operated at a temperature of 125 K under an excess bias of 2.5% above the breakdown. The repetition rate of the illuminating pulsed laser source is 100 kHz.

Figure 6.10 demonstrates an estimation of average laser power required to image a target at 300 m in attenuating media at a different number of attenuating lengths. Figure 6.10 shows that sub mW of optical power would be required for successful imaging through a weak attenuating medium when the laser power drops by a factor of 1/*e* after traveling 300 m in such a medium. The required laser power increases to mW levels for more attenuating media. Finally, a maximum of 4 attenuation lengths can be achieved using laser powers of 250 mW (1310 nm) and 360 mW (1450 nm).

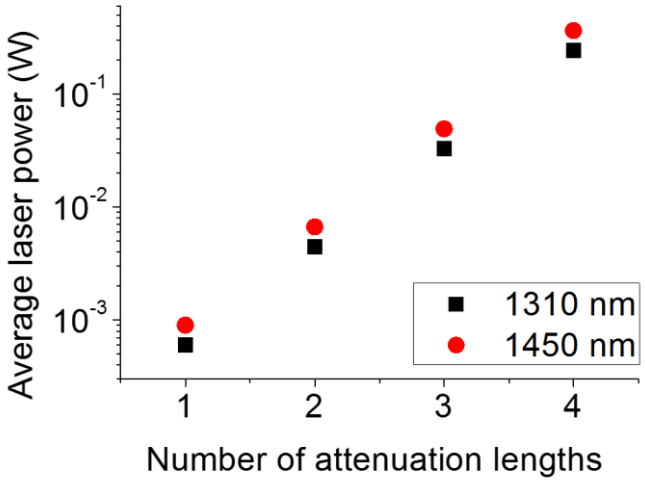

Figure 6.10. Laser power required to image a target at a stand-off distance of 300 m for different attenuation lengths using 1310 nm (black squares) and 1450 nm (red circles) operating wavelengths and 10 ms per pixel acquisition time. The estimate is based on a collecting lens of a 25.4 mm diameter and a 26 μm diameter planar Ge-on-Si SPAD considered to be operated at a temperature of 125 K under an excess bias of 2.5% above the breakdown. The repetition rate of the illuminating light is 100 kHz.

6.6 Conclusions

A LIDAR system incorporating a single planar Ge-on-Si SPAD detector has been demonstrated. These detectors offer high single-photon detection efficiency, relatively low dark count rates and good temporal response [44]. These detectors possess the advantages of compatibility with mature Si technology while expanding the wavelength of operation beyond the sensitivity of Si SPADs potentially up to 1550 nm. Such operating wavelengths benefit from lower solar background noise and reduced atmospheric attenuation compared to the NIR wavelength region. More importantly, 20 times higher average optical power levels of the illuminating beam can be used while remaining eye-safe.

We acquired high-resolution 3D images of various targets using the TCSPC technique in a dark laboratory environment. Millimetre depth resolutions were achieved from a stand-off distance of 0.4 m for acquisition times in the milliseconds per pixel regime. All measurements were performed using pW average optical powers. We also demonstrated the potential for the reduction of the total acquisition time by obtaining partial information

about the target and further restoring the image by applying the RDI-TV algorithm. This algorithm allows image reconstruction even when up to 75% of data is missing or corrupted. It was estimated that such a system would require sub mW laser powers at wavelengths in SWIR region of 1310 and 1450 nm to image a scene at up to a 1 km range. For example, using 1 ms and 30 ms per pixel acquisition times, the average laser powers required to image a target at 1 km using 1310 nm wavelength illumination would be 9 mW and 0.3 mW, respectively. If 1450 nm wavelength is used for illumination, the average laser powers required would be 13.5 mW or 0.45 mW for per pixel acquisition times of 1 ms or 30 ms, respectively. In addition, for rapid imaging using 1 ms per pixel acquisition time the imaging of a 10000 pixels scene takes 2.5 s and 100000 pixels in 25 s, respectively. At 300 metres, the average laser power levels required for successful imaging are 0.8 mW and 1.2 mW for illumination wavelengths of 1310 nm and 1450 nm, respectively. This demonstrates the potential for rapid automotive 3D imaging. We also presented an estimation of the average laser power required to image a target through an attenuating medium. Based on these estimations this LIDAR system can potentially achieve successful imaging at 300 m at up to 2 attenuation lengths while remaining eye-safe. The results presented in this Chapter show a potential for a new low-cost LIDAR system for single-photon sensing and 3D imaging in the eye-safe SWIR region. Various advanced applications that operate in this wavelength region such as automotive and autonomous vehicles, security and environmental monitoring would benefit from a LIDAR system that employs planar Ge-on-Si SPADs detectors.

6.7 Acknowledgments

The restoration of depth and intensity using total variation algorithm described in this Chapter have been developed by Dr. Abderrahim Halimi from Institute of Sensors, Signals and Systems at Heriot-Watt University. The results presented in this Chapter form the basis of a paper that is currently under preparation to be submitted to Optics Express.

6.8 References

1. C. Mallet and F. Bretar, *Full-waveform topographic lidar: State-of-the-art.* ISPRS Journal of Photogrammetry and Remote Sensing, 2009. **64**(1): p. 1-16.

2. M.-C. Amann, T.M. Bosch, M. Lescure, R.A. Myllylae and M. Rioux, *Laser ranging: a critical review of unusual techniques for distance measurement.* Optical Engineering, 2001. **40**(1): p. 10-20.

3. B. Schwarz, *LIDAR: Mapping the world in 3D.* Nature Photonics, 2010. **4**(7): p. 429.

4. C. Weitkamp, *Lidar: range-resolved optical remote sensing of the atmosphere*. Vol. 102. 2006: Springer Science & Business.

5. G. Buller and A. Wallace, *Ranging and three-dimensional imaging using time-correlated single-photon counting and point-by-point acquisition.* IEEE Journal of Selected Topics in Quantum Electronics, 2007. **13**(4): p. 1006-1015.

6. J.S. Massa, G.S. Buller, A.C. Walker, S. Cova, M. Umasuthan, and A.M. Wallace, *Time-of-flight optical ranging system based on time-correlated single-photon counting.* Applied Optics, 1998. **37**(31): p. 7298-7304.

7. A.M. Wallace, A. McCarthy, C.J. Nichol, X. Ren, S. Morak, D. Martinez-Ramirez, I.H. Woodhouse, and G.S. Buller, *Design and evaluation of multispectral lidar for the recovery of arboreal parameters.* IEEE Transactions on Geoscience and Remote Sensing, 2014. **52**(8): p. 4942-4954.

8. A. Maccarone, A. McCarthy, X. Ren, R.E. Warburton, A.M. Wallace, J. Moffat, Y. Petillot, and G.S. Buller, *Underwater depth imaging using time-correlated single-photon counting.* Optics Express, 2015. **23**(26): p. 33911-33926.

9. A. Halimi, A. Maccarone, A. McCarthy, S. McLaughlin and G.S. Buller, *Object depth profile and reflectivity restoration from sparse single-photon data acquired in underwater environments.* IEEE Transactions on Computational Imaging, 2017. **3**(3): p. 472-484.

10. A. McCarthy, X. Ren, A. Della Frera, N.R. Gemmell, N.J. Krichel, C. Scarcella, A. Ruggeri, A. Tosi, and G.S. Buller, *Kilometer-range depth imaging at 1550 nm wavelength using an InGaAs/InP single-photon avalanche diode detector.* Optics Express, 2013. **21**(19): p. 22098-22113.

11. A.M. Pawlikowska, A. Halimi, R.A. Lamb and G.S. Buller, *Single-photon three-dimensional imaging at up to 10 kilometers range.* Optics Express, 2017. **25**(10): p. 11919-11931.

12. Z. Li, E. Wu, C. Pang, B. Du, Y. Tao, H. Peng, H. Zeng, and G. Wu, *Multi-beam single-photon-counting three-dimensional imaging lidar.* Optics Express, 2017. **25**(9): p. 10189-10195.

13. International Electrotechnical Commission, *Safety of laser products-Part 1: Equipment classification and requirements.* IEC 60825-1, 2007.

14. L.S. Rothman, D. Jacquemart, A. Barbe, D.C. Benner, M. Birk, L. Brown, M. Carleer, C. Chackerian Jr, K. Chance, L. Coudert, and et al., *The HITRAN 2004 molecular spectroscopic database.* Journal of Quantitative Spectroscopy and Radiative Transfer, 2005. **96**(2): p. 139-204.

15. D. Killinger, *Free space optics for laser communication through the air.* Optics and Photonics News, 2002. **13**(10): p. 36-42.

16. R. Tobin, A. Halimi, A. McCarthy, M. Laurenzis, F. Christnacher, and G.S. Buller, *Three-dimensional single-photon imaging through obscurants.* Optics Express, 2019. **27**(4): p. 4590-4611.

17. F. Nadeem, T. Javornik, E. Leitgeb, V. Kvicera and G. Kandus, *Continental fog attenuation empirical relationship from measured visibility data.* Radioengineering, 2010. **19**(4): p. 596-600.

18. H. Willebrand and B.S. Ghuman, *Free space optics: enabling optical connectivity in today's networks*. 2002: SAMS Publishing.

19. R.E. Bird, R.L. Hulstrom and L. Lewis, *Terrestrial solar spectral data sets.* Solar Energy, 1983. **30**(6): p. 563-573.

20. M.A. Albota, B.F. Aull, D.G. Fouche, R.M. Heinrichs, D.G. Kocher, R.M. Marino, J.G. Mooney, N.R. Newbury, M.E. O'Brien, and B.E. Player, *Three-dimensional imaging laser radars with Geiger-mode avalanche photodiode arrays.* Lincoln Laboratory Journal, 2002. **13**(2): p. 351-370.

21. B.F. Aull, A.H. Loomis, D.J. Young, R.M. Heinrichs, B.J. Felton, P.J. Daniels, and D.J. Landers, *Geiger-mode avalanche photodiodes for three-dimensional imaging.* Lincoln Laboratory Journal, 2002. **13**(2): p. 335-349.

22. A. McCarthy, R.J. Collins, N.J. Krichel, V. Fernández, A.M. Wallace, and G.S. Buller, *Long-range time-of-flight scanning sensor based on high-speed time-correlated single-photon counting.* Applied Optics, 2009. **48**(32): p. 6241-6251.

23. P.A. Hiskett, C.S. Parry, A. McCarthy and G.S. Buller, *A photon-counting time-of-flight ranging technique developed for the avoidance of range ambiguity at gigahertz clock rates.* Optics Express, 2008. **16**(18): p. 13685-13698.

24. C. Niclass, A. Rochas, P.-A. Besse and E. Charbon, *Design and characterization of a CMOS 3-D image sensor based on single photon avalanche diodes.* IEEE Journal of Solid-State Circuits, 2005. **40**(9): p. 1847-1854.

25. D. Stoppa, L. Pancheri, M. Scandiuzzo, L. Gonzo, G.-F. Dalla Betta, and A. Simoni, *A CMOS 3-D imager based on single photon avalanche diode.* IEEE Transactions on Circuits and Systems I: Regular Papers, 2007. **54**(1): p. 4-12.

26. C. Niclass, M. Soga, H. Matsubara, S. Kato and M. Kagami, *A 100-m Range 10-Frame/s 340 x 96-Pixel Time-of-Flight Depth Sensor in 0.18-mu m CMOS.* IEEE Journal of Solid-State Circuits, 2013. **48**(2): p. 559-572.

27. M. Entwistle, M.A. Itzler, J. Chen, M. Owens, K. Patel, X. Jiang, K. Slomkowski, and S. Rangwala. *Geiger-mode APD camera system for single-photon 3D LADAR imaging*. in *Advanced Photon Counting Techniques VI*. 2012. International Society for Optics and Photonics.

28. R. Tobin, A. Halimi, A. McCarthy, X. Ren, K.J. McEwan, S. McLaughlin, and G.S. Buller, *Long-range depth profiling of camouflaged targets using single-photon detection.* Optical Engineering, 2017. **57**(3): p. 031303.

29. X. Jiang, M. Itzler, K. O'Donnell, M. Entwistle, M. Owens, K. Slomkowski, and S. Rangwala, *InP-based single-photon detectors and geiger-mode APD arrays for quantum communications applications.* IEEE Journal of Selected Topics in Quantum Electronics, 2015. **21**(3): p. 5-16.

30. G. Buller and R. Collins, *Single-photon generation and detection.* Measurement Science and Technology, 2009. **21**(1): p. 012002.

31. M.G. Tanner, C. Natarajan, V. Pottapenjara, J. O'Connor, R. Warburton, R. Hadfield, B. Baek, S. Nam, S. Dorenbos, and E.B. Ureña, *Enhanced telecom wavelength single-photon detection with NbTiN superconducting nanowires on oxidized silicon.* Applied Physics Letters, 2010. **96**(22): p. 221109.

32. A. McCarthy, N.J. Krichel, N.R. Gemmell, X. Ren, M.G. Tanner, S.N. Dorenbos, V. Zwiller, R.H. Hadfield, and G.S. Buller, *Kilometer-range, high resolution depth imaging via 1560 nm wavelength single-photon detection.* Optics Express, 2013. **21**(7): p. 8904-8915.

33. R.E. Warburton, A. McCarthy, A.M. Wallace, S. Hernandez-Marin, R.H. Hadfield, S.W. Nam, and G.S. Buller, *Subcentimeter depth resolution using a single-photon counting time-of-flight laser ranging system at 1550 nm wavelength.* Optics Letters, 2007. **32**(15): p. 2266-2268.

34. C.M. Natarajan, M.G. Tanner and R.H. Hadfield, *Superconducting nanowire single-photon detectors: physics and applications.* Superconductor Science and Technology, 2012. **25**(6): p. 063001.

35. R.E. Warburton, G. Intermite, M. Myronov, P. Allred, D.R. Leadley, K. Gallacher, D.J. Paul, N.J. Pilgrim, L.J.M. Lever, Z. Ikonic, R.W. Kelsall, E. Huante-Ceron, A.P. Knights, and G.S. Buller, *Ge-on-Si Single-Photon Avalanche Diode Detectors: Design, Modeling, Fabrication, and Characterization at Wavelengths 1310 and 1550 nm.* IEEE Transactions on Electron Devices, 2013. **60**(11): p. 3807-3813.

36. Z. Lu, Y. Kang, C. Hu, Q. Zhou, H.-D. Liu, and J.C. Campbell, *Geiger-Mode Operation of Ge-on-Si Avalanche Photodiodes.* IEEE Journal of Quantum Electronics, 2011. **47**(5): p. 731-735.

37. N.J. Martinez, M. Gehl, C.T. Derose, A.L. Starbuck, A.T. Pomerene, A.L. Lentine, D.C. Trotter, and P.S. Davids, *Single photon detection in a waveguide-coupled Ge-on-Si lateral avalanche photodiode.* Optics Express, 2017. **25**(14): p. 16130-16139.

38. A. Halimi, Y. Altmann, A. McCarthy, X. Ren, R. Tobin, G.S. Buller, and S. McLaughlin. *Restoration of intensity and depth images constructed using sparse single-photon data*. in *Signal Processing Conference (EUSIPCO), 2016 24th European*. 2016. IEEE.

39. Y. Altmann, X. Ren, A. McCarthy, G.S. Buller and S. McLaughlin, *Lidar waveform-based analysis of depth images constructed using sparse single-photon data.* IEEE Transactions on Image Processing, 2016. **25**(5): p. 1935-1946.

40. D. Shin, F. Xu, D. Venkatraman, R. Lussana, F. Villa, F. Zappa, V.K. Goyal, F.N. Wong, and J.H. Shapiro, *Photon-efficient imaging with a single-photon camera.* Nature Communications, 2016. **7**: p. 12046.

41. D. Shin, F. Xu, F.N. Wong, J.H. Shapiro and V.K. Goyal, *Computational multi-depth single-photon imaging.* Optics Express, 2016. **24**(3): p. 1873-1888.

42. N.J. Krichel, A. McCarthy, I. Rech, M. Ghioni, A. Gulinatti, and G.S. Buller, *Cumulative data acquisition in comparative photon-counting three-dimensional imaging.* Journal of Modern Optics, 2011. **58**(3-4): p. 244-256.

43. R. Richmond and S. Cain, *Direct-Detection Ladar System; TT85*. 2009, SPIE Publications: Bellingham, WA, USA.

44. P. Vines, K. Kuzmenko., J. Kirdoda, D.C. Dumas, M.M. Mirza, R.W. Millar, D.J. Paul, and G.S. Buller, *High performance planar Ge-on-Si single-photon avalanche detectors.* Nature Communications, 2019. **10**(1): p. 1086.

Chapter 7. Conclusions and future work

7.1 Conclusions

Single-photon counting in the SWIR region has developed increasing interest as for a range of emerging applications. For example, quantum communications at 1310 nm and 1550 nm wavelengths take advantage of the low attenuation windows in standard optical fibres [1]. In single-photon LIDAR applications, operating at wavelengths above 1400 nm allows the use of greater optical powers compared to near-infrared due to the increased laser eye-safety thresholds [2]. In addition, the solar background is reduced compared to the near-infrared and visible regions [3]. Also, the atmospheric transmission is greater at wavelengths around 1550nm [4, 5]. In Chapter 2, single-photon detection in the SWIR region was described and included an overview of existing single-photon detectors for operation in the SWIR spectral region. As mentioned in Chapter 2, there are two types of commercially available single-photon detectors that operate in this spectral region: superconducting nanowire single-photon detectors (SNSPDs) and InGaAs/InP SPAD detectors. SNSPDs demonstrate excellent SPDEs of up to 90% [6-8], low DCR [6] and low timing jitter of down to 18 ps [6]. Although these detectors are very efficient, they require operation at cryogenic temperatures below 3 K, imposing practical limitations on the range of possible applications that could employ SNSPDs. In applications that require compact single-photon detectors, InGaAs/InP SPADs are commonly used. These detectors demonstrate SPDEs of up to 45% [9], low DCRs [10] and jitters which can be as low as 30 ps [9]. However, InGaAs/InP SPADs suffer from afterpulsing, which can place severe limitations on the maximum count rate possible. In addition, integration of InGaAs/InP SPADs onto Si photonics platforms has proven very difficult. In Chapter 3, an alternative semiconductor material, Ge, have been discussed as a possible candidate material for absorber layers in single-photon detectors operational at wavelengths of up to 1.6 μm in the SWIR region. In addition, Ge has the potential of being integrated onto Si photonics platform. The integration of single-photon detectors with other photonics components on the same chip is one of the major goals in developing quantum computing systems. Having all the components on the same chip allows for improvements in efficiency due to the elimination of insertion losses and a reduction in system size. A short overview of the Ge-on-Si single-photon detectors reported in the literature have concluded the Chapter 3.

In this thesis, the design and development of planar geometry Ge-on-Si SPAD detectors has been presented. These detectors exploit low defect Si for impact ionisation, while expanding the sensitivity beyond the Si absorption cut-off by using a Ge layer for photon absorption. In addition, these detectors have the potential for fabrication using CMOS compatible processes, similar to those commonly used in microelectronics. In Chapter 4, different designs of Ge-on-Si SPAD detectors and corresponding electric field simulations have been presented. These designs are based on the SACM structure. Such a structure allows for separate optimisation of the electric field within the device, independent of its absorption properties. A high electric field is maintained in the Si multiplication layer to ensure the occurrence of avalanche multiplication while the electric field in Ge is maintained at a level sufficient for inducing carrier transport but significantly lower than in Si. The electric field simulations were used to develop a new planar geometry design. It was found that reducing the diameter of the top contact with respect to the charge sheet, in combination with separating the sidewalls and the charge sheet by 10 µm, ensures that the electric field is confined to the centre of the detector. This significantly reduces the leakage current, which in turn, reduces the DCR when biased above avalanche breakdown. The results presented in Chapter 4 served as the basis designs for the fabricated devices.

Planar geometry Ge-on-Si SPAD detectors were fabricated by our collaborators from the University of Glasgow. In Chapter 5, the results of single-photon characterisation of Ge-on-Si SPAD detectors with diameters ranging from 26 µm to 200 µm performed at operating temperatures between 78 K and 175 K have been presented. At a temperature of 125 K, the SPDEs of up to 38% at a detection wavelength of 1310 nm were measured using 100 µm diameter device at excess bias of 5.5%. This value is almost an order of magnitude higher compered to the previously reported for Ge-on-Si SPAD detectors. The DCR per unit area measured using 100 µm diameter Ge-on-Si SPADs at a temperature of 100 K was 18.3 count $s^{-1}\mu m^{-2}$, which is three orders of magnitude lower than the value for the previously reported Ge-on-Si SPADs. The lowest NEP measured using these devices was of 2×10^{-16} $WHz^{-1/2}$, which is almost two orders of magnitude lower than the lowest previously reported NEP of 1×10^{-14} $WHz^{-1/2}$ for mesa Ge-on-Si SPADs. The minimum timing jitter measured using 100 µm diameter detectors was 310 ps.

A study of the spectral dependence of SPDE was performed in the wavelength range between 1310 nm and 1550 nm at different operating temperatures, which clearly exhibited that the cut-off wavelength of planar Ge-on-Si SPADs increases with the increasing temperature, as expected. From these results, it was predicted that planar geometry Ge-on-Si SPAD detectors with a 1 µm thick Ge absorption layer will be capable of efficient detection (at 50% of the λ = 1450nm SPDE value) at a wavelength of 1550 nm at an operating temperature as low as 245 K. According to the estimations, only less than 50% of light at 1310 nm wavelength is absorbed within the 1 µm thick Ge absorber. Hence, there is a potential to improve the SPDE by using thicker Ge absorption layers, which would allow efficient detection of longer wavelength photons at temperatures even lower than 245 K.

An afterpulsing study in Ge-on-Si SPAD detectors was performed using the double gating technique at temperatures between 100 K and 175 K. As expected, it was demonstrated that afterpulsing reduces with increased temperature. A comparison of the afterpulsing in a planar Ge-on-Si SPAD and a commercial InGaAs/InP SPAD detectors under identical operating conditions was demonstrated. Both detectors were operated at a temperature of 125 K and at an excess bias that corresponds to 17% SPDE. Ge-on-Si SPADs have demonstrated reduced afterpulsing when compared to InGaA/InP SPADs. For example, using a delay time of 10 µs, which corresponds to 100 kHz count rate, Ge-on-Si SPAD detectors exhibited five times lower afterpulsing than InGaAs/InP SPAD under nominally identical conditions. Although InGaAs/InP SPADs are optimised for operation at higher temperatures, Ge-on-Si SPADs require further optimisation to operate at temperature above 175 K. However, Ge-on-Si demonstrated the potential for high count rate operation. An afterpulsing study of different diameter devices from 26 µm to 100 µm is planned for future work to better understand the origin of this phenomenon in Ge-on-Si SPADs.

Using an improved planarisation step during the fabrication process, it was possible to fabricate smaller diameter devices down to 26 µm. Single-photon characterisation of these detectors was performed in the same temperature range between 78 K and 175 K. The highest SPDE of 30% at a detection wavelength of 1310 nm was measured using a 26 µm diameter devices operated at a temperature of 125 K and an excess bias of 6.5%. The DCR per unit area of 3.5 count $s^{-1}\mu m^{-2}$ was measured using these devices, which is

four orders of magnitude lower than the previously published lowest value for Ge-on-Si SPADs. A record low NEP of 4×10^{-17} $WHz^{-1/2}$, which is 240 times lower than the lowest previously reported value for Ge-on-Si SPADs. A timing jitter of these devices was measured to be as low as 150 ps.

A development of a laboratory-based LIDAR system incorporating an individual planar Ge-on-Si SPAD detector has been described in Chapter 6. Three-dimensional imaging of vehicle models has been demonstrated in a dark laboratory environment at a stand-off distance of 0.4 m using pW laser power levels at 1450 nm wavelength. Based on the experimental results, the average laser power levels required for successful imaging at longer distances have been estimated. According to these estimations, it is expected that eye-safe sub-mW laser powers at 1310 nm or 1450 nm wavelengths would be sufficient for imaging targets at distance ranges of the order of 1 km. Although the measurements were performed in a dark laboratory environment, a high internal system loss of 10 dB and a low target reflectivity of 10% was considered for the laser power estimations to factor in solar background noise and atmospheric attenuation present in an outdoor environment. Of course, future investigation of the system performance in an outdoor environment under day-light conditions is required. In addition, once the Ge-on-Si SPAD detectors are optimised for operation at higher temperature and longer wavelengths, there is the potential of using these detectors in automotive, autonomous LIDAR applications.

7.2 Future Work

Although the planar Ge-on-Si SPADs described in this Thesis demonstrated record low NEPs compared to the Ge-on-Si SPADs reported in the literature [11-13], had SPDE values similar to those of commercially available InGaAs/InP SPAD detectors and considerably reduced afterpulsing effects, there remain a number of ways in which to improve the detector performance. Further optimisation is required to reduce the DCR at higher temperatures of operation, which will enable efficient single-photon detection at wavelengths around 1550 nm. Operation at temperatures compatible with Peltier cooling systems will also allow using Ge-on-Si SPADs in applications that require compact and mobile single-photon detectors.

Firstly, as mentioned previously, reducing the size of the SPADs will lead to lower DCR levels, which will allow higher temperatures of operation, and higher levels of excess

bias, which, in turn, will lead to the higher SPDE values. In addition, single-photon characterisation of smaller size detectors will help to confirm the origin of the dark counts. Indeed, preliminary characterisation of a 26 μm diameter planar Ge-on-Si SPADs demonstrated single-photon operation at 200 K and considerably lower DCR and NEP compared to the 100 μm diameter SPADs presented in Chapter 5. However, further experimental investigation is required to confirm the origin of dark counts in these devices. In an attempt to further reduce the DCR, the fabrication of smaller diameter devices down to 10 μm is planned for future generations of the Ge-on-Si SPADs. In addition, it would be useful to fabricate these devices using selective area growth in order to investigate the contribution of threading dislocations to the DCR. It has been reported that utilising this technique results in lower defect densities and improved performance in Ge-on-Si p-n and p-i-n photodetectors [14, 15]. However, the impact of selective area growth on SPAD performance is currently unknown and further investigation is required.

Secondly, as mentioned in Chapter 4, further optimisation of the Ge absorption layer is required to increase the SPDE even further. The designs with 2 μm and 3 μm thick absorber have been proposed in order to achieve up to ~88% absorption of 1310 nm wavelength light, which, in turn, will increase the SPDE and will lower the value of the operation temperature required for efficient operation at a wavelength of 1550 nm. Fabrication of devices with 2 μm and 3 μm thick Ge absorption layers is planned for future work.

Thirdly, future Ge-on-Si SPAD designs should consider waveguide structures. Such device structures can be easily integrated onto the Si photonics components and provide a potential route towards reducing the DCR and improving the detection efficiency if correctly optimised.

Finally, the fabrication of linear Ge-on-Si SPAD detector arrays is planned for future work. Further investigation will be required to assess the performance of these detectors in an array configuration, which has not been carried out previously. Additional study is also required to determine the optimum distance from the active area of the detector to the Ge absorber sidewalls. As mentioned in Chapter 4, decreasing this distance would improve the fill factor of the Ge-on-Si SPAD array. However, more fabricated samples are required to determine the optimal parameters and further design optimisation may be required to eliminate cross talk, for example. The use of linear or two-dimensional SPAD

detector arrays in single-photon LIDAR applications will enable much faster acquisition times. The use of Ge-on-Si SPAD detectors will allow a relatively low cost picosecond single-photon camera, enabling deployment of 3D imaging in a variety of application scenarios.

After a laboratory-based demonstration of the LIDAR imaging system incorporating an individual planar Ge-on-Si SPAD detector, it would be informative to test its performance in a field trial over longer distances and in daylight. To determine the limitations of the system, imaging of a range of targets with different surface reflectivity should be performed. In addition, a demonstration of such a system performing imaging of moving objects would be essential to prove the effective use for automotive and autonomous LIDAR applications. Once developed, a Ge-on-Si SPAD array used for LIDAR could significantly reduce the total acquisition time.

7.3 References

1. K. Gerd, *Optical Fiber Communications*. 2 ed. 1991, New-York: McGraw-Hill.

2. International Electrotechnical Commission, *Safety of laser products-Part 1: Equipment classification and requirements.* IEC 60825-1, 2007.

3. R.E. Bird, R.L. Hulstrom and L. Lewis, *Terrestrial solar spectral data sets.* Solar Energy, 1983. **30**(6): p. 563-573.

4. D. Killinger, *Free space optics for laser communication through the air.* Optics and Photonics News, 2002. **13**(10): p. 36-42.

5. L.S. Rothman, D. Jacquemart, A. Barbe, D.C. Benner, M. Birk, L. Brown, M. Carleer, C. Chackerian Jr, K. Chance, L. Coudert, and et al., *The HITRAN 2004 molecular spectroscopic database.* Journal of Quantitative Spectroscopy and Radiative Transfer, 2005. **96**(2): p. 139-204.

6. A. Pearlman, A. Cross, W. Slysz, J. Zhang, A. Verevkin, M. Currie, A. Korneev, P. Kouminov, K. Smirnov, and B. Voronov, *Gigahertz counting rates of NbN single-photon detectors for quantum communications.* IEEE Transactions on Applied Superconductivity, 2005. **15**(2): p. 579-582.

7. W. Zhang, L. You, H. Li, J. Huang, C. Lv, L. Zhang, X. Liu, J. Wu, Z. Wang, and X. Xie, *NbN superconducting nanowire single photon detector with efficiency over 90% at 1550 nm wavelength operational at compact cryocooler temperature.* Science China Physics, Mechanics & Astronomy, 2017. **60**(12): p. 120314.

8. J. Sprengers, A. Gaggero, D. Sahin, S. Jahanmirinejad, G. Frucci, F. Mattioli, R. Leoni, J. Beetz, M. Lermer, and M. Kamp, *Waveguide superconducting single-photon detectors for integrated quantum photonic circuits.* Applied Physics Letters, 2011. **99**(18): p. 181110.

9. M.A. Itzler, X. Jiang, M. Entwistle, K. Slomkowski, A. Tosi, F. Acerbi, F. Zappa, and S. Cova, *Advances in InGaAsP-based avalanche diode single photon detectors.* Journal of Modern Optics, 2011. **58**(3-4): p. 174-200.

10. B. Korzh, N. Walenta, T. Lunghi, N. Gisin and H. Zbinden, *Free-running InGaAs single photon detector with 1 dark count per second at 10% efficiency.* Applied Physics Letters, 2014. **104**(8): p. 081108.

11. R.E. Warburton, G. Intermite, M. Myronov, P. Allred, D.R. Leadley, K. Gallacher, D.J. Paul, N.J. Pilgrim, L.J.M. Lever, Z. Ikonic, R.W. Kelsall, E. Huante-Ceron, A.P. Knights, and G.S. Buller, *Ge-on-Si Single-Photon Avalanche Diode Detectors: Design, Modeling, Fabrication, and Characterization at Wavelengths 1310 and 1550 nm.* IEEE Transactions on Electron Devices, 2013. **60**(11): p. 3807-3813.

12. N.J. Martinez, M. Gehl, C.T. Derose, A.L. Starbuck, A.T. Pomerene, A.L. Lentine, D.C. Trotter, and P.S. Davids, *Single photon detection in a waveguide-coupled Ge-on-Si lateral avalanche photodiode.* Optics Express, 2017. **25**(14): p. 16130-16139.

13. Z. Lu, Y. Kang, C. Hu, Q. Zhou, H.-D. Liu, and J.C. Campbell, *Geiger-Mode Operation of Ge-on-Si Avalanche Photodiodes.* IEEE Journal of Quantum Electronics, 2011. **47**(5): p. 731-735.

14. S. Claussen, K. Balram, E. Fei, T. Kamins, J. Harris, and D. Miller, *Selective area growth of germanium and germanium/silicon-germanium quantum wells in*

silicon waveguides for on-chip optical interconnect applications. Optical Materials Express, 2012. **2**(10): p. 1336-1342.

15. S. Park, T. Tsuchizawa, T. Watanabe, H. Shinojima, H. Nishi, K. Yamada, Y. Ishikawa, K. Wada, and S. Itabashi, *Monolithic integration and synchronous operation of germanium photodetectors and silicon variable optical attenuators.* Optics Express, 2010. **18**(8): p. 8412-8421.